ISTANBUL TECHNICAL UNIVERSITY ★ GRADUATE SCHOOL

DETERMINATION OF SPATIAL DISTRIBUTIONS OF GREENHOUSES USING SATELLITE IMAGES AND OBJECT-BASED IMAGE ANALYSIS APPROACH

PhD THESIS

Gizem ŞENEL

Department of Geomatics Engineering

Geomatics Engineering Programme

MARCH 2023

ISTANBUL TECHNICAL UNIVERSITY ★ GRADUATE SCHOOL

DETERMINATION OF SPATIAL DISTRIBUTIONS OF GREENHOUSES USING SATELLITE IMAGES AND OBJECT-BASED IMAGE ANALYSIS APPROACH

PhD THESIS

Gizem ŞENEL
(501182620)

Department of Geomatics Engineering

Geomatics Engineering Programme

Thesis Advisor: Prof. Dr. Çiğdem GÖKSEL
Thesis Co-Advisor: Prof. Dr. Manuel Angel AGUILAR TORRES

MARCH 2023

ISTANBUL TEKNİK ÜNİVERSİTESİ ★ LİSANSÜSTÜ EĞİTİM ENSTİTÜSÜ

NESNE TABANLI SINIFLANDIRMA YAKLAŞIMI VE UYDU GÖRÜNTÜLERİ KULLANILARAK SERALARIN MEKANSAL DAĞILIMININ BELİRLENMESİ

DOKTORA TEZİ

Gizem ŞENEL
(501182620)

Geomatik Mühendisliği Anabilim Dalı

Geomatik Mühendisliği Programı

Tez Danışmanı: Prof. Dr. Çiğdem GÖKSEL
Eş Danışman: Prof. Dr. Manuel Angel AGUILAR TORRES

MART 2023

Gizem ŞENEL, Ph.D. student of ITU Graduate School student ID 501182620 successfully defended the thesis/dissertation entitled "DETERMINATION OF SPATIAL DISTRIBUTIONS OF GREENHOUSES USING SATELLITE IMAGES AND OBJECT-BASED IMAGE ANALYSIS APPROACH", which she prepared after fulfilling the requirements specified in the associated legislations, before the jury whose signatures are below.

Thesis Advisor :	**Prof. Dr. Çiğdem GÖKSEL** Istanbul Technical University	....
Co-advisor :	**Prof. Dr. Manuel Angel AGUILAR TORRES** University of Almería	....
Jury Members :	**Prof. Dr. Elif SERTEL** Istanbul Technical University	....
	Prof. Dr. Dilek KOÇ SAN Akdeniz University	....
	Prof. Dr. Dursun Zafer ŞEKER Istanbul Technical University	....
	Prof. Dr. Hande DEMİREL Istanbul Technical University	....
	Prof. Dr. Fernando Jose AGUILAR TORRES University of Almería	....

Date of Submission : 03 February 2023
Date of Defense : 02 March 2023

FOREWORD

I am happy to have completed this thesis, even though it was a challenging experience both emotionally and academically. The help and support of many people brought me an end during my doctoral journey.

I would like to start by expressing my greatest appreciation to my supervisor Prof. Dr. Çiğdem GÖKSEL, who has been my biggest supporter since I was an undergraduate student. I will be forever grateful for all the opportunities and endless support she has provided me.

I would like to express my sincere thanks to my family and my dearest friends for their encouragement and moral support during my challenging journey. I would like to express my special gratitude to Muradiye, whom I thank every day for knowing her, and for never giving up her support.

I am also grateful to my co-advisor, Prof. Dr. Manuel Ángel AGUILAR TORRES and Prof. Dr. Fernando José AGUILAR TORRES, for all the opportunities and endless academic support they provided me at the University of Almería, where I was a visiting researcher with the support of TUBITAK 2214-A International Doctoral Research Fellowship Programme. At this point, I would like to express my special gratitude to Dr. Abderrahim NEMMAOUI for doing his best to make my life in Almería easier and for helping me whenever I needed. I learned a lot from them, and I am honored to have the opportunity to work with them.

Also, during my Ph.D. education, I was a scholar of the Council of Higher Education, Turkey (in Turkish Yükseköğretim Kurulu, YÖK) in the priority field of Remote Sensing and GIS within the scope of 100/2000 Program and TUBITAK 2211-A which I would like to acknowledge. I also would like to thank Istanbul Technical University Center for Satellite Communications, Remote Sensing (ITU-CSCRS) for providing SPOT-7 data for this thesis.

February 2023

Gizem ŞENEL
(Geomatics Engineer)

TABLE OF CONTENTS

Page

ABBREVIATIONS

AFI	: Area Fit Index
AG	: Agricultural Greenhouses
ANOVA	: Analysis of Variance
APGI	: Advanced Plastic Greenhouse Index
CART	: Classification and Regression Trees
Catboost	: Categorical Boosting
CNN	: Convolutional Neural Network
CSBI	: Color Steel Buildings Index
ED2	: Euclidean Distance 2
ED3	: Euclidean Distance 3
EMM	: Estimated Marginal Means
F	: Fitness Function
GB	: Gradient Boosting
GDI	: Greenhouse Detection Index
GEE	: Google Earth Engine
GIS	: Geographic Information Systems
KNN	: K-Nearest Neighbor
LightGBM	: Light Gradient Boosting Machines
LULC	: Land use and land cover
M	: Match
MDI	: Moment Distance Index
MED2	: Modified Euclidean Distance 2
MRS	: Multiresolution Segmentation
MSI	: Multispectral Imagery
NDBI	: Normalized Difference Builtup Index
NDVI	: Normalized Difference Vegetation Index
NIR	: Near infrared

NN : Nearest Neighbor
NSR : Number-of-Segments Ratio
OBIA : Object-based image analysis
OLI : Operational Land Imagery
OS2 : OverSegmentation 2
PCG : Plastic-covered greenhouse
PGHI : Plastic GreenHouse Index
PGI : Plastic Greenhouse Index
PMF : Plastic-mulched farmland
PMLI : Plastic-Mulched Landcover Index
PSE : Potential Segmentation Error
QR : Quality Ratio
RF : Random Forest
RFE : Recursive Feature Elimination
RPGI : Retrogressive Plastic Greenhouse Index
RSS : Reflectance storage scale
SAR : Synthetic aperture radar
SVM : Support Vector Machines
SWIR : Shortwave infrared
TIRs : Thermal Infrared Sensor
TM : Thematic Mapper
US2 : UnderSegmentation 2
VI : Index Greenhouse Vegetable Land Extraction
VNIR : Visible near infrared
WV3 : Worldview-3
XGBoost : Extreme Gradient Boosting

LIST OF TABLES

Page

LIST OF FIGURES

Page

DETERMINATION OF SPATIAL DISTRIBUTIONS OF GREENHOUSES USING SATELLITE IMAGES AND OBJECT-BASED CLASSIFICATION METHODS

SUMMARY

In the face of the expected pressure on agricultural production systems with the increasing world population, one of the most suitable options for sustainable intensification of agricultural production is greenhouse activities that allow an increase in production on existing agricultural lands. Greenhouse activities can cause environmental problems at the local and regional scales. Since the primary material used in the covering of greenhouses is plastic, ecological problems are expected in the near future due to the excessive use of plastic. Besides, they may affect the integrity of ecosystems by changing land use and land cover (LULC) into extensive agricultural areas. On the other hand, the economy of many rural regions is supported by greenhouse activities, especially in Mediterranean countries. Moreover, due to the exposure of these structures to floods, especially with climate change effects, producers face economic and social problems. While all these situations make the production system unsustainable, they also endanger the ecology and economy of the region.

Thanks to synoptic data acquisition and high temporal resolution, remote sensing images allow periodic agricultural sector monitoring. Considering the positive outcomes and adverse effects of greenhouses, determining greenhouse areas using remote sensing images is essential in providing better management strategies. In that case, monitoring through remote sensing images is the most suitable approach to obtain information about the effects of greenhouses on climate and environment and improve their economic output.

Within the scope of this thesis, answers to different questions were sought by using the object-based image analysis (OBIA) approach, which is stated to give better results in the literature to determine greenhouses. OBIA approach consists of mainly three stages which are image segmentation, feature extraction, and image or object classification, and these sections formed the structure of this thesis

In the image segmentation step, which is the first step of the OBIA, answers were sought for two crucial questions for the segmentation of plastic-covered greenhouses (PCG). The first of these questions is which of the supervised segmentation quality assessment metrics performs better in evaluating PCG segmentation. An experimental design was formed in which segmentation metrics were evaluated together with interpreter evaluations. At this stage, sixteen different datasets consisting of different spatial resolutions (medium and high spatial resolution), seasons (summer and winter), study areas (Almería (Spain) and Antalya (Turkey)), and reflection storage scales (RSS) (16Bit and Percent) were used. Various segmentation outputs were created using the Multiresolution segmentation (MRS) algorithm. Six different interpreters evaluated these outputs and compared them with the eight segmentation quality

metrics. As a result of the evaluations, it was concluded that Modified Euclidean Distance 2 (MED2) was the most successful metric in the evaluation of PCG segmentation. On the other hand, Fitness and F-metric failed to identify the best segmentation output compared to other metrics investigated. In addition, the effects of different factors on the visual interpretation results were analyzed statistically. It was revealed that the RSS is an essential factor in visual interpretation. In detail, it was concluded that when evaluating the segmentation outputs created by using the Percent format, the interpreters were more in agreement and interpreted this data type more efficiently.

In the second part of the segmentation phase, how much factors or their interactions affect the greenhouse segmentation was investigated. Approximately 4,000 segmentation outputs were produced from sixteen data sets, and MED2 values were calculated. For each shape parameter in each data set, the values reaching the best MED2 value were determined and statistically tested by analysis of variance (ANOVA). The segmentation outputs calculated from the datasets showed that the optimal scale parameters clustered by taking values close to each other in Percent format and took values in a broader range in 16Bit format. This showed that it would be effortless to determine the most appropriate segmentation outputs obtained from the Percent format. In addition, statistical tests have shown that the segmentation accuracy calculated from different RSS formats is directly dependent on the shape parameter. While segmentation accuracy increases with decreasing shape parameters in Percent format, this is the opposite in 16Bit format. This situation revealed that the shape parameter selection is critical depending on the RSS. In summary, it has been revealed that the Percent format is the appropriate data format for PCG segmentation with the MRS algorithm, and in addition, low-shape parameters should be preferred in the Percent format.

In the second stage of the thesis, it was hypothesized that different feature space evaluation methods and feature space dimensions affect the classification in terms of accuracy and time. Based on this hypothesis, 128 features were obtained from Sentinel-2 images of the Almería and Antalya study areas, and classification performance was evaluated by random forest (RF) algorithm by applying different feature space evaluation methods. As a result of this evaluation, it was seen that the reduction of the feature space has a direct effect on the accuracy. But moreover, it has been determined that reducing the size of the feature space significantly reduces the time required to run the classification algorithm. Therefore, among the examined feature space evaluation algorithms, it has been concluded that RF and Recursive Feature Elimination (RFE)-RF (RFE-RF) algorithms are more suitable for classification accuracy and the time required to run the algorithm. Moreover, it has been found that these algorithms are less dependent on feature space variation in terms of classification accuracy, but reducing the feature space significantly reduces the computation time.

In addition, among a total of 128 features obtained from the segments, including spectral, textural, geometric features and spectral indices, Plastic GreenHouse Index (PGHI) and Normalized Difference Vegetation Index (NDVI) were the most relevant features for PCG mapping according to RF and RFE-RF methods. As a result, the necessity of including indices such as PGHI and NDVI in the feature space and the application of one of the feature space evaluation methods such as RF or RFE-RF in terms of reducing the calculation time are the main outputs of this stage.

In the third and final stage of the thesis, the effectiveness of ensemble learning algorithms for the PCG classification has been tested. According to the experimental results, Categorical boosting (Catboost), RF, and support vector machines (SVM) algorithms performed well in both studied areas (Almería and Antalya), but the implementation time required for CatBoost and SVM is higher than all other algorithms studied. K-nearest neighbor (KNN) and AdaBoost algorithms achieved lower classification performance in both study areas. In addition to these algorithms, the light gradient boosting machines (LightGBM) algorithm achieved an F1 score of over 90% in both study areas in a short time. In summary, considering the computation time and classification accuracy, RF and LightGBM are the two up-front algorithms.

In general, within the scope of this thesis, answers to the questions encountered in the three steps of OBIA were sought to reach the best PCG determination approach. The determination of greenhouses from satellite images was carried out in two essential study areas in the Mediterranean Basin, where greenhouse activities are intensively carried out. Although these outputs belong to selected test sites, they provide important outputs for generalizing the findings on a large scale. Determining the spatial distribution of PCG to minimize the negative effects on the environment and increase their economic returns will make an important contribution to planners and decision-makers in achieving sustainable agriculture goals.

NESNE TABANLI SINIFLANDIRMA YAKLAŞIMI VE UYDU GÖRÜNTÜLERİ KULLANILARAK SERALARIN MEKANSAL DAĞILIMININ BELİRLENMESİ

ÖZET

Hızla artan dünya nüfusu tarımsal üretimin sürdürülebilir şekilde yoğunlaştırılmasını gerekmektedir. Tarımda sürdürülebilir yoğunlaşmayı sağlamak için en uygun seçeneklerden biri, mevcut tarım arazilerinde üretimin artırılmasına olanak tanıyan seracılık faaliyetleridir. Dünyada birçok ülkede ve özellikle Akdeniz ülkelerinin tarımsal üretiminde seracılık faaliyetleri önemli bir yer tutmaktadır. Ülkemizde, Akdeniz Bölgesinde pek çok kırsal bölgenin ekonomisi seracılık faaliyetleri ile desteklenmekte ve tarımsal üretiminin önemli bir bölümünü oluşturan seraların kapladığı alan hızla artmaktadır.

Seracılık faaliyetlerinin, özellikle seraların kaplanmasında kullanılan temel malzeme olan plastiğin aşırı kullanımı nedeniyle yakın gelecekte yerel ve bölgesel ölçekte ekolojik sorunlara yol açabileceği öngörülmektedir. Ayrıca, yoğun seracılık faaliyetleri gübre ve pestisit kullanımının artışını da beraberinde getirmektedir ki bu durum da yüksek seviyede uygulanan kimyasal girdilerin sızıntısına, akiferlerin kirlenmesine ve yüzey suyunun ötrofikasyonuna neden olmaktadır. Tüm bunlara ek olarak, artan dünya nüfusu nedeniyle artan tarım talebi, temel arazi örtüsü türünün yoğun tarım alanlarına dönüşmesine neden olmaktadır. Tarımda plastik seraların kullanımı bu dönüşümü önemli ölçüde hızlandırmaktadır. Arazi örtüsü ve arazi kullanımındaki (AÖAK) bu değişiklikler ekosistemlerin bütünlüğünü doğrudan etkilemektedir.

Olumsuz ekolojik etkilerin yanısıra, iklim değişikliği ile birlikte seraların sele maruz kalması sonucunda üreticilerin ekonomik ve sosyal sorunlarla karşı karşıya kalması gibi problemler de ortaya çıkmaktadır. Bu durum üretim sistemini sürdürülemez hâle getirirken bölge ekolojisini ve ekonomisini de tehlikeye atmaktadır.

Uzaktan Algılama teknolojisi, sinoptik veri avantajı, yüksek spektral ve zamansal çözünürlüğü ile tarım sektörünün periyodik olarak izlenmesine olanak sağlamaktadır. Sera alanlarının uydu görüntüleri kullanılarak çalışılması, daha iyi yönetim stratejileri sunmak açısından önemli bir yer tutmasının yanısıra, seraların iklim ve çevre üzerindeki etkileri hakkında bilgi edinilmesi ve ekonomik çıktılarının iyileştirilmesi için mekânsal dağılımının izlenmesinde en uygun yaklaşım olarak görülmektedir.

Bu tezde, seraların belirlenmesi amacıyla, literatürde daha iyi haritalama doğruluğuna ulaştığı belirtilen Obje Tabanlı Görüntü Analizi (OBIA) yaklaşımından yararlanılarak farklı sorulara yanıt aranmıştır. Bu kapsamda, tezin birinci bölümününde plastik seraların tarımsal üretimdeki önemi açıklanarak, ekonomik avantajları ve ekolojik dezavanlajları belirtilmiştir. Bunun devamında konu ile ilgili literatür araştırması sunulmuş ve tezin hedefleri verilmiştir. İkinci bölümde, çalışma alanları ve bu çalışma alanlarına ait veri setleri verilmiştir. Tezin üçüncü bölümünde, öncelikle tezin deneysel tasarım şeması ve çalışmada kullanılan yöntemler açıklanmıştır. Dördüncü

bölümde, çalışmanın üç temel aşamasını oluşturan görüntü segmentasyonu, özellik çıkarımı ve değerlendirilmesi ve son olarak yeni nesil topluluk öğrenme algoritmaları kullanılarak sera sınıflandırması üzerine yapılan araştırmaların sonuçları verilmiştir. Tezin beşinci bölümünde, sonuçlar detaylı olarak tartışılmış, ve son bölüm olan altıncı bölümde elde edilen tüm sonuçlar değerlendirilerek konu ile ilgili öneriler verilmiştir.

OBIA metodolojisinin birinci adımını oluşturan görüntü segmentasyonunda, plastik seraların segmentasyonu için iki önemli soruya yanıt aranmıştır. Bu sorulardan ilki, plastik sera segmentasyonun değerlendirilmesinde kontrollü segmentasyon kalitesi değerlendirme metriklerinden hangisinin daha iyi performansa sahip olduğudur. Bu araştırma sorusuna cevap bulmak için segmentasyon metriklerinin kullanıcı yorumları ile birlikte değerlendirildiği bir deneysel tasarım oluşturulmuştur. Bu aşamada, öncelikle farklı mekansal çözünürlük (orta ve yüksek mekansal çözünürlük), mevsim (yaz ve kış), çalışma alanı (Almería (İspanya) ve Antalya (Türkiye)) ve yantısım depolama ölçeğinden (16Bit ve Yüzde) oluşan on altı faklı veri setlerinden çok çözünürlüklü segmentasyon (Multiresolution segmentation, MRS) algoritması kullanılarak değişen sayıda segmentasyon çıktıları oluşturulmuştur. Bu çıktılar, altı farklı yorumlayıcı tarafından değerlendirilerek, her bir veri seti için segmentasyon çıktıları sera objelerini en iyi temsil edenden en zayıf olana doğru sıralanmıştır. Yorumlama sonuçları, her bir segmentasyon çıktısı için hesaplanan sekiz metrik ile karşılaştırılarak değerlendirilmiştir. Değerlendirmeler sonucunda, modifiye edilmiş öklit uzaklığı (Modified Euclidean Distance 2, MED2) metriğinin sera segmentasyonunun değerlendirilmesinde en başarılı metrik olduğu sonucuna ulaşılmıştır. Ek olarak bu metriğin hesaplanmasında kullanılan AssesSeg ücretsiz olarak erişilebilen ve birden çok segmentasyon çıktısının tek seferde değerlendirilmesini sağlayan bir araçtır, ki bu da erişilebilirliğini kolaylaştırmaktadır. Öte yandan, Uygunluk (Fitness) ve F ölçeği (F measure) araştırılan diğer metriklere oranla en iyi segmentasyon çıktısını belirlemede daha başarısız olmuşlardır. Ayrıca, farklı faktörlerin görsel yorumlama sonuçlarına etkisi istatistiksel olarak incelenmiştir. Bu incelemeler sonucunda, yantısım depolama ölçeğinin görsel yorumlamada önemli bir faktör olduğu ortaya çıkmıştır. Detaylı olarak Yüzde formatını kullanılarak oluşturulan segmentasyon çıktılarını değerlendirirken yorumlayıcıların daha çok hemfikir olduğu, dolayısıyla bu veri tipini daha rahat yorumladıkları sonucuna ulaşılmıştır.

Segmentasyon aşamasının ikinci adımında, hangi faktörlerin veya etkileşimlerinin sera segmentasyonu üzerinde ne kadar etkili olduğu araştırılmıştır. Bu soruya yanıt aramak için, on altı farklı veri setinden yaklaşık 4,000 adet segmentasyon çıktısı üretilmiş ve MED2 değerleri hesaplanmıştır. Her bir veri setindeki her bir şekil parametresi için en iyi MED2 değerine ulaşan değerler belirlenmiş, ve istatistiksel olarak varyans analizi ile test edilmiştir. Veri setlerinden hesaplanan segmentasyon çıktıları, optimal ölçek parametrelerinin Yüzde formatında birbirine yakın değerler alarak kümelendiğini, 16Bit formatında ise daha geniş aralıkta değerler aldığını göstermiştir. Bu durum Yüzde formatından elde edilecek segmentasyon çıktıları için en uygun ölçek parametresinin belirlenmesinin daha kolay olacağını göstermiştir. Ek olarak, istatistiksel testler farklı yantısım depolama ölçeği formatlarından hesaplanan segmentasyon doğruluğunun şekil parametresine doğrudan bağlı olduğunu göstermiştir. Yüzde formatında azalan şekil parametresi ile segmentasyon doğruluğu artarken, 16Bit formatında bu durumun tam tersi olduğu görülmüştür. Sonuçlar, yantısım depolama ölçeği formatına bağlı olarak şekil parametresi seçiminin oldukça önemli olduğuna işaret etmiştir. Özet olarak, Yüzde formatının MRS algoritması ile sera segmentasyonu için uygun veri formatı olduğu, ve buna ek olarak Yüzde formatınında düşük şekil parametrelerinin tercih edilmesi gerektiği ortaya konulmuştur.

Tezin ikinci aşamasında, farklı özellik uzayı yöntemlerinin ve özellik uzayı boyutunun sınıflandırmayı doğruluk ve zaman açısından etkilediği hipotezi oluşturulmuştur. Bu hipoteze bağlı olarak, Almeria ve Antalya çalışma alanlarına ait Sentinel-2 görüntülerinden toplam 128 özellik elde edilmiş ve farklı özellik uzayı değerlendirme yöntemleri uygulanarak sınıflandırma performansı Rastgele Orman (RO) algortitması ile değerlendirilmiştir. Bu değerlendirme sonucunda, özellik uzayının indirgenmesinin doğruluk üzerinde doğrudan etkisinin olduğu görülmüştür. Ayrıca, özellik uzayı boyutunun azaltılmasının sınıflandırma algoritmasının çalıştırılması için gereken süreyi önemli ölçüde azalttığı belirlenmiştir. İncelenen özellik uzayı değerlendirme algoritmalarından, RO ve özyinelemeli özellik eleme (Recursive Feature Elimination, RFE) -RO (RFE-RO) algoritmalarının sınıflandırma doğruluğu ve yöntemin çalıştırılması için gereken zaman açısından daha uygun olduğu sonucuna ulaşılmıştır. Bundan başka, bu algoritmaların özellik uzayı değişimine sınıflandırma doğruluğu açısından daha az bağımlı olduğu, fakat özellik uzayını azaltmanın hesaplama süresini önemli ölçüde azalttığı tespit edilmiştir.

Ayrıca, segmentlerden elde edilen ve spektral, dokusal, geometrik özellikler ve spektral indisleri içeren toplam 128 özellik arasından, RF ve RFE-RF yöntemlerine göre Plastik Sera İndisi (Plastic GreenHouse Index, PGHI) ve Normalize Fark Bitki İndisinin (Normalized Difference Vegetation Index, NDVI) seraların belirlenmesi ile ilişkili indisler olduğu tespit edilmiştir. Detaylı olarak, Almería çalışma alanında PGHI (minimum), ve NDVI (maksimum), Antalya çalışma alanında ise PGHI (ortalama) ve PGHI (medyan) değerlerinin seraların belirlenmesinde önemli özellikler olduğu belirlenmiştir. Sonuç olarak, seraların sınıflandırılması amacıyla gerçekleştirilecek çalışmalarda PGHI ve NDVI gibi indislerin özellik uzayına dahil edilmesi gerekliliği ve hesaplama süresinin azaltılması açısından RO ve RFE-RO gibi özellik uzayı yöntemlerinden birinin uygulanması bu aşamanın temel çıktılarıdır.

Tezin üçüncü ve son aşamasında yeni nesil topluluk öğrenme algoritmalarının seraların sınıflandırması için etkinliği test edilmiştir. Deneysel sonuçlara göre, Kategorik Artırma (Categorical Boosting, Catboost), RO ve Destek Vektör Makinaları (DVM) algoritmaları incelenen her iki çalışma alanında da (Almería ve Antalya) iyi performans göstermişlerdir, fakat CatBoost and DVM için gereken uygulama süresi incelenen diğer tüm algoritmalardan fazladır. K-En Yakın Komşuluk (K-Nearest Neighbor, KNN) and Uyarlanabilir Artırma (Adaptive Boosting, AdaBoost) algoritmaları her iki çalışma alanında da daha düşük sınıflandırma performansına ulaşmışlardır. Bu algoritmalara ek olarak, hafif gradyan artırma makineleri (Light Gradient Boosting Machines, LightGBM) algoritması her iki çalışma alanında %90 üzerinde F1 skoruna oldukça kısa sürede ulaşmıştır. Özetle, hesaplama süresi ve sınıflandırma doğruluğu göz önünde bulundurulduğunda, RO ve LightGBM bu çalışmada öne çıkan iki algoritmadır. Yine de, sınıflandırma algoritmasının seçiminin uygulama amacına bağlı olduğu unutulmamalıdır.

Genel olarak, bu tez çalışması kapsamında nesne tabanlı sınıflandırma yaklaşımını oluşturan üç aşamada en iyi sera belirleme yaklaşımına ulaşmak için üç faklı adımda karşılaşılabilecek sorulara yanıt aranmıştır. Uydu görüntülerinden seraların belirlenmesi, Akdeniz Havzasında yer alan iki seracılık faaliyetlerinin yoğun olarak yürütüldüğü iki önemli çalışma alanında gerçekleştirilmiştir. Sınıflandırma algoritmalarından elde edilen çıktılar açık erişimli algoritmaların nesne tabanlı sınıflandırma yaklaşımınına entegrasyonunun uygun ve ümit verici olduğunu da ortaya koymuştur. Bu çıktılar seçilen test bölgelerine ait olsa da, elde edilen bulguların büyük ölçekte genelleştirilmesi için önemli çıktılar sunmaktadır. Seraların çevre üzerindeki olumsuz etkilerini minimize etmek ve ekonomik getirilerini artırmak için mekânsal dağılımının belirlenmesi, sürdürülebilir tarım hedeflerine ulaşılması açısından plancılar ve karar vericiler için önemli bir katkı sağlayacaktır. Bu nedenle, seraların uzaktan algılama verileri kullanılarak mekânsal dağılımının belirlenmesi, arazi kullanımındaki gelişmeleri analiz etmek ve tarımsal üretime rehberlik etmek için uygulama açısından büyük öneme sahiptir.

1. INTRODUCTION

The human population, which would reach 9 billion in 2050, is expected to put unprecedented pressure on natural resources and agricultural systems as food demand increases (Aznar-Sanchez et al., 2020). Therefore, one of the most significant problems that human beings must deal with is the food supply (Hasan et al., 2018). In this context, the concept of sustainability gains importance. Sustainable development, which includes the economic, social, and environmental dimensions, is characterized as considering future generations' needs while meeting current needs (Brundtland Commission, 1987). Besides, with the Food and Agricultural Organization of the United Nations declaration regarding the requirement to raise food production to fulfill the increasing population's nutritional needs, the term "sustainable intensification" was started to be used in 2008 (Food and Agriculture Organization of the United Nations, 2008). Sustainable intensification of agriculture allows for improving food production and promoting sustainable development (Aznar-Sanchez et al., 2020).

Greenhouse cultivation is one of the best ways to accomplish sustainable intensification in agriculture since it offers a viable alternative for increasing production on the current agricultural land area. In recent years, the intensification of agricultural greenhouses (AG) has met the rising demand for resource-intensive diets (Tilman et al., 2011). AGs allow the cultivation of plants in adverse weather conditions and out of season, enabling year-round production. Besides, it ensures applying a protection management approach by providing better control over pests and diseases. Thus, AGs make a significant contribution to the sustainable intensification of agriculture.

In recent decades, greenhouses have expanded rapidly and changed the agricultural landscape in several regions, particularly in China, Europe, North Africa, and the Middle East (Chaofan et al., 2016). Notably, plastic film-covered agricultural greenhouses, which constitute the majority of greenhouse material, including plastic-covered greenhouses (PCG), walk-in tunnels (high tunnels), low tunnels, and plastic-mulched farmland (PMF), are unwaveringly expanding worldwide at a rate of close to 20% per year (Jiménez-Lao et al., 2020).

Such agricultural activities have some limitations and disadvantages to the local and regional environment. Firstly, the intensification of agriculture is accomplished with high levels of chemical inputs that can pollute the environment and affect the health of the population (Aznar-Sanchez et al., 2020). Due to fertilizer leakage, it can contaminate aquifers and may cause eutrophication of surface water (Lu et al., 2014). Secondly, plastic covers reduce plant biodiversity by altering the pollination cycle and disrupting soil structure by leaving plastic film residues. They also generate large amounts of plastic and crop waste. Lastly, the growing demand for agriculture due to the increasing world population causes the transformation of the primary land cover type into intensive agricultural areas. The use of agricultural plastic greenhouses is increasing worldwide, and it significantly accelerates this transformation. Changes in land use and land cover (LULC) have a direct impact on ecosystems' state and integrity (Jiménez-Lao et al., 2020).

Together with these facts, the construction of AGs and the use of mulching films are not stated to the local government in many developing countries, thus, making it difficult for relevant departments to obtain information regarding the spatial distribution of plastic-covered areas (Feng et al., 2021).

Considering both positive economic and adverse ecologic outcomes, it has become a requirement to understand and monitor the spatio-temporal distribution of AGs in-depth to offer solutions to the problems and develop better management strategies. Remote sensing seems to be the exclusively suitable to obtain information on the effect of the spatial distribution of greenhouses on climate and environment, as it provides monitoring in a wide geographic area and extensive temporal archive (Aguilar et al., 2015; Jiménez-Lao et al., 2020). However, mapping AGs with remote sensing data is highly challenging due to the exclusive characteristics of greenhouses. Because the spectral signature of AGs is highly dependent on the type of materials, crop types under the cover and phenological status, age, conservation status, and local agricultural practices (Jiménez-Lao et al., 2020).

1.1 Literature Review

As the areal extent of the AGs expanded in different parts of the world, mapping of the AGs through remote sensing images has been attempted in several studies since 2006, and the number is incrementally increasing. AG mapping studies have been carried out by considering various input data, image processing approaches, and algorithms.

Greenhouse mapping studies were performed initially with high-resolution data. Some preliminary work on AG mapping was carried out by Agüera et al. (2006). They detected greenhouses from orthorectified aerial and QuickBird images using the pixel-based maximum likelihood classification method in Spain's southeastern region. Similarly, Sönmez and Sarı (2006) extracted greenhouses from the IKONOS image using on-screen-digitizing to construct a geographic information systems (GIS) for the greenhouses in Antalya, Turkey.

Some other studies aimed to increase per-pixel mapping accuracy and compare different classifiers through supervised approaches. Agüera et al. (2008) attempted to improve per-pixel plastic greenhouse mapping accuracy using texture analysis from QuickBird and IKONOS images of Spain. Likewise, Arcidiacono and Porto (2011) investigated the contribution of the texture information obtained from the Quickbird image to the accuracy of determining crop-shelter coverage areas in Italy. Koc-San (2013) intended to compare the supervised classification methods for mapping greenhouses, which are maximum likelihood, random forest (RF), and support vector machines (SVM). The author also aimed to assess plastic and glass greenhouses detecting and discriminating ability of WorldView-2 image in Antalya, Turkey.

In addition to high-resolution data, AG mapping studies were carried out using medium spatial resolution data, especially after Landsat data became freely available. The main reasons for including medium spatial resolution data in AG mapping studies are the satellites' wide swath width, the high temporal resolution, and free availability. In this manner, Lu et al. (2014) claimed that high spatial resolution images are not suitable for mapping PMF in a large geographic area due to their high cost and infrequent temporal coverage. For this reason, they aimed to extract the transparent PMF from a multi-temporal Landsat-5 Thematic Mapper (TM) image by proposing a decision-tree (DT) classifier over a large geographic area. As a result, they obtained an overall accuracy changing from 85.27% to 97.82% for the selected years. The same research team also proposed a threshold model reaching an overall accuracy of over 84% to detect plastic-mulched farmlands through multi-temporal MODIS data (Lu et al., 2015). Likewise, Novelli and Tarantino (2015) aimed to map plastic cover vineyards using Landsat-8 Operational Land Imagery (OLI) and Thermal Infrared Sensor (TIRs) data and spectral indices proposed in the research. They determined a threshold for each proposed index and reached an overall accuracy of over 80 % in four test areas. These studies focused on determining greenhouses in the selected regions by specifying a threshold value. The most critical issue is that threshold values are determined experimentally, and the greenhouse types and used material, crop types, or local agricultural practices vary by country, which can change the selected thresholds for each country, even for each region.

The increasing use of plastic in agriculture has revealed the need to map and provide information on the materials used. For this reason, Levin et al. (2007) investigated the plastic materials used in constructing plastic greenhouses in Israel by integrating field spectroradiometer and remote sensing data. Similar to previous studies, they used high spatial resolution data (AISA-ES hyperspectral sensor with 1-m resolution) and investigated the AG mapping potential of medium spatial resolution Landsat data (pan-sharpened to 15-m) through pixel-based image classification methods. They found that the best spectral range for plastic mapping is around 1732 nm, where other minerals, soil, vegetation, or atmospheric attenuation do not coincide with the spectral properties of plastic materials. They also stated that the spatial resolution of the sensor should be equal to or higher than 8-16 meters, as most of the greenhouses in Israel are smaller than 3200 m2.

The greenhouse mapping performances of unsupervised classification methods with pixel-based analysis are also evaluated in the literature. Taşdemir and Koc-San (2014) aimed to map greenhouses using spectral features and Gabour textural features extracted from the WorldView-2 image through an unsupervised image classification method. In detail, they clustered the extracted features with an approximate spectral clustering method based on local density-based similarity, then obtained clusters were labeled as greenhouses and others. They reached an overall accuracy of 87.30% with the proposed methodology. Similarly, Pala et al. (2015) extracted greenhouses from the WorldView-2 image using an approximate spectral clustering ensemble based on the hybrid geodesic similarity criterion, reaching an overall accuracy of 87.8%. Lately, in addition to this research, several numbers of studies have attempted to map AG using pixel-based approaches (Hao et al., 2019; Hasituya et al., 2016; Hasituya et al., 2020; Liu et al., 2020; Ou et al., 2019; Perilla & Mas, 2019; Shi et al., 2020; Xiong et al., 2019).

The studies mentioned above have focused on AG mapping considering the input remote sensing data and pixel-based unsupervised or supervised classification methods. However, one significant drawback to adopting the pixel-based procedures is that it analyzes each pixel's spectral properties without considering spatial or contextual properties related to the pixel. This can result in misclassified pixels or unwanted detail in groups of pixels that must be considered together as a single object. Confusion in the classification process can be decreased by the capability to handle contextual information (Tarantino & Figorito, 2012). In this manner, object-based image analysis (OBIA) helps to reduce the "salt-and-pepper" effect and to employ other object properties together with the traditional spectral characteristics (Chaofan et al., 2016). Jobin et al. (2008) pointed out that one of the significant advantages of OBIA is the potential to include ancillary data along with object-related properties such as shape, texture, and context or relationship beyond purely spectral information. In fact, Chaofan et al. (2016) reported that object-based classification yielded a significant improvement compared with the traditional per-pixel classification for greenhouse mapping.

As of 2010, OBIA approaches have been proposed for AGs determination through remote sensing images. Arcidiacono and Porto (2010) analyzed the crop shelter classification ability of pixel-based and object-based methods. The authors indicated that object-oriented methods offer more accurate outcomes and diminish the computation time of image classification. Tarantino and Figorito (2012) conducted the initial research to address the adverse effects of plastic-covered vineyard production in Italy. They used true color aerial images, multi-resolution segmentation, and the Nearest Neighbor (NN) classifier to identify plastic greenhouses. The authors used feature space optimization to identify the best parameters for the classification procedure. They applied their methodology in eight test areas and achieved overall accuracies ranging from 83.00% to 93.00%. In another study, Aguilar et al. (2014) proposed an object-based AG classification methodology through stereo pairs acquired by very high-resolution GeoEye-1 and WorldView-2 images of Almería, Spain. The authors used manual digitizing outputs as segmentation and created ten different scenarios according to the features derived from image objects. Using the NN and SVM classifiers, the authors reached an overall accuracy ranging from 87.91% to 89.01% with NN and from 84.07% to 87.36% with SVM. Novelli et al. (2016) tested the greenhouse mapping performance of Landsat-8 and Sentinel-2 Multispectral Imagery (MSI) images through OBIA with a RF classifier. They also used WorldView-2 images to improve multi-resolution image segmentation and expand features used for the OBIA. The researchers obtained an overall accuracy ranging between 89.00% to 93.40%. Besides these researches, Bektas Balcik et al. (2020) evaluated the AG mapping performances of Sentinel-2 and SPOT-7 images and different commonly used classifiers (k-nearest neighbor (KNN), SVM, RF). Aguilar et al. (2021) examined the potential of visible NIR (VNIR) and shortwave infrared (SWIR) bands of Worldview-3 (WV3) for plastic greenhouse delineation with an OBIA approach. It was stated that indices derived with SWIR bands have higher predictive power for greenhouse mapping.

Reducing the number of features will decrease the model complexity since most features tend to be correlated. Increasing feature diversity in OBIA made the subjective selection of features difficult. Several techniques have been applied to efficiently reduce the feature space from statistical analysis to machine learning and deep learning. Ma et al. (2017a) evaluated the efficiency of SVM and RF algorithms in determining LULC with remote sensing images through different feature selection approaches. Researchers analyzed the methods under two categories; feature importance (Gain ratio, chi-squared, SVM-RFE (SVM-Recursive Feature Elimination, RFE), Relief-F and RF) and feature subset (Correlation-based Feature Selection, RF wrapper, SVM wrapper) methods. It has been stated that feature importance methods are more suitable for the object-based classification approach since the best classification accuracy is achieved with these methods.

In addition to optical data, several studies have been performed to reveal the contribution of radar images to AG mapping (Hasituya et al., 2017; Hasituya et al., 2020; Liu et al., 2019; Lu et al., 2018; Tuya et al., 2021). Studies using radar data have shown that the radar data alone could not achieve high accuracy for AG mapping. For example, Hasituya et al. (2017) obtained an approximately 75% overall accuracy through the pixel-based study conducted with Radarsat-2. On the other hand, Lu et al. (2018) claimed that AG mapping using synthetic aperture radar (SAR) data alone improved accuracy significantly by the object-based approach. It was also affirmed that integrating Sentinel-1 SAR data and Sentinel-2 optical data increased accuracy by 1-3% through OBIA. Furthermore, the PMF mapping potential of Pléiades and Radarsat-2 data has been investigated by Tuya et al. (2021) through OBIA and RF. The research revealed that the Pléiades data reached a higher overall accuracy than the Radarsat-2 data.

OBIA approach is also utilized for the discrimination of different greenhouse structures (such as low plastic tunnels, net-house or circular arched shape) (Tiwari et al., 2020), greenhouse crop identification (Aguilar et al., 2015; Nemmaoui et al., 2018), or assessment of plastic greenhouses landscape changes (González-Yebra et al., 2018).

There have been numerous studies to investigate AG detection considering the input remote sensing data (optical or radar), image classification methods (unsupervised or supervised, parametric or non-parametric, and machine learning or deep learning-based approaches), image processing approach (i.e., pixel-based or object-based), and single or multitemporal. Figure 1.1 shows the number of papers and research articles published on the AG mapping until February 2023, according to the Web of Science Core Collection. As seen from the increasing number of research, including 60 articles and 9 proceeding papers, AG mapping has recently received great attention.

In addition to the importance of AG mapping, another reason for the increasing number of studies in recent years is the availability of accessible, high-resolution data such as Sentinel-2 and the opportunity in the big data processing capability of platforms like Google Earth Engine (GEE). The GEE cloud platform has been the subject of mapping greenhouses with its ability to analyze large datasets. To illustrate, Lin et al. (2021) constructed an integrated classification algorithm for greenhouse detection in Jiangsu Province of China with the GEE platform and Landsat 8 images. The authors utilized the tree classifiers: classification and regression trees (CART), RF, and maximum entropy model with spectral, texture, and terrain features. The results yielded that the GEE platform provides the rapid mapping of large-scale greenhouses under complex terrain and higher accuracy with an integrated classification approach. In another research, Ou et al. (2021) developed an annual greenhouse mapping method for China from 1989 to 2018 on the GEE platform using Landsat images. The authors employed the RF classifier for image classification. It was concluded that the average User's Accuracy, Producer's Accuracy, and F1 score reached 96.56%, 86.64%, and 0.911, respectively.

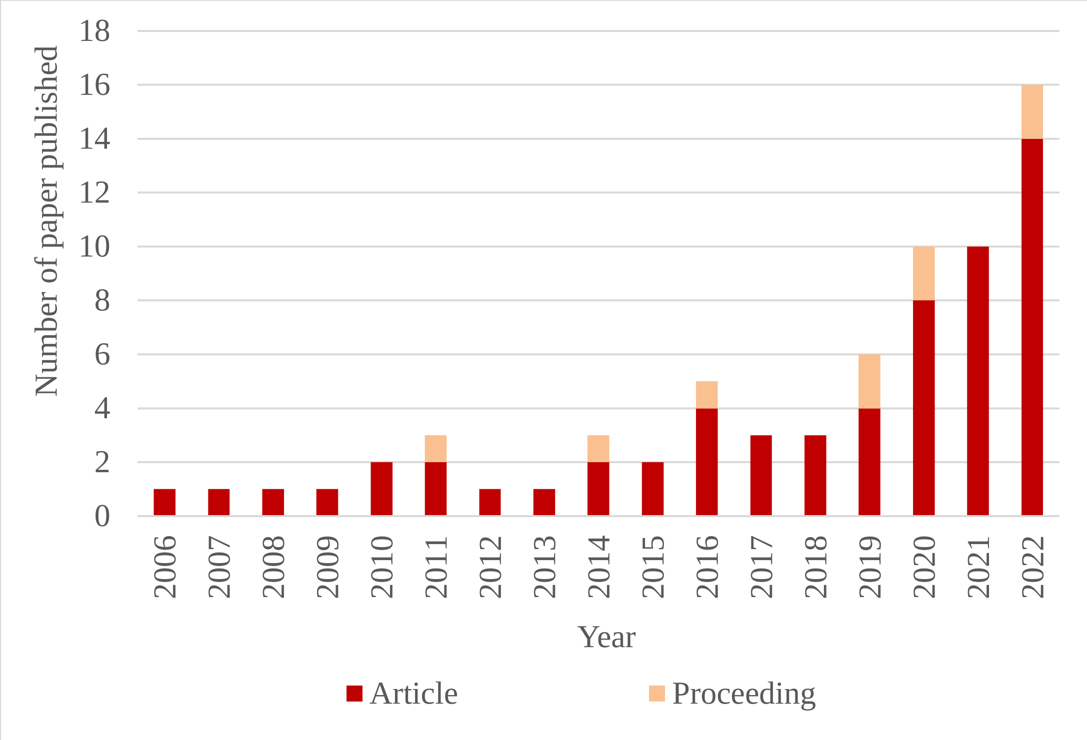

Figure 1.1 : The total number of research articles and conference proceedings published on greenhouse mapping through remote sensing images.

The recent advances in pattern recognition and computer vision also have provided opportunities for the detection of AGs. In this manner, Li et al. (2020) compared the three convolutional neural network (CNN) based models for greenhouse detection using Gaofen-1 and Gaofen-2 images. Liu et al. (2020) proposed a deep semi-supervised learning framework using Google Earth images for green plastic cover mapping. It should be stated that deep learning techniques have emerged as a research hotspot recently in the remote sensing field. For example, Feng et al. (2021) proposed a dilated and non-local CNN to identify the PCG and mulching films from Google Earth data. The suggested model comprises various multi-scale dilated convolution blocks and a non-local feature extraction module. They tested their model in two different test areas in China and Saudi Arabia and obtained an overall accuracy of 89.6% and 92.6% with the proposed model. The authors also pointed out that the dilated convolution could improve the classification accuracy by 2.7% compared to standard convolution. Chen et al. (2021) aimed to map the distribution of greenhouses in China using a deep learning method with high-resolution Google Earth images. The authors achieved a mean intersection over union of 97.20%. Ma et al. (2021a) presented a data-driven deep learning framework called dense object dual-task deep learning for large-scale greenhouse mapping. The proposed framework was tested in six test areas in China. It was reported that a performance increment of 1.8% has been obtained in mean average precision compared to the Faster R-CNN method.

In another research, Sun et al. (2021) proposed a greenhouse mapping approach with a one-dimensional CNN using two-temporal Sentinel-2 images with various seasonal characteristics. The authors claimed that the greenhouse reflectance changes during crop growth; moreover, the reflectance in red-edge and near-infrared bands significantly increases and then decreases during the whole crop growth period. Consequently, they pointed out that two-period images that included the difference in greenhouse reflectance were adequate for greenhouse mapping. Furthermore, the authors stated that the proposed approach yielded higher classification accuracy than SVM or RF.

Zhang et al. (2021) suggested a high-resolution boundary refined network to extract the greenhouses from Gaofen-2 images. The results show that the proposed network reveals an essential improvement in segmentation performance up to an IoU score of 94.89%. Ma et al. (2021b) introduced a multi-channel fused fully convolutional network to delineate greenhouses from SuperView-1 high-resolution remote sensing data. The suggested fully convolutional network was optimized by the optimal scale object-oriented segmentation results. As a result, it was indicated that the proposed model based on the optimal scale object-oriented segmentation preserves the edge details of the greenhouse and the precision and F1 score value are 92.68% and 0.94, respectively. The contribution of different algorithms has been investigated in several research (Chen et al., 2022; Feng et al., 2022; Li et al., 2022).

As can be observed from the findings, remote sensing-based mapping of this type of land cover is still awaiting due to the particular characteristics of greenhouses, as seen by the rising number of scientific works published, especially in the recent few years (Jiménez-Lao et al., 2020). These unique characteristics of AG depend on the following factors that significantly affect the spectral signature:

- the used plastic material (i.e., thickness, density, transparency, light dispersal, ultraviolet and infrared properties, anti-fog additives, and color)
- the seasonal use of greenhouses (e.g., during summer, covering materials may be painted white to protect plants against excessive radiation by lowering the temperature),
- the existence of vegetation inside the greenhouse, which changes the overall reflectance of the greenhouse,
- the view angle (i.e., the relationship between the light incidence angle and the remote sensor point of view) (Aguilar et al., 2014).

The above factors may bring different spectral signatures for the same land use type and cause serious confusion with non-greenhouse classes.

Ensemble learning algorithms have received more attention in the last few years due to their superiority over single classifiers regarding pattern recognition and classification performance among machine learning algorithms (Ustuner & Balik Sanli, 2019). Different bagging and boosting ensemble learning algorithms are frequently used (Belgiu & Drăguţ, 2016). Recently, extreme gradient boosting (XGBoost) and light gradient boosting machines (LightGBM) algorithms have been employed in remote sensing applications, specifically in agricultural product classification (Üstüner et al., 2020; Ustuner & Balik Sanli, 2019), gully detection (Wang et al., 2020) or invasive plant species detection (Muthoka et al., 2021).

XGBoost, developed by Chen and Guestrin (2016), is a popular method for classification in data science and remote sensing fields. For example, Muthoka et al. (2021) aimed to detect invasive plant species using the Sentinel-2 using ensemble machine learning classifiers, XGBoost, and RF. The results indicated that the Sentinel-2 spectral bands reached an overall accuracy of 80% and 84.4% for XGBoost and RF classifiers, respectively. The researchers also investigated the classification performance of combined spectral bands, vegetation, and topographic indices that reached an overall accuracy of 89.2% and 92.4% for XGBoost and RF classifiers. In another research, Abdi (2019) compared the LULC classification performance of SVM, RF, XGBoost, and deep learning using multi-temporal scenes from Sentinel-2 covering spring, summer, autumn, and winter conditions. The results yielded that SVM, XGBoost, RF, and DL reached an overall accuracy of 0.758, 0.751, 0.739, and

0.733, respectively. Hamedianfar et al. (2020) integrated an artificial neural network and particle swarm optimization to improve the learning process and determine the essential features and their importance using Worldview-3 satellite data. The researchers adopted an XGboost image classifier to obtain the LULC and tested it in three different test areas. The XGBoost classifier reached an overall accuracy of 91.68%, 89.54%, and 89.33% for the first, second, and third sites, respectively.

Furthermore, the XGBoost algorithm has been integrated within the OBIA framework in work conducted by Ding et al. (2021). They tested the artificial terrace mapping performance of three commonly-used machine-learning classifiers: XGBoost, RF, and KNN through OBIA. It was stated that RF reached the best overall accuracy with 95.60%, followed by 94.16% and 92.33% for XGBoost and KNN, respectively. Accordingly, it has been observed that the XGBoost algorithm reaches reasonable classification accuracy for different LULC classifications, although there is no superiority to other classifiers.

In addition to the XGBoost ensemble learning algorithm, the LightGBM has been included in studies lately. Furthermore, the LightGBM algorithm also has been used within the OBIA approach. To illustrate, Wang et al. (2020) aimed to detect gully erosion using open-source optical images (Google Earth images) through OBIA and LightGBM. The authors stated that the overall performance is suitable for gully mapping because of its high automation, low cost, and acceptable accuracy. Categorical Boosting (CatBoost) is another recently popular gradient boosting algorithm introduced by Prokhorenkova et al. (2017). Sahin (2020) examined landslide susceptibility modeling performance of different ensemble learning algorithms, Gradient Boosting (GB), CatBoost, XGBoost, LightGBM, and RF. The experiments yielded that the CatBoost reached the highest classification accuracy with 0.8503, followed by the XGBoost, LightGBM, GBM, and RF.

1.2 Purpose of the Thesis

The main purpose of the thesis is to propose an OBIA framework to determine the spatial distribution of the AGs in the selected test areas using remote sensing images. Greenhouses constitute a significant part of agricultural production, and the total greenhouse area continues to increase worldwide. It is reported that to achieve the sustainable food safety goal, food production must be improved significantly, and the ecological footprint of agriculture must be strictly decreased (Aznar-Sanchez et al., 2020). Therefore, determining and estimating the spatial distribution of AGs is essential for planners and policy-makers to increase crop yields while reducing the ecological footprint of these structures.

In detail, the OBIA framework consisted of three main steps; image segmentation, feature extraction, and object/image classification. However, a literature review on the detection of greenhouses with remote sensing data reveals that the efficiency of different feature space reduction methods has not been evaluated yet. In addition, the PCG classification performance of new-generation ensemble learning algorithms (XGBoost, LightGBM, and CatBoost) has not yet been evaluated. Besides, the integration of OBIA and new-generation ensemble learning is a promising approach in LULC, and the researches on this topic are limited.

For this purpose, the objectives of this thesis are; (i) to improve the segmentation step, (ii) to determine the most compelling feature space reduction algorithm in the feature selection step, and (iii) in the classification step, to test the performance of ensemble learning algorithms.

2. STUDY AREA AND DATA

2.1 Study Areas

Two study sites which cover a square area with a side of 3 km, located in Antalya (Turkey) and Almería (Spain), were selected to conduct the experiments. Figure 2.1. shows the location of the study sites.

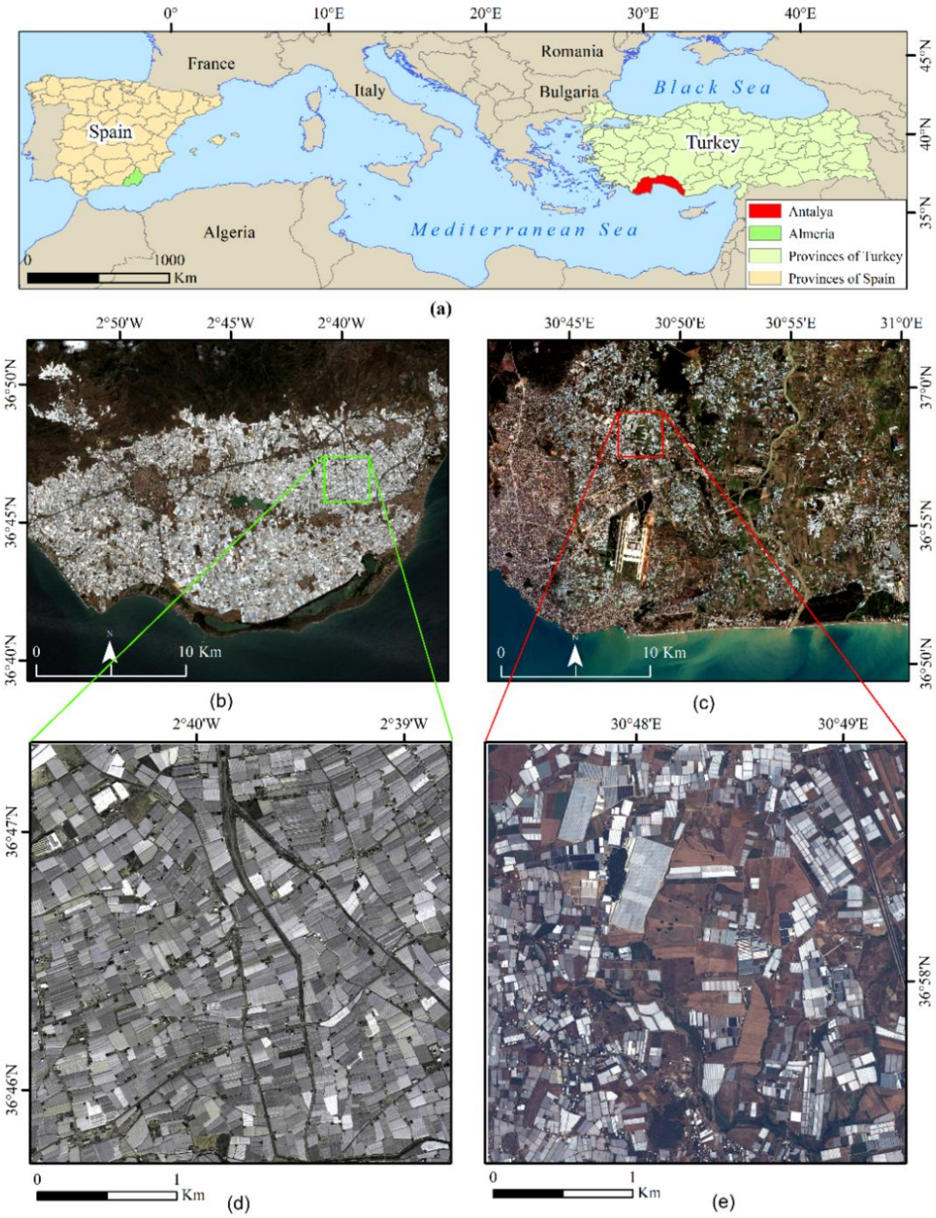

Figure 2.1: (a) Global location of the study areas, general overview of (b) Almería and (c) Antalya, and study sites in (d) Almería an (e) Antalya.

2.1.1 Antalya (Turkey)

The sample area in the Aksu district of Antalya was chosen as the first study site in the thesis. In the selected study site, two field studies were carried out in the Fatih neighborhood of Aksu District in March 2021 and August 2022. Sample photos from the study area are given in Figure 2.2. Types of greenhouses (plastic, glass, or covered with black nets or white painting) and the plants growing in them have been gathered. According to the field study, a total of 128 glass greenhouses were detected.

(a)

(b)

Figure 2.2: Sample (a) plastic and (b) glass greenhouses from Antalya.

The Aksu District is one of the districts where greenhouse production is most intense in Antalya. Most of the production in the district is vegetable production, as well as cut flowers, ornamental plants, and saplings. The economic income sources of the district are mainly based on agriculture and the agriculture industry (T.C. Aksu District Governorship, 2023). According to the Turkish Statistical Institute (Türkiye İstatistik Kurumu, TÜİK), 3,804,471 tons of vegetables (which is equivalent to 49% of the vegetable production in Turkey) were produced in greenhouses in Antalya, and 445,859 tons of this amount were produced in the Aksu district (TÜİK, 2020). In addition, most of the production in the district is exported. Therefore, the district is important for regional and national economies (Western Mediterranean Development Agency, 2019).

Besides, many greenhouses have been affected by floods due to the excessive rainfall in the district recently. In addition to the adverse ecological problems caused by unplanned and intensive greenhouse activities, the lack of a spatial management plan and climate change effects cause the greenhouses to be exposed to flooding, causing economic and social damage to the farmers.

2.1.2 Almería (Spain)

The second sample region is selected in Almería, located in southern Spain. This region is known as the "Sea of Plastic" or the "Poniente", one of the most significant concentrations of greenhouses in the world (Aguilar et al., 2016a). A field study was conducted in April 2022 in the selected study site in Almería. Sample photos from the field are given in Figure 2.3.

Figure 2.3: Sample plastic-covered greenhouses from Almería (Spain).

The area has a dense plastic-covered greenhouse concentration, and mostly tomato, pepper, cucumber, aubergine, melon, and watermelon are cultivated under the greenhouses (Aguilar et al., 2021; Aguilar et al., 2020). The spectral signatures of greenhouses in this region change over time due to cultivated plants under greenhouses (Novelli et al., 2016) and whitewashing activities (Aguilar et al., 2015).

Although there are different types of plastic covers in the region, the most frequently used covering materials are polyethylene films (e.g., low density, long life, thermic, with or without additives) and ethylene-vinyl acetate (EVA) copolymer (Aguilar et al., 2016a; Aguilar et al., 2015). These materials may have different thicknesses (180 µm or 200 µm) and colors (yellow, white, or green) (Aguilar et al., 2015).

2.2 Datasets

In the thesis, mainly two data types have been used; medium-resolution (Sentinel-2) and very high-resolution (SPOT-7 and Worldview-3) images.

2.2.1 Sentinel-2

Sentinel-2 Mission provides simultaneous and continuous monitoring of land and coastal areas with two identical satellites (Sentinel-2A and Sentinel-2B). The MSI sensor on Sentinel-2A and Sentinel-2B satellites acquired images from the visible region to the shortwave infrared region of the electromagnetic spectrum. Its temporal resolution is five days, thanks to its twin satellite configuration. It has a swath width of 290 km and acquires images with 13 spectral bands with different spatial resolutions (Sentinel-2 Products Specification Document, 2021). The specifications of Sentinel-2A and Sentinel-2B are given in Table 2.1.

Table 2.1 : Band specifications of Sentinel-2 MSI.

Band #	Band Name	Sentinel-2A		Sentinel-2B		Spatial Resolution (m)
		Central λ (nm)	Band Width (nm)	Central λ (nm)	Band Width (nm)	
B1	Coastal Blue	443.9	27	442.3	45	60
B2	Blue	496.6	98	492.1	98	10
B3	Green	560.0	45	559.0	46	10
B4	Red	664.5	38	665.0	39	10
B5	VRE-1	703.9	19	703.8	20	20
B6	VRE-2	740.2	18	739.1	18	20
B7	VRE-3	782.5	28	779.7	28	20
B8	NIR	835.1	145	833.0	133	10
B8A	Narrow NIR	864.8	33	864.0	32	20
B11	SWIR-1	1613.7	143	1610.4	141	20
B12	SWIR-2	2202.4	242	2185.7	238	20

λ: wavelength, VRE: Vegetation red edge, NIR: Near infrared, SWIR: Shortwave infrared

In the thesis, four cloud-free Sentinel-2 Level 2A (surface reflectance) images corresponding to Almería and Antalya (covering two seasons, winter and summer) were used (Table 2.2).

Table 2.2 : The dates of the used Sentinel-2 data.

Study area	Acquisition date and sensor
Almería	26.12.2020 (Sentinel-2A) - 14.06.2020 (Sentinel-2B)
Antalya	01.02.2019 (Sentinel-2B) - 06.07.2019 (Sentinel-2A)

Image acquisition dates were chosen considering the data availability and being in two different seasons since the reflectance of greenhouses had changed due to whitewashing activities.

2.2.2 SPOT-7

The SPOT-7, launched by AIRBUS Defense & Space in 2014, acquires images in red, green, blue, and NIR bands with a spatial resolution of 6 m and a panchromatic band with a spatial resolution of 1.5 m. The radiometric resolution of the SPOT-7 image is 12 bits. Two SPOT-7 images covering the Antalya study site were used in the thesis, which were orthorectified products. The images had a +9.29° off-nadir angle for the 05.02.2019 (winter) dated image and a +20.61° off-nadir angle for the 04.07.2019 (summer) dated image. The SPOT-7 images were stored as 16-bit products.

2.2.3 Worldview-3

WorldView-3, operated by DigitalGlobe Inc and launched in 2014, is a high-spatial-resolution optical satellite. Eight visible and near-infrared bands (VNIR) with a spatial resolution of 1.24 m, two shortwave infrared bands (SWIR) with a resolution of 3.7 m, and one panchromatic band with a spatial resolution of 0.31 m presented with this satellite at the nadir. The dynamic range of WorldView-3 images is 11 bits without dynamic range adjustment (Digital Globe, 2014).

The WorldView-3images covering the Almería study area were in Ortho Ready Standard Level-2A (ORS2A), and the final product has a ground sample distance (GSD) of 0.3 m, 1.2 m, and 3.7 m for PAN, VNIR, and SWIR, respectively.

Therefore, the two WorldView-3 images covering the Almería study area were used in the thesis. The images taken on June 11, 2020 (summer) and December 25, 2020 (winter) were used, which are the closest dates to the corresponding Sentinel-2 images. Moreover, the images were acquired with a mean off-nadir angle of 1.5° for the 25.12.2020 dated image and 27.6° for the 11.06.2020 dated image.

3. EXPERIMENTAL DESIGN AND METHODS

The methodological flowchart of the thesis is given in Figure 3.1. To begin with, data required for the analyses were collected as given in Chapter 2, and preprocessing was completed.

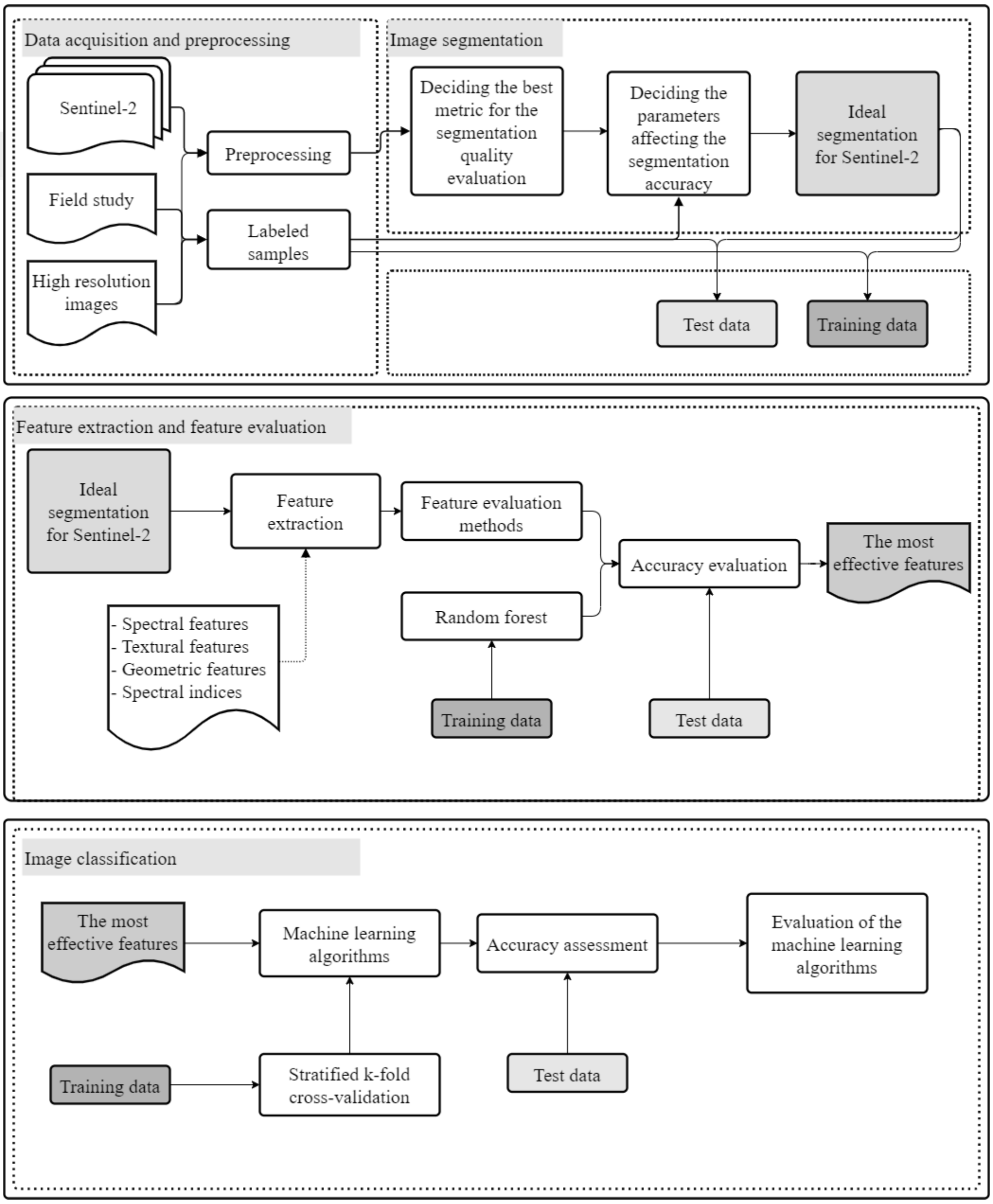

Figure 3.1 : Methodological flowchart of the thesis.

Then, as the first stage of the thesis related to image segmentation, comprehensive experiments were designed on the basis of PCG segmentation. Following this, the features which were evaluated through algorithms were extracted, and different feature space algorithms were assessed. In the last section, some machine learning-based image classification algorithms were evaluated through the OBIA approach.

3.1 Image Preprocessing

Eight cloud-free satellite images were used, including two images from WorldView-3 and two from Sentinel-2 for the Almería study site and two from SPOT-7 and two from the Sentinel-2 Antalya study site. After images were obtained, preprocessing steps were completed. It should be noted that high resolution images (WorldView-3 and SPOT-7) were mainly used to extract the ground truth for the analysis, except in the experiments in the segmentation step.

First, the WorldView-3 and SPOT-7 images were pan-sharpened using the PAN and VNIR bands. The two Worldview-3 images were pan-sharpened to 0.3 m GSD, while the two SPOT-7 images were pan-sharpened to 1.5 m GSD using the PANSHARP module of Catalyst v. 2222.0.5 (PCI Geomatics, Richmond Hill, ON, Canada).

Then, the atmospheric correction was performed on the WorldView-3 and SPOT-7 through the ATCOR module based on the MODTRAN (MODerate resolution atmospheric TRANsmission) radiative transfer code (Berk et al., 1998) in Catalyst v. 2222.0.5. Besides, since the Sentinel-2 images were already downloaded as Level-2A, the atmospheric correction was not performed for these images.

Lastly, the original Level-2A Sentinel-2 images and their corresponding High Resolution (HR) were co-registered using the AROSICS library available through the python programming language (Scheffler et al., 2017).

3.2 Extraction of the Reference PCG Polygons

A reference dataset corresponding to Almería and Antalya study sites was manually digitized on HR Worldview-3 and SPOT-7 ortho images. It should be noted that the same person completed all digitizing processes, and then controlled to ensure all the individual greenhouses were correctly digitized (Figure 3.2). In the Antalya study site, greenhouses made up of glass were also detected based on the field visit and high-resolution Google Earth images.

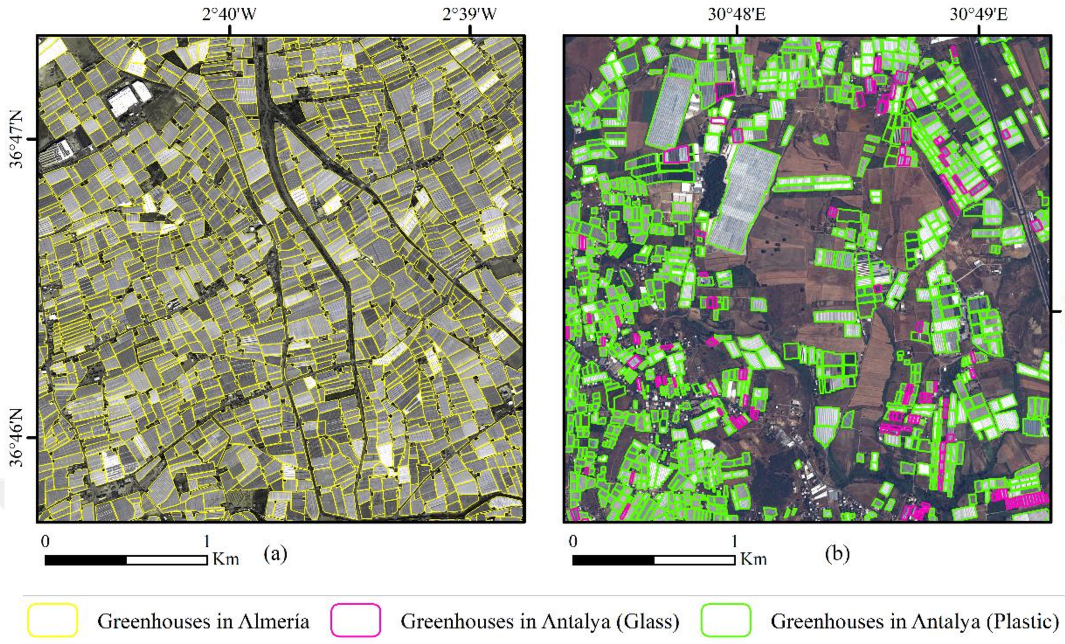

Figure 3.2 : On-screen digitized greenhouses in (a) Almería and (b) Antalya study site.

The on-screen digitized greenhouses were used in both image segmentation, feature space evaluation, and image classification stages. The details of the used samples were given in related sections.

3.3 Image Segmentation

Image segmentation, the first and most crucial stage in OBIA, is the process of dividing the image into homogeneous and semantically relevant pixel groups. This division can depend on the color, spectral characteristics, texture, or shape of objects (Blaschke, 2010). Although many other image segmentation algorithms have been developed in the fields of image processing and computer vision, the multi-resolution segmentation (MRS) algorithm has been broadly used and successfully utilized in various remote sensing applications. This algorithm is available through the eCognition software (Trimble, Munich, Germany). In fact, Ma et al. (2017b) reported that 80.9% of the investigated 254 case studies adopted the eCognition software for the segmentation. In fact, the MRS algorithm has been effectively used in object-based greenhouse mapping studies with several inputs (Aguilar et al., 2016; Aguilar et al., 2022; Bektas

Balcik et al., 2020; Novelli et al., 2016; Tarantino & Figorito, 2012). Thus, in this thesis, the MRS algorithm is also used to segment the images.

The MRS outputs depend on several parameters that the user must optimally specify, and the selection of these parameters depends on the purpose of the research. This is due mainly to the fact that different land objects or segments have spectrally and structurally varied, which means that distinct land objects may have different optimal segmentation values (Hay et al., 2003; Hossain & Chen, 2019; Jozdani & Chen, 2020; Tian & Chen, 2007). However, choosing the best segmentation is complicated since fuzzy borders or image noise may make it difficult to obtain an optimal segmentation for even a single land object (Costa et al., 2008). In this case, it is necessary to create a framework in which the quality of the segmentation result can be evaluated to ensure the generalizability of the image segmentation. As a result, segmentation quality can be evaluated iteratively until the best segmentation is achieved (Jozdani & Chen, 2020). Therefore the parameters for the MRS algorithm have been selected based on the iterative process of evaluation of segmentation quality.

3.3.1 Experimental design for the image segmentation stage

Two-step experiment were designed for the image segmentation stage of the thesis. These experiments were mainly designed with different types of image sources, including different study sites (i.e., Almería and Antalya), satellite images (Worldview-3, Sentinel-2, and SPOT -7), and seasons (summer and winter). Besides these sources, it is important to keep in mind that digital formats, i.e., reflectance storage scales (RSS), were also analyzed. In detail, the images were computed in two ways; 16 Bit Reflectance (which is referred as 16Bit in the thesis), which have units from zero through 10,000 stored values, and Percent Reflectance (which is referred as Percent in the thesis), which have reflectance units from zero through 100 percent stored values.

The first step was designed to evaluate the efficiency of some metrics for the PCG segmentation, in which eight segmentation accuracy evaluation metrics were investigated to determine the with the MRS method. To begin with, some MRS outputs were systematically generated considering different total segment numbers and sixteen datasets corresponding to different study sites (i.e., Almería and Antalya), satellite images (Worldview-3, Sentinel-2, and SPOT -7), seasons (summer and winter), and digital formats (16-bit and Percent). Then, these outputs were asked to be evaluated by six experienced interpreters by ranking the segmentation from 1 (best) to 10 (worst). In this ranking, it was requested to check the segmentation quality in terms of matching between image segments and geo-objects (i.e., PCG). In addition, while performing this assessment, it was requested to evaluate the segmentation quality by considering the segment file produced for each scale parameter, the ground truth data (in this case, on-screen digitized reference greenhouses), and the satellite image of the relevant segment data. After the visual evaluation of the segmentations, segmentation evaluation metrics were calculated for each segmentation output, and the results were compared with the visual evaluation to determine the best segmentation quality metric for the PCG segmentation.

The second step was designed to assess the effects of several factors (reflectance storage scale (RSS), spatial resolution, shape parameter, study area, and image season) on PCG segmentation. The parameters' influence and interactions were elaborated through a full factorial analysis of variance (ANOVA) design and by computing the partial $\eta^{2,}$ which represents the explained variance of the dependent variable. This parameter partially removes the effects of other factors and interactions.

3.3.2 Multi-resolution segmentation algorithm

MRS is a bottom-up region-merging method in which smaller objects (i.e., pixels) are merged to create large objects with several iterative steps (Baatz & Schäpe, 2000; Benz et al., 2004). Three components regulate the MRS outcome: shape, scale parameter, and compactness. The scale parameter is defined as the maximum heterogeneity for the segment, while compactness is the weight of the smoothness criteria. The last parameter, shape, regulates the weight of color and shape criteria (Tian & Chen, 2007). Besides these parameters, the band combination and the weights of each band should be determined for the MRS algorithm. The MRS algorithm was used through the eCognition v.10.1 software in the thesis.

Theoretically, during the merging process, the weighted heterogeneity of the image objects is minimized by the optimization procedure, and adjacent image objects are combined in this way. The increment of the heterogeneity, f (equation 3.1), is defined with the color and shape, where w_{color} and w_{shape} provide the adaptation of the heterogeneity (Benz et al., 2004).

$$f = w_{color} \times \Delta h_{color} + w_{shape} \times \Delta h_{shape}, \in [0,1,],$$
$$w_{shape} \in [0,1,], w_{color} + w_{shape} = 1 \tag{3.1}$$

Δh_{color}, which is the differences in spectral heterogeneity, provides the muli-variant segmentation by employing the weight of the image channels, w_c (equation 3.2) (Benz et al., 2004).

$$\Delta h_{color} = \sum\nolimits_{c} w_c \times (n_{merge} \times \sigma_{c_{merge}} - (n_{obj1} \times \sigma_{c_{obj1}} + n_{obj2} \times \sigma_{c_{obj2}}) \tag{3.2}$$

where, n is the total number of pixels, σ is the standard deviation within the object, subscripts c refers to the channel, obj1, and obj2 refer to the objects to be merged and merge refers to the merged object.

The shape heterogeneity, Δh_{shape} (equation 3.3), is described with compactness (equation 3.4) and smoothness (equation 3.5) of the object's shape and refers to the improvement of the shape.

$$\Delta h_{shape} = w_{comp} \times \Delta h_{comp} + w_{smooth} \times \Delta h_{smooth},$$
$$w_{comp} + w_{smooth} = 1 \tag{3.3}$$

$$\Delta h_{comp} = n_{merge} \frac{l_{merge}}{\sqrt{b_{merge}}} - \left(n_{obj1} \frac{l_{obj1}}{\sqrt{b_{obj1}}} + n_{obj2} \frac{l_{obj2}}{\sqrt{b_{obj2}}} \right) \tag{3.4}$$

$$\Delta h_{smooth} = n_{merge} \frac{l_{merge}}{b_{merge}} - \left(n_{obj1} \frac{l_{obj1}}{b_{obj1}} + n_{obj2} \frac{l_{obj2}}{b_{obj2}} \right) \tag{3.5}$$

where l is the object perimeter and b is the bounding box perimeter of the object. The merging process stops if the smallest growth described by f is greater than the limit set by the scale parameter.

3.3.3 Segmentation quality evaluation metrics

Several empirical techniques, both supervised and unsupervised, have been proposed to assess the accuracy of image segmentation (Zhang et al., 2008; Zhang, 1996). The basis of the supervised evaluation methods relies on the difference between a set of reference polygons and algorithmically produced image segments (Clinton et al., 2010). Conversely, unsupervised methods assess the segmentation quality by examining the intra-class homogeneity and inter-class heterogeneity (Jozdani & Chen, 2020; Zhang et al., 2008). It has been reported that the supervised evaluation methods are more suitable for the artificial target recognition task since they consider geometric boundaries' accuracy (Chen et al., 2018b). In light of this, supervised assessment techniques can be effectively utilized to select the best segmentation algorithm or to determine the most suitable segmentation parameter for a specific segmentation algorithm (Chen et al., 2018b).

Additionally, factors like plants inside the greenhouse or the seasonal use of greenhouses will influence intra-class homogeneity within a particular greenhouse segment. Further, inter-class heterogeneity may be impacted in regions with a high concentration of greenhouses. These factors may make unsupervised evaluation techniques unsuitable for assessing the accuracy of greenhouse segmentation (Senel et al., 2023).

Supervised evaluation metrics evaluate under-segmentation, over-segmentation, or both by considering reference objects (Aguilar et al., 2018; Costa et al., 2018). Moreover, numerous empirical investigations have concentrated on evaluating the quality of segmentation using supervised assessment measures (Belgiu & Drăguţ, 2014; Clinton et al., 2010; Jozdani & Chen, 2020; Neubert et al., 2008; Tong et al., 2012). Jozdani and Chen (2020) reported that under-segmentation and over-segmentation measures present different deficiencies, such as inappropriate weighting. Therefore, only the combined metrics were considered in the thesis.

Let $X = \{x_i: i = 1,2,\dots,n\}$ represents the n number reference polygon dataset and $Y = \{y_j: i = 1,2,\dots,m\}$ represents the segmentation dataset consisting of m number of polygons based on the notations given by Clinton et al. (2010) and Costa et al. (2018). Moreover, the $area(x_i \cap y_j)$ describes the geographic intersection of the reference object x_i and y_j. The notations used to describe metrics are as follows:

- $\tilde{Y} = \{y_j: area(x_i \cap y_j) \neq 0\}$ is the set of objects (y_j) that intersect reference object x_i,
- $Y_{a_i} = \{y_j: the\ centroid\ of\ x_i\ is\ in\ y_j\}$,
- $Y_{b_i} = \{y_j: the\ centroid\ of\ y_j\ is\ in\ y_j\}$,
- $Y_{c_i} = \{y_j: area(x_i \cap y_j)/area(y_j) > 0.5\}$,
- $Y_{d_i} = \{y_j: area(x_i \cap y_j)/area(x_i) > 0.5\}$,

- $Y_i' = \{y_j: \max(area(x_i \cap y_j))\}$,
- $Y_i^* = \{Y_{a_i} \cup Y_{b_i} \cup Y_{c_i} \cup Y_{d_i}\}$.

Area Fit Index (AFI) (Lucieer and Stein (2002)) is computed as the mean of all AFI_{ij} values given in equation 3.6. AFI equals zero when the overlap ratio between the reference dataset and the segments is 100%, and this means a perfect fit. AFI > 0.0 indicates the image is over-segmented, while AFI < 0.0 is under-segmented.

$$AFI_{ij} = \frac{area(x_i) - area(y_j)}{area(x_i)}, y_j \in Y'_i \tag{3.6}$$

The Quality Rate (QR) is proposed by Weidner (2008) (equation 3.7). This metric takes values between zero to 1, which ideally results in zero.

$$QR_{ij} = 1 - \frac{area(x_i \cap y_j)}{area(x_i \cup y_j)}, y_j \in Y_i^* \tag{3.7}$$

Index D (D-index) is presented as the “closeness” to an ideal segmentation output by Clinton et al. (2010). This metric (equation 3.8) is initially proposed by Levine and Nazif (1982), and it ranges from 0 to 1 in, ideally equal to zero.

$$\begin{aligned} D_{ij} &= \sqrt{\frac{OS_{ij}^2 + US_{ij}^2}{2}}, \text{ where} \\ OS_{ij} &= 1 - \frac{area(x_i \cap y_j)}{area(x_i)}, \\ US_{ij} &= 1 - \frac{area(x_i \cap y_j)}{area(y_j)}, y_j \in Y_i' \end{aligned} \tag{3.8}$$

Match (M), introduced by Janssen and Molenaar (1995) (equation 3.9), and has values ranging from 0 to 1. When M is equal to 1, it means that the reference dataset and segmentation have a perfect match

$$M_{ij} = \sqrt{\frac{area(x_i \cap y_j)^2}{area(x_i) \times area(y_j)}}, y_j \in Y'_i \tag{3.9}$$

Fitness Function (F) (equation 3.10) was proposed by Costa et al. (2008) to quantify both over-segmentation and under-segmentation. Larger values indicate over-segmentation or under-segmentation, while zero indicates a perfect match.

$$F_{ij} = \frac{area(y_j) + area(x_i) - 2 \times area(y_j \cap x_i)}{area(y_j)}, x_i \in X'_j \tag{3.10}$$

F measure is constructed by Zhang et al. (2015) by employing precision and recall metrics (equation 3.11). The recall measure is determined by comparing segments to each reference object, while the precision is calculated by comparing reference polygons to their corresponding segments. Weight argument (α) is employed by this metric which is tales as 0.5 in this thesis. The optimal scenario for the F measure is that it is equal to 1.

$$F - measure = \frac{1}{\frac{\alpha}{Precision} + (1-\alpha)\frac{1}{Recall}}, \ where$$
$$Precision_{ij} = \frac{area(x_i \cap y_j)}{area(y_j)}, x_i \in X'_j, \tag{3.11}$$
$$Recall_{ij} = \frac{area(x_i \cap y_j)}{area(x_i)}, y_j \in Y'_i$$

If a reference polygon's and a candidate segment's intersection area is larger than 50% of either polygon's or candidate segment's total area, a candidate segment can therefore be described as a corresponding segment known as the areal-overlap-based criterion (Clinton et al., 2010; Liu et al., 2012). Liu et al. (2012) proposed the Euclidean Distance 2 (ED2), relying on areal-overlap-based criteria, which evaluate geometric discrepancy and arithmetic discrepancy criteria.

The ED2 measure computes the segmentation quality in two-dimensional Euclidean space with the Potential Segmentation Error (PSE) and Number-of-Segments Ratio (NSR). However, Jozdani and Chen (2020) reported that ED2 does not always correctly determine optimal segmentation results. To tackle the problem, Yang et al. (2014) proposed OverSegmentation 2 (OS2), UnderSegmentation 2 (US2), and Euclidean Distance 3 (ED3) segmentation evaluation metrics. ED3 integrates both geometric and arithmetic discrepancies (equation 3.12). While the range of this metric changes between 0 and 1, the perfect match equals zero.

$$ED3_{ij} = \sqrt{\frac{(OS2_{ij})^2 + (US2_{ij})^2}{2}}, \text{ where}$$
$$OS2_{ij} = 1 - \frac{area(x_i \cap y_j)}{area(x_i)}, \tag{3.12}$$
$$US2_{ij} = 1 - \frac{area(x_i \cap y_j)}{area(y_j)}, y_j \in Y_{c_i} \cup Y_{d_i}$$

When the number of reference polygons increases, reference polygons without corresponding segments can be formed since the rule of at least a 50% overlap ratio is not met. In this case, the number of used reference polygons will be lower than the original number. Therefore, to avoid bias when calculating both PSE and NSR, Novelli et al. (2016) proposed PSE_{new} and NSR_{new} by modifying the ED2 measure.

As given in the formula of modified ED2 (MED2) in equation 3.1, n is the excluded reference polygon number, $\max(|s_i - r_k|)$ is the maximum segment for a single reference polygon and v_{max} is the maximum number of corresponding segments that in one single reference geometry. A MED2 equal to zero when the reference dataset and the segmentation have a perfect match, while a higher MED2 value demonstrates arithmetic and/or geometric discrepancy.

$$ED2 = \sqrt{{PSE_{new}}^2 + {NSR_{new}}^2}, \text{ where}$$
$$PSE_{new} = \frac{\sum|s_i - r_k| + n \times \max(|s_i - r_k|)}{\sum|r_k|} \tag{3.13}$$
$$NSR_{new} = \frac{|m - v - n \times v_{max}|}{m - n}$$

In the thesis, the MED2 metric was calculated through the free access command-line tool (AssesSeg) developed by Novelli et al. (2017). AFI, QR, D-index, M, Fitness, ED3, and F-measure were computed using segmetric library (URL-1), which is available through the R programming language. For the calculation of the metrics, 200 reference polygons were used since this number of polygons was suggested by Aguilar et al. (2018).

3.4 Feature Extraction and Evaluation of the Feature Importance

As the second step of OBIA, features are extracted from each image segment after image segmentation. The features mentioned here can be spectral, textural, geometric, and contextual, or they can be different information obtained from the image (such as spectral indices). Each feature is used as an explanatory variable to train the classification model (Kucharczyk et al., 2020). All features can be used for the classification algorithm, and a subset of the most useful features can be specified and used to classify the image by feature space (Chen et al., 2018a). It has been stated that reducing the number of features will decrease the model complexity since most features tend to be correlated (Chen et al., 2018a; Kucharczyk et al., 2020). Increasing feature diversity in OBIA made the subjective selection of features difficult.

Several techniques have been applied to efficiently reduce the feature space from statistical analysis to machine learning and deep learning. Many of these techniques are proposed to maximize separation distances between classes and minimize the number of input features (Chen et al., 2018a). Machine-learning algorithms such as RF are favorable since they do not assume a specific data distribution. However, as Chen et al. (2018a) stated, there is no consensus on which machine learning algorithm is better than the others for spesific applications. The authors also reported that the use of machine learning algorithms depends on the following parameters; performance, ease of use, and accessibility. Ma et al. (2017a) assessed the efficiency of advanced feature selection methods through SVM and RF classifiers. The authors argued that feature space reduction has great importance on accuracy for both classifiers used. In the thesis, on the emphasis of greenhouse detection, different properties (spectral, textural, geometric, and spectral indices) were extracted from segments, and then feature space reduction methods were performed.

3.4.1 Features extracted

To evaluate the impacts of different spectral features on PCG segmentation, different features given in Table 3.1. were computed. For this purpose, spectral features (including mean, minimum, maximum, and standard deviation of all bands and brightness and difference), textural features (including angular second moment, contrast, correlation, dissimilarity, entropy, homogeneity, standard deviation, and mean calculated in all direction), and spectral indices. Considering the spectral features, all of the bands of Sentinel-2 images were employed in this stage. The bands which have a spatial resolution of 20 m and 60 m were resampled to 10 m.

In Table 3.1, ρ_i presents the reflectance value of the band i, while λ is the wavelength in μm. To investigate the impacts of spectral indices, Normalized Difference Vegetation Index (NDVI) (Rouse et al., 1973), Normalized Difference Builtup Index (NDBI) (Zha et al., 2003), Plastic-Mulched Landcover Index (PMLI) (Lu et al., 2014), Index Greenhouse Vegetable Land Extraction (VI) (Zhao et al., 2004), Plastic Greenhouse Index (PGI) (Yang et al., 2017), Retrogressive Plastic Greenhouse Index (RPGI) (Yang et al., 2017), Plastic GreenHouse Index (PGHI) (Ji et al., 2019), Color Steel Buildings Index (CSBI) (Ji et al., 2019), Moment Distance Index (MDI) (Salas & Henebry, 2012), Greenhouse Detection Index (GDI) (González-Yebra et al., 2018) and Advanced Plastic Greenhouse Index (APGI) (Zhang et al., 2022) were employed in the thesis. These indices were mainly selected based on the literature research on PCG mapping and the formulations of the indices were given in Table 3.1. It should be noted that MDI was computed using the blue, green, red, NIR8, SWIR1, and SWIR2 bands of Sentinel-2.

For the feature extraction stage, 65 spectral feature, six textural features, two geometric information and 55 spectral index features (11 spectral indices with five statistics), in total 128 features were evaluated.

Table 3.1 : Extracted features for the image segments.

	Feature	Description or formula
Spectral information	Mean	Mean values of bands for each image object
	Minimum	Minimum values of bands for each image object
	Maximum	Maximum values of bands for each image object
	Median	Median values of bands for each image objects
	Standard Deviation	The standard deviation of bands for each image object
	Brightness	The brightness of the image layers
	Difference	The maximum difference in brightness
Geometric information	Shape index	The smoothness of an image object border (eCognition Developer 9.0 Reference Book, 2014)
	Width pixel	Width of the object in pixel unit (eCognition Developer 9.0 Reference Book, 2014)
Textural information	GLCM ASM	The angular second moment of all directions
	GLCM CON	The contrast of all directions
	GLCM COR	Correlation of all directions
	GLCM DIS	Dissimilarity of all directions
	GLCM ENT	The entropy of all directions
	GLCM HOM	Homogeneity of all directions
Spectral indices	Normalized Difference Vegetation Index (NDVI)	$NDVI = \frac{NIR - Red}{NIR + Red}$
	Normalized Difference Builtup Index (NDBI)	$NDBI = \frac{SWIR1 - NIR}{SWIR1 + NIR}$

3.1 (continued) : Extracted features for the image segments.

Feature	Description or formula
Plastic-Mulched Landcover Index (PMLI)	$PMLI = \frac{SWIR1 - Red}{SWIR1 + Red}$
Index Greenhouse Vegetable Land Extraction (Vi)	$Vi = \left(\frac{SWIR1 - NIR}{SWIR1 + NIR}\right) \times \left(\frac{NIR - R}{NIR + R}\right)$
Plastic Greenhouse Index (PGI)	$PGI = 100 \times \left(\frac{B \times (NIR - R)}{1 - \frac{B+G+NIR}{3}}\right)$, PGI = 0 where NDVI > 0.73; PGI = 0 when NDBI > 0.005
Retrogressive Plastic Greenhouse Index (RPGI)	$RPGI = 100 \times \left(\frac{B}{1 - \frac{B + G + NIR}{3}}\right)$
Plastic GreenHouse Index (PGHI)	$PGHI = \frac{B}{SWIR2}$
Color Steel Buildings Index (CSBI)	$CSBI = \frac{SWIR2}{SWIR1}$
Moment Distance Index (MDI)	$MDI = MD_{rp} - MD_{lp}$ *where;* $MD_{rp} = \sum_{i=\lambda_{rp}}^{\lambda_{lp}} \sqrt{(\rho_i^2 + (\lambda_{rp} - i)^2)}$, $MD_{lp} = \sum_{i=\lambda_{lp}}^{\lambda_{rp}} \sqrt{(\rho_i^2 + (i - \lambda_{lp})^2)}$,
Greenhouse Detection Index (GDI)	$GDI = \frac{MDI}{3} - \left(\frac{\rho_{blue - \left(\frac{\rho_{SWIR1} + \rho_{SWIR2}}{2}\right)}}{\rho_{blue + \left(\frac{\rho_{SWIR1} + \rho_{SWIR2}}{2}\right)}}\right)$
Advanced Plastic Greenhouse Index (APGI)	$APGI = 100 \times Coastal \times Red \times \frac{2 \times NIR - Red - SWIR2}{2 \times NIR + Red + SWIR2}$

3.4.2 Feature evaluation methods

Reducing the number of features will decrease the model redundancy since most features tend to be correlated. Moreover, increasing feature diversity in OBIA made the subjective selection of features difficult. For that reasons, several methods were implemented for the extracted features, including RF-RFE, Chi^2 test and RF. The effect of feature importance evaluation methods in the scikit-learn library, available through the python programming language, were examined on the accuracy of PCG classification.

3.4.2.1 Chi^2 feature evaluation

The Chi^2 method was used to evaluate the value of a feature by calculating the chi-square stats between each non-negative feature and class and to obtain a ranking list of all features in the feature selection step (Ma et al., 2017a; URL-2). The Chi^2 score of a feature is calculated by considering equation 3.14.

$$\chi^2 = \sum_{i=1}^{r}\sum_{j=1}^{c}\frac{(n_{ij}-\mu_{ij})^2}{\mu_{ij}} \tag{3.14}$$

where c is the class number, and r is the discrete intervals number for the feature.

3.4.2.2 Recursive feature evaluation (RFE)

The purpose of RFE is to choose features taking into account smaller and smaller sets of features by recursively with the external estimator, which assigns the weights for the features. In RFE, in the beginning, the importance of each feature is obtained by training the estimator on the initial features set. The least crucial features are then eliminated from the features. This process is recursively done over the feature set until the selected features are attained (URL-3). In the thesis, two different methods, RF, and SVM with linear kernel, were tested as external estimators for the weights of the features.

3.4.2.3 RF feature evaluation

The RF algorithm proposed by Breiman (2001) can be used to estimate feature importance for ranking the features by calculating predictive importance. The calculation of the predictive power is mainly based on the computation of the mean decrease in the classification accuracy for the out-of-bag (OOB) samples not used in model building from the bootstrap sampling (Ma et al., 2017a). Feature selection using RF is categorized as an embedded method and combines filtering and wrapping approaches.

3.5 Image Classification

The third step of OBIA is the classification model, which is routinely trained to classify the image objects. For example, Kucharczyk et al. (2020) evaluated this section under three subsections: sampling design, response design, and classification.

The sampling design includes generating training data and testing sample locations. It is pointed out that the ideal test set is expected to comprise as many high-quality samples as possible, with an equal number of samples per class.

Response design is labeling the training and testing samples produced or collected in the sampling design stage. Reference data for labeling samples can be collected in the field campaign from pre-existing thematic maps or the interpretation of high-resolution remote sensing images (Kucharczyk et al., 2020).

The last subsection is classification, training a model, and classifying image objects. There are several approaches for classification, including rule-based or supervised approaches. Ma et al. (2017b) reported that supervised object-based classification techniques have been an indispensable part of remote sensing research on land cover mapping since 2010. Recently, besides the traditional machine learning algorithms such as RF, SVM, or KNN, new generation ensemble learning algorithms are increasingly used within the OBIA. Thus, several methods, including KNN, SVM, adaptive boosting (AdaBoost), RF, GB, XGBoost, CatBoost, and LightGBM, have been tested for greenhouse mapping in the thesis.

3.5.1 K-nearest neighbor (KNN)

KNN is a neighbors-based classification algorithm, which is categorized as instance-based or non-generalizing learning. This method only keeps instances of the training data instead of creating a comprehensive internal model. After classification is computed using a simple majority vote of each point's nearest neighbors, an unknown object is assigned to the most representative data class among its closest neighbors. The outputs of this algorithm are mainly controlled by the k parameter, which is highly dependent on the data. It has been noted that the larger k value reduces the impacts of noise but also blurs the classification boundaries (URL-4).

3.5.2 Support vector machines (SVM)

SVM is one of the most commonly used kernel-based statistical learning algorithms. SVM is non-parametric, meaning the algorithm is insensitive to the underlying data distribution. The SVM algorithm seeks to identify a hyperplane that splits the dataset into a specified number of classes consistent with the training samples (Vapnik, 2006). Kernel functions can minimize the dimensionality-induced increase in computational complexity (Sheykhmousa et al., 2020). The choice of kernels is the main issue with the applicability of SVMs, affecting the results of the classification process directly. Various types of kernels are employed in the SVMs, including linear, polynomial, radial basis function, and sigmoid kernels (Kavzoglu & Colkesen, 2009). In the thesis, linear and radial basis function, which are commonly employed in remote sensing literature, were tested.

3.5.3 Adaptive boosting (AdaBoost)

Boosting and bagging methods are commonly used in ensemble learning approaches. In boosting, each model tries to eliminate the error of the previous one in each sequence (Sheykhmousa et al., 2020). Adaboost, introduced by Freund and Schapire (1997), was the first boosting algorithm. The idea of AdaBoost is to adjust adaptively of the errors while fitting a sequence of weak hypotheses. The final prediction is then generated using a weighted majority vote by summing their probabilistic predictions (Freund & Schapire, 1997).

3.5.4 Random forest (RF)

The RF algorithm is one of the first successful bagging approaches, which combines the bagging sampling approach, random feature selection, and random decision trees (Sheykhmousa et al., 2020). The RF algorithm is based on the concept of classification and regression trees but relies on several self-learning ensembles of trees called forests. The classification performance of a single tree is enhanced with the bagging approach, which combines the bootstrap aggregating for each tree. In addition, the trees are constructed for the random subset of features at each splitting node, which significantly reduces the over-fitting and helps to reduce the correlation between trees (Breiman, 2001). In this case, overfitting is eliminated with the ultimate prediction for the classification problem (Sheykhmousa et al., 2020).

3.5.5 Gradient boosting machines (GB)

The basic principle of the GB algorithm introduced by Friedman (2001) is to build the new base learners to have the highest possible correlation with the entire ensemble's negative gradient of the loss function. To obtain a more accurate estimation of the response variable, the learning process in GB always fits new models (Lagrari et al., 2019).

3.5.6 Extreme gradient boosting (XGBoost)

XGBoost, developed by Chen and Guestrin (2016), is an increasingly popular method for classification in data science and remote sensing fields thanks to its ability to produce and compress multiple decision trees to improve classification accuracy. In addition, models are resistant to overfitting since the learning process is iterative and additive, combined with a robust regularization framework (Muthoka et al., 2021).

The innovative part of the XGBoost is that it contains an objective function that incorporates the loss function and the regulation term, which regulates the model complexity. It has been stated that the high predictive ability of the XGBoost algorithm is associated with the loss function algorithm and its ability to optimize simultaneous weak learning to improve model performance (Abdi, 2019; Chen & Guestrin, 2016; Muthoka et al., 2021).

3.5.7 Categorical boosting (CatBoost)

CatBoost is a recently popular gradient boosting algorithm introduced by Prokhorenkova et al. (2017) for classification, regression, and ranking tasks. It has been noted that CatBoost provides fast and reliable performance, even with a small dataset, and reduces overfitting. Moreover, in contrast to other machine learning methods, this algorithm can handle a variety of data formats, including categorical characteristics with the minimum amount of training data (Sahin, 2020).

3.5.8 Light gradient boosting machines (LightGBM)

LightGBM, which used the tree-based learning method, provides a gradient boosting by including two new approaches described as Gradient-based One-Side Sampling (GOSS) and Exclusive Feature Bundling (EFB) (Ke et al., 2017). Moreover, since it is based on decision tree algorithms, LightGBM splits the tree optimally by leaf information (Figure 3.3(a)), while other augmentation algorithms like XGBoost split the tree on a depth or level basis (Figure 3.3(b)), not on a leaf basis.

In LightGBM, trees grow with a leaf-wise (or best-first) approach that grows leaves with maximum delta loss to ensure accuracy optimization, unlike other decision tree approaches. Moreover, LightGBM limits the tree depth using several parameters to prevent possible over-fitting with a small dataset. In this case, trees continue to grow as leaves if this parameter is defined (Wang et al., 2020).

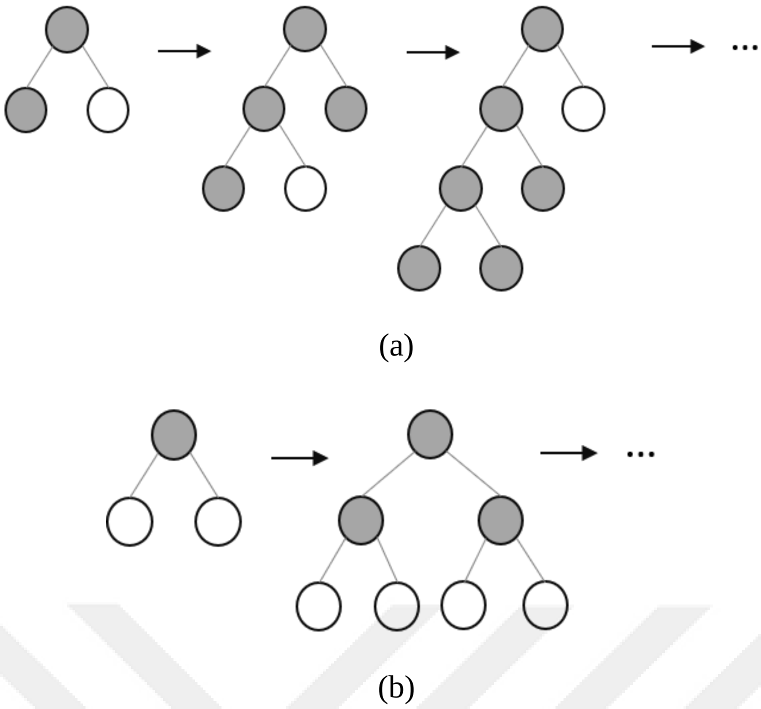

(a)

(b)

Figure 3.3 : (a) Leaf-wise and (b) level-wise growth (adapted from Microsoft Corporation (2021).

3.5.9 Cross-validation and hyperparameter tuning

Within the scope of the thesis, the stratified k-fold method was used to divide the train/test set to evaluate the performance of the models. In this method, the cross-validation process is split into stratified folds n repetitions (see Figure 3.4). Each set in each k-fold contains approximately the same percentage of samples from each class. In this thesis, stratified k-fold was conducted with 10 fold in 3 repetitions. The stratified k-fold was implemented with the scikit-learn library using Python 3.7.

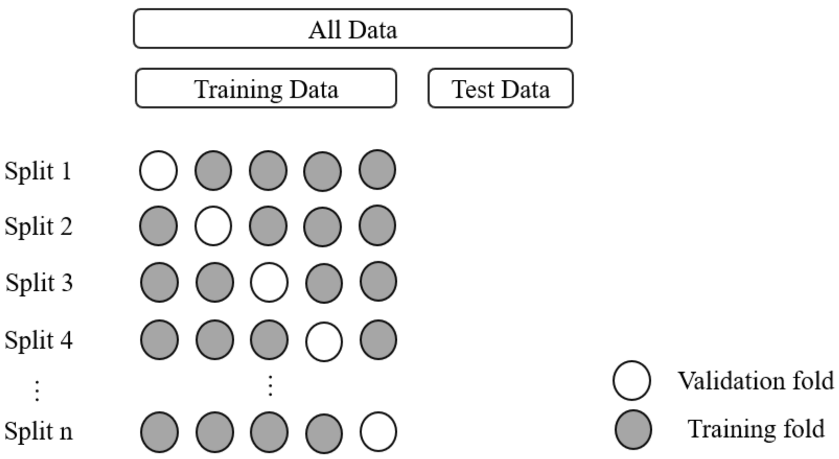

Figure 3.4 : Schema for the stratified k-fold method.

Hyperparameters for the eight algorithms explained in the previous section were selected by utilizing the GridSearchCV function within the scikit-learn library. This function provides the selection of hyperparameters with exhaustive search, which are not learned by the estimator (classification algorithm).

GridSearchCV basically fit the training samples to the algorithms with the specified range of hyperparameters and tested the score with cross-validation. For the cross-validation of the scores for GridSearchCV, the k-fold method was used again.

3.5.10 Accuracy assessment

The accuracy assessment task compares two sources of information, one based on the analysis of remote sensing data (the map) and another based on the reference data assumed to be accurate (Campbell & Wynne, 2011). OBIA accuracy assessment, in which thematic accuracy is evaluated, also compares classified image objects with labeled test samples, i.e., reference class (Kucharczyk et al., 2020). As Campbell and Wynne (2011) described, the standard form for addressing errors is the error matrix (also called confusion matrix), as it establishes overall errors for each category and misclassifications by category.

The error matrix (or confusion matrix) can be utilized as an initial point for various descriptive and analytical statistical techniques (Congalton, 1991). The accuracy of the thematic maps created through OBIA was calculated by creating an error matrix, and the following metrics were calculated. To evaluate the mapping abilities of the investigated methods, an error matrix was constructed for each case, and accuracy assessment metrics, including overall accuracy (OA), producer's accuracy (PA), user's accuracy (UA), and F1-score (F1) were computed. These metrics were calculated as follows;

$$UA = \frac{TP}{(TP + FP)} \tag{3.15}$$

$$PA = \frac{TP}{(TP + FN)} \tag{3.16}$$

$$F1 = 2 \times \frac{(UA \times PA)}{(UA + PA)} \tag{3.17}$$

where TP, FP, TN and FN represent true positive, false positive, true negative and false negative, respectively. TP denotes the total number of correctly classified PCG pixels, while FP represents the total number of incorrectly classified non-PCG pixels as PCG. Furthermore, FN represents the PCG pixels incorrectly identified as non-PCG pixels and FP represents the non-PCG pixels incorrectly identified as PCG pixels. All the metrics take a value between 0 to 1, where a high value represents better classification accuracy. In the thesis, mainly the F1 metric was used to evaluate the accuracy of the PCG mapping ability of the algorithms.

4. EXPERIMENTS AND RESULTS

4.1 Image Segmentation

4.1.1 Evaluation of the segmentation quality metrics

In the first stage, six experienced interpreters visually assessed image segmentation datasets created with the MRS algorithm with variable scale parameters, always keeping the compactness and shape parameters constant at 0.5. It has been stated by Novelli et al. (2016) that the blue, green, NIR combination for Sentinel-2 and the blue, green, NIR2 combination for WorldView-2 images achieved the best segmentation accuracy for greenhouse detection. Thereupon, in this thesis, the segmentation was conducted by using the blue, green and NIR2 bands of Worldview-3 data, while blue, green, and NIR bands of Sentinel-2 and SPOT-7 were used for the segmentation. It should be noted that the weight of the bands was taken equally.

The MRS was conducted for each image corresponding to different study sites (i.e., Almería and Antalya), satellite images (WV3, Sentinel-2, and SPOT-7), seasons (summer and winter), and reflectance storage scales (percent and 16Bit). It should be keep in mind that scale parameters for each segmentation file was hidden from the interpreter. All the segmentation files were named randomly to achieve a fair comparison. Ten segmentation files for 16 image sources created with varying MRS scale parameters were visually evaluated by ranking the segmentations from best (1) to worst (10) based on the scores provided by the six experienced interpreters. After visual evaluation, the median value of the scores given by the six interpreters was calculated for each segmentation file.

Table 4.1 shows an example of the visual evaluation results for the ten segmentations computed from the SPOT-7 image with the percentage reflectance storage scales taken on February 5, 2019 at the Antalya study site. In this case, the MRS scale parameter ranged from 35 to 80. Other tables showing the visual interpretation for other datasets were given in Appendices Table A.1-Table A.8.

Table 4.1 : Example of the visual evaluation of segmentation quality for Antalya study site, winter season, SPOT-7 image, and reflectance storage scales ranging from 0.1 to 100 (percent). SP: MRS scale parameter. I: Interpreter.

SP	Scores granted by interpreters						Median
	I-1	I-2	I-3	I-4	I-5	I-6	
15	6	3	5	5	8	9	5.5
20	4	2	4	3	3	6	3.5
25	1 (best)	1 (best)	3	1 (best)	5	1 (best)	1.0
30	2	4	1 (best)	2	4	2	2.0
35	3	5	2	4	1 (best)	3	3.0
40	5	6	6	7	2	4	5.5
45	7	7	7	6	6	5	6.5
50	8	8	8	8	7	7	8.0
55	9	9	9	9	9	8	9.0
60	10 (worst)	10 (worst)	10 (worst)	10 (worst)	10 (worst)	10 (worst)	10.0

Following the visual interpretation, the eight segmentation quality evaluation metrics (MED2, AFI, D-Index, ED3, F-Measure, Fitness, M and QR) were calculated for the each segmentation file. An example to this process is given in Table 4.2 for the SPOT-7 image with the percentage reflectance storage scales taken on February 5, 2019 at the Antalya study site, while other tables corresponding to the metrics are given in Appendices (Table A.9 - Table A.16).

Table 4.2 : Computed segmentation accuracy metrics and median values of visual rankings for the Antalya study site, winter season, and SPOT-7 Percent orthoimages. Optimal values for the indices were given within the parenthesis.

SP	MED2 (0)	AFI (0)	D index (0)	ED3 (0)	Fmeasure (1)	Fitness (0)	M (1)	QR (0)	Median
15	1.097	0.163	0.433	0.287	**0.516**	8.624	0.829	0.598	5.5
20	0.425	**-0.021**	0.328	0.193	0.490	5.064	**0.866**	0.444	3.5
25	**0.252**	-0.316	0.274	0.148	0.446	3.592	0.852	0.369	**1**
30	0.338	-0.523	**0.272**	**0.146**	0.404	2.862	0.831	**0.366**	2
35	0.561	-0.875	0.297	0.175	0.364	2.186	0.783	0.404	3
40	0.848	-1.297	0.333	0.204	0.329	1.889	0.736	0.453	5.5
45	1.307	-2.149	0.360	0.237	0.292	1.552	0.680	0.500	6.5
50	1.689	-2.936	0.389	0.262	0.270	1.417	0.640	0.543	8
55	2.415	-4.295	0.422	0.293	0.248	1.336	0.589	0.596	9
60	2.802	-4.827	0.448	0.312	0.233	**1.248**	0.559	0.633	10

The median value of the segmentation rankings provided by the six interpreters and the values computed with eight metrics considering the reference polygons were compared to determine the best metrics for each of the sixteen image sources. This comparison was assessed with a scoring system to determine the best metrics for the PCG segmentation. For example, as given in Table 4.2, the lowest median value was found as 1 for scale parameter 25 as a result of visual evaluations, and only MED2 among segment metrics reached the optimal value with this scale parameter. Thus, MED2 was scored as 3 points for this dataset. The following median value of 2 corresponds to optimal values in the D index, ED3, and QR metrics; therefore, these metrics were scored as 2 points. The third-ranking median value 3 did not coincide with any metric, and none of the metrics scored as1 point. This scoring system was evaluated for 16 image sources. Finally, the scores for each metric were summed for all data sets to determine which metrics performed best to catch the best segmentation and worst segmentation (Table 4.3).

Table 4.3 : Total points for metrics in Almería study site for best and worst cases. (WV3: WorldView-3, S2:Sentinel-2)

	Almería December				Almería June				
	Best								Total Points
	WV3 Percent	WV3 16 bits	S2 Percent	S2 16 bits	WV3 Percent	WV3 16 bits	S2 Percent	S2 16 bits	
MED2	3	3	3	3	3		1	3	19
AFI			2	2	1		2		7
D index		2	2	1		2		2	9
ED3	1	2	2	3	2	3		2	15
Fmeasure			1						1
Fitness						2		2	4
M	2		2	3	3		2		12
QR		2	2	1		2		2	9
	Worst								
	WV3 Percent	WV3 16 bits	S2 Percent	S2 16 bits	WV3 Percent	WV3 16 bits	S2 Percent	S2 16 bits	Total Points
MED2	3	3	3	3	3	3	3	3	24
AFI	3		1	1	1				6
D index		3	3	3	3	3	3	3	21
ED3		3	3	3	3	3	3	3	21
Fmeasure	3		1	1	1		3		9
Fitness		3	3	3	3	3	3	3	21
M	3	3	3	3	3	3	3	3	24
QR		3	3	3	3	3	3	3	21

Table 4.4 : Total points for metrics in Antalya study site for best and worst cases. (S7: SPOT-7, S2: Sentinel-2)

	Antalya February				Antalya July				Total Points
	Best								
	S7 Percent	S7 16 bits	S2 Percent	S2 16 bits	S7 Percent	S7 16 bits	S2 Percent	S2 16 bits	
MED2	3	2	3	3	3	3	3	3	23
AFI				2					2
D index	2	3	2	1	2		3		13
ED3	2	1	2	1	2		2		10
Fmeasure									0
Fitness									0
M				2	3				5
QR	2	3	2	1	2		3		13
	Worst								
	S7 Percent	S7 16 bits	S2 Percent	S2 16 bits	S7 Percent	S7 16 bits	S2 Percent	S2 16 bits	Total Points
MED2	3		3	3	3	3	3	3	21
AFI	3		3	1	3	1	3		14
D index	3	3	2	3	1	3	3	3	21
ED3	3	3	2	3	1	3	3	3	21
Fmeasure	3		3	1	3	1	3		14
Fitness		3	2	3	1	3	3	3	18
M	3		3	1	3	1	3		14
QR	3	3	2	3	1	3	3	3	21

The result of Table 4.3 and Table 4.4 revealed that the metric with the highest score was MED2 in both study sites, with 42 points. Following that, ED3 reached the highest score, with 25 points. Finally, QR and D index metrics got 22 points. Similarly, the ability to determine the worst segmentations of the metrics was assessed by the same scoring system. In the worst segmentation determination case, MED2 reached 45 points, ED3, D-index, and QR reached 42 points, and Fitness achieved 39 points. It can be pointed out that the MED2 metric is more successful in determining the optimal scale parameter among the investigated metrics.

4.1.1.1 Statistical analysis of the visual rankings

The effects of the investigated factors, including study site, seasons, spatial resolution, and RSS, and their two-way interactions on the variation of the median values of the visual rankings, were investigated through a factorial ANOVA.

In this step, only the best 16 segmentations corresponding to the best median value were analyzed with ANOVA. The Kolmogorov-Smirnov test was conducted to test the normal distribution, and $p < 0.05$ were considered for statistical significance. The results of the Kolmogorov-Smirnov test revealed that the population of the median values as a dependent variable fit a normal distribution. The adjusted Pearson correlation coefficient (R^2) explained by the ANOVA model was 0.768 and statistically significant (p= 0.000). The ANOVA results of the investigated factors are given in Table 4.5.

Table 4.5 : ANOVA results of the visual rankings.

Factors and their interactions	p-value
Study site	0.65
Spatial resolution	0.06
RSS	0.00
Season	0.06
RSS x Season	0.65
Spatial resolution x RSS	0.01
Study site x RSS	0.20
Spatial resolution x Season	0.65
Study site x Season	0.20
Study site x Spatial resolution	0.65

As given in Table 4.5, the statistical analysis showed that the reflectance storage scale (16Bit and Percent) and the interaction of reflectance storage scale and spatial resolution were highly significant, which means that these two factors are significant in interpreters' ability to appreciate the quality of the segmentation. To elaborate this more in depth, estimated marginal means for the RSS were also calculated. As a result of this, in contrast to the value of 1.563 provided by the Percent format, the mean value of the dependent variable (median) for the 16Bit format took a value of 2.250. Since Percent segmentation results appear less artificial, smoother, and match better with the real world object than the 16Bit outputs, interpreters are more likely to recognize segmentation quality with the Percent outputs. This means that interpreters may therefore feel more comfortable while evaluating the segmentation obtained from Percent images.

To highlight the main difference between the segmentation outputs from these two reflectance storage scale, Figure 4.1 shows a sample area from Almería and Antalya study sites. In this figure, the first and the last column shows the over-segmented and under-segmented scale parameter, respectively, while the second shows the almost optimal scale parameter.

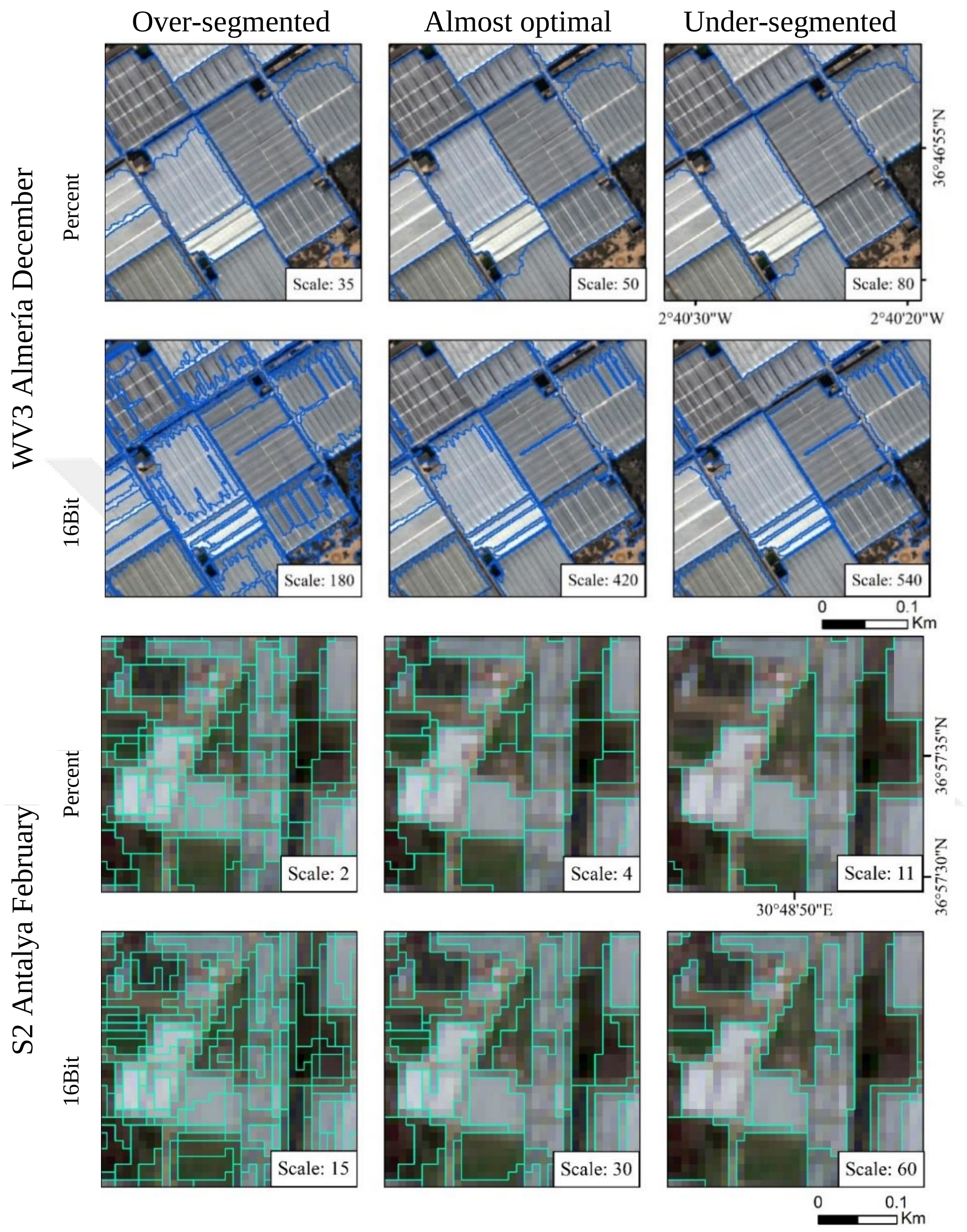

Figure 4.1 : Sample areas from Almería and Antalya showing the segmentation outputs for different scale parameters.

As can be seen in Figure 4.1, there are more noisy and shaky segment edges in segmentation outputs from 16Bit than from Percent. Especially in HR images, the ventilation roofs on the top of the greenhouses cause over-segmentation of the greenhouses. Accordingly, it can be said that this reflectance storage scale related effect had a considerable impact on the interpreter’s ability to perceive visual information.

4.1.2 Evaluating factors affecting segmentation accuracy

Sixteen image sources were tested through the MRS algorithm with various scale parameters (with an increment value of 1) and shape parameters ranging from 0.1 to 0.9 (with an increment value of 0.1). In this process, the compactness parameter was fixed to 0.5. In this way, approximately 4,000 segmentation files were generated through a semi-automated eCognition ruleset.

The segmentation quality was assessed with the MED2 metric since MED2 is the best metric according to the first-stage results. To investigate the segmentation accuracy in depth with different factors, 144 samples regarding the optimal values detected for each shape parameter were taken into account. Figure 4.2 depicts the 144 samples grouped based on the spatial resolution (high spatial resolution (WV3 and SPOT-7) and medium spatial resolution (Sentinel-2)), RSS (Percent and 16Bit), and shape parameters (low shape parameter: 0.1-0.3, medium shape parameter: 0.4-0.6, high shape parameter: 0.7-0.9).

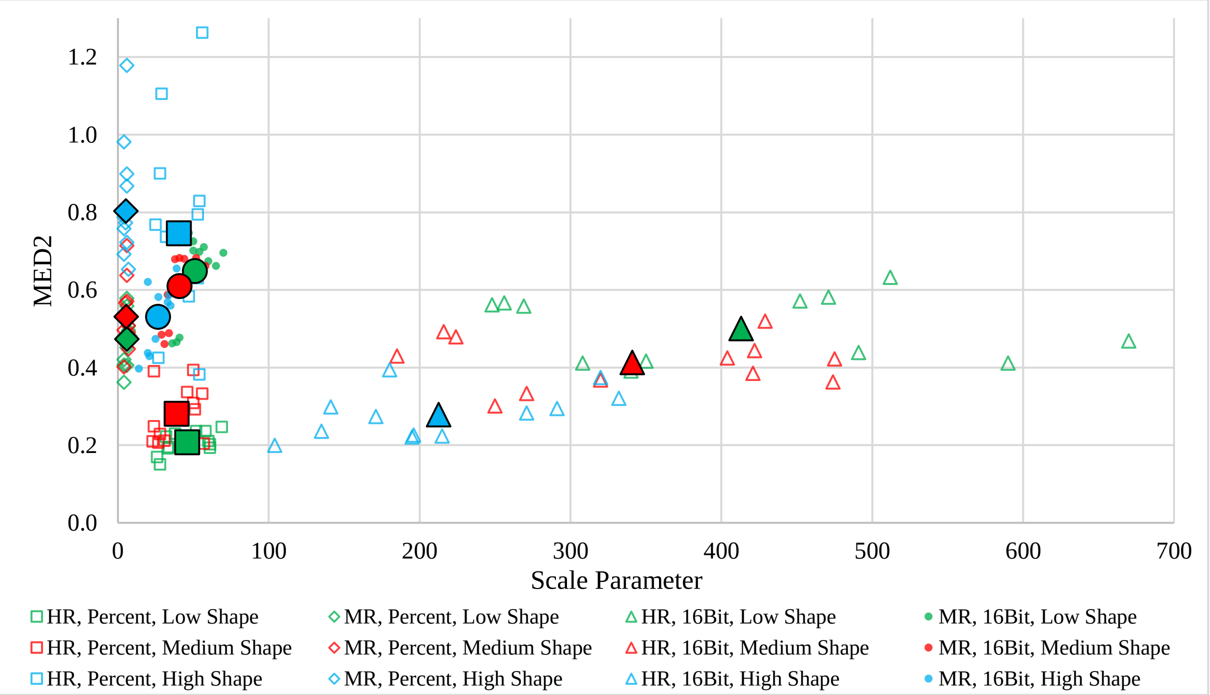

Figure 4.2 : Scale parameter vs MED2 graph showing the results of 144 samples. Note that average values of each reflectance storage scale and shape category are depicted in a solid and larger symbol.

Figure 4.2 revealed that segmentation accuracy decreased with the increasing shape parameter for the percent orthoimages. Additionally, for each category of the shape parameter, the optimal scale parameter was close to one another, resulting in clusters.

The optimal scale parameter distribution for the medium resolution images in Percent format is from 4 to 8, for the 16Bit format is from 14 to 70. Furthermore, for the high-resolution images, the scale parameter distribution is higher in 16Bit format (ranging from 104 to 670) than the Percent format (ranging from 23 to 61). Thus, the dispersion of the scale values are greater, horizontally spread and unstable in 16Bit format than the Percent format in which scale parameters are more clustered.

4.1.2.1 Statistical analysis of the factors

A full factorial ANOVA design was conducted to examine the effect of several factors on segmentation accuracy. The ANOVA model evaluates the relationships between segmentation accuracy (optimal MED2) and some factors (spatial resolution, shape parameter, study area, spatial resolution, RSS, and season and their interactions).

The study site (Antalya and Almería), spatial resolution (high spatial resolution (WV3 and SPOT-7) and medium spatial resolution (Sentinel-2)), season (summer and winter), RSS (Percent and 16Bit) and the shape parameter category (low shape parameter: 0.1-0.3, medium shape parameter: 0.4-0.6, high shape parameter: 0.7-0.9) were the factors analyzed within the ANOVA.

After testing the MED2 values presented a normal distribution, the ANOVA was carried out with 144 samples. The adjusted Pearson correlation coefficient (R^2) explained by the ANOVA model was 0.768, which shows that the variables could explain up to 76.8% of the variance of the optimal MED2 metric and was statistically very significant ($F = 11.096$, $p = 0.000$). This indicates that there are statistically significant differences between the evaluated parameters. Figure 4.3 depicts the scatterplot of observed optimal MED2 against predicted optimal MED2 values based on the computed ANOVA model. Moreover, Figure 4.3 shows that those possible outliers in the ANOVA model are generally from the Percent orthoimages using with highest shape parameters.

Table 4.6 shows the ANOVA results and partial eta-squared statistic (η^2) of the factors and their interactions. Please note that the table is sorted based on the descending partial η^2 values.

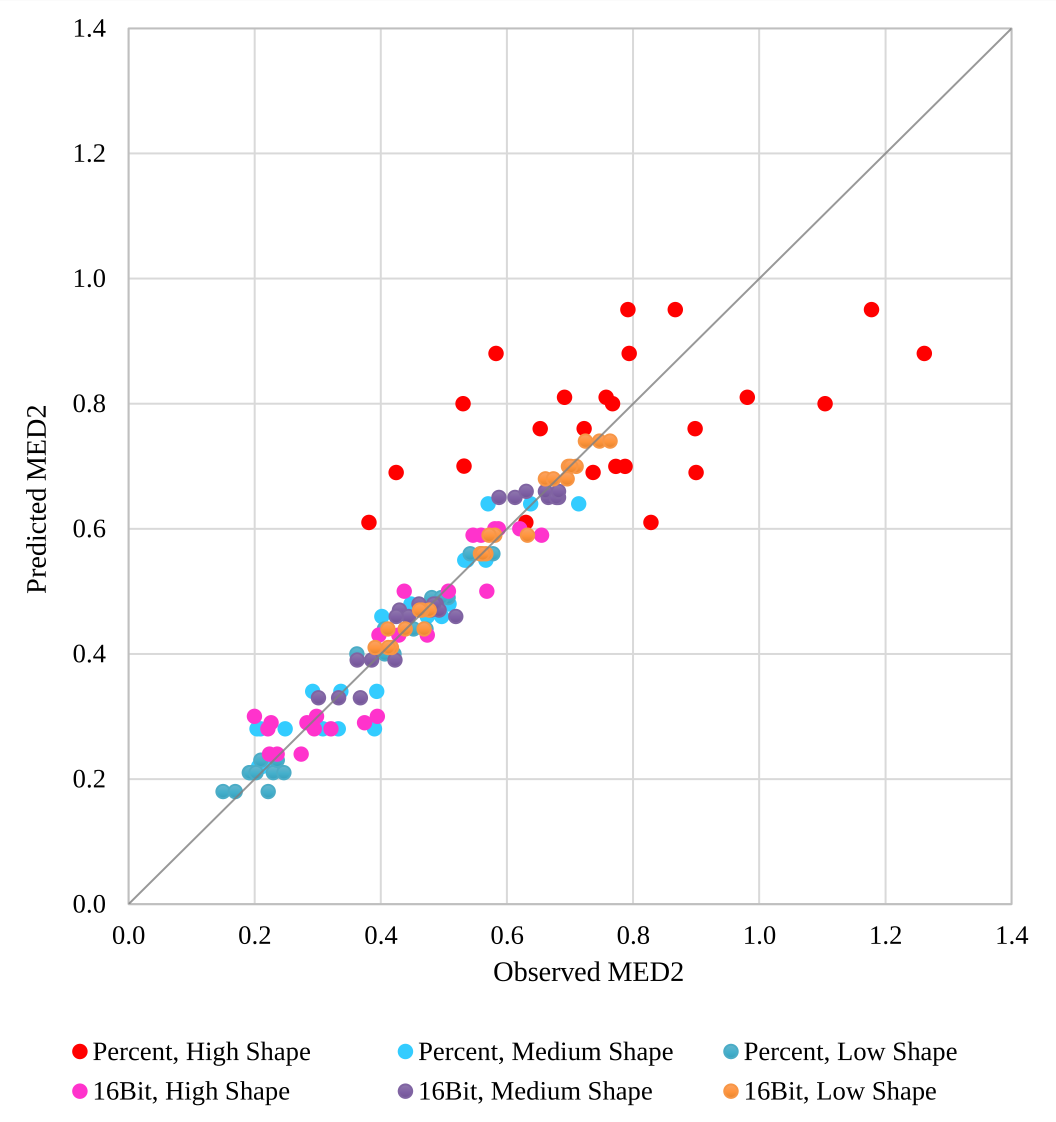

Figure 4.3 : Scatterplot depicting the observed optimal MED2 against predicted optimal MED2 values based on the ANOVA model. Each reflectance storage scale and shape parameter category data are shown in different colors

As seen from Table 4.6, the ANOVA results yielded that the rows starting from the interaction of reflectance storage scale and shape parameter category to the interaction of spatial resolution, season and RSS are statistically significant ($p < 0.05$). The rest of the factors are not statistically significant, and also, there is no statistically significant four-way and five-way interaction among factors.

Besides, the factors and interactions with the highest effect size based on partial η^2 values were the interaction between the factors reflectance storage scale (RSS) and shape parameter category (Shape) (partial $\eta^2 = 0.714$), the spatial resolution factor (partial $\eta^2 = 0.584$) and the shape parameter category factor (partial $\eta^2 = 0.362$).

Table 4.6 : Summary of the ANOVA results (N = 144) indicating factors and interactions together with their associated partial η^2.

Factors and their interactions	p-value	Partial Eta squared (partial η^2)
Intercept	0.000	0.974
RSS x Shape	0.000	0.714
SR	0.000	0.584
Shape	0.000	0.362
SR x RSS x Shape	0.001	0.144
SR x Season	0.00	0.129
Season x RSS x Shape	0.00	0.127
SS	0.01	0.075
SS x Season	0.01	0.068
SS x SR x Season	0.03	0.049
SR x Season x RSS	0.04	0.044
Season x Shape	0.21	0.032
SR x Shape	0.22	0.031
Season x RSS	0.10	0.027
Season	0.11	0.026
SS x SR x Season x Shape	0.38	0.020
SS x SR x RSS x Shape	0.43	0.017
SS x RSS x Shape	0.47	0.016
SS x SR	0.26	0.013
SS x Season x RSS x Shape	0.54	0.013
SS x SR x Season x RSS	0.33	0.010
SR x Season x Shape	0.65	0.009
SS x SR x Season x RSS x Shape	0.70	0.007
RSS	0.56	0.004
SS x SR x RSS	0.57	0.003
SS x Season x Shape	0.86	0.003
SS x Shape	0.86	0.003
SS x Season x RSS	0.68	0.002
SS * RSS	0.70	0.002
SS * SR * Shape	0.93	0.001
SR * Season * RSS * Shape	0.96	0.001
SR * RSS	0.85	0.000

Moreover, the estimated marginal means (EMM) of optimal MED2 as a function of RSS and shape parameter, spatial resolution, and study area were computed to show the reasons for the interaction's considerable impact on segmentation quality (Figure 4.4). Figure 4.4 (a) shows the general trend of the two RSS types (Percent and 16Bit formats) in relation to the shape parameter, which have completely opposing effect on segmentation quality. On one hands, for 16Bit RSS, segmentation accuracy increased as the shape parameter increased. On the other hand, segmentation accuracy continuously fell as the shape parameter decreased for Percent RSS.

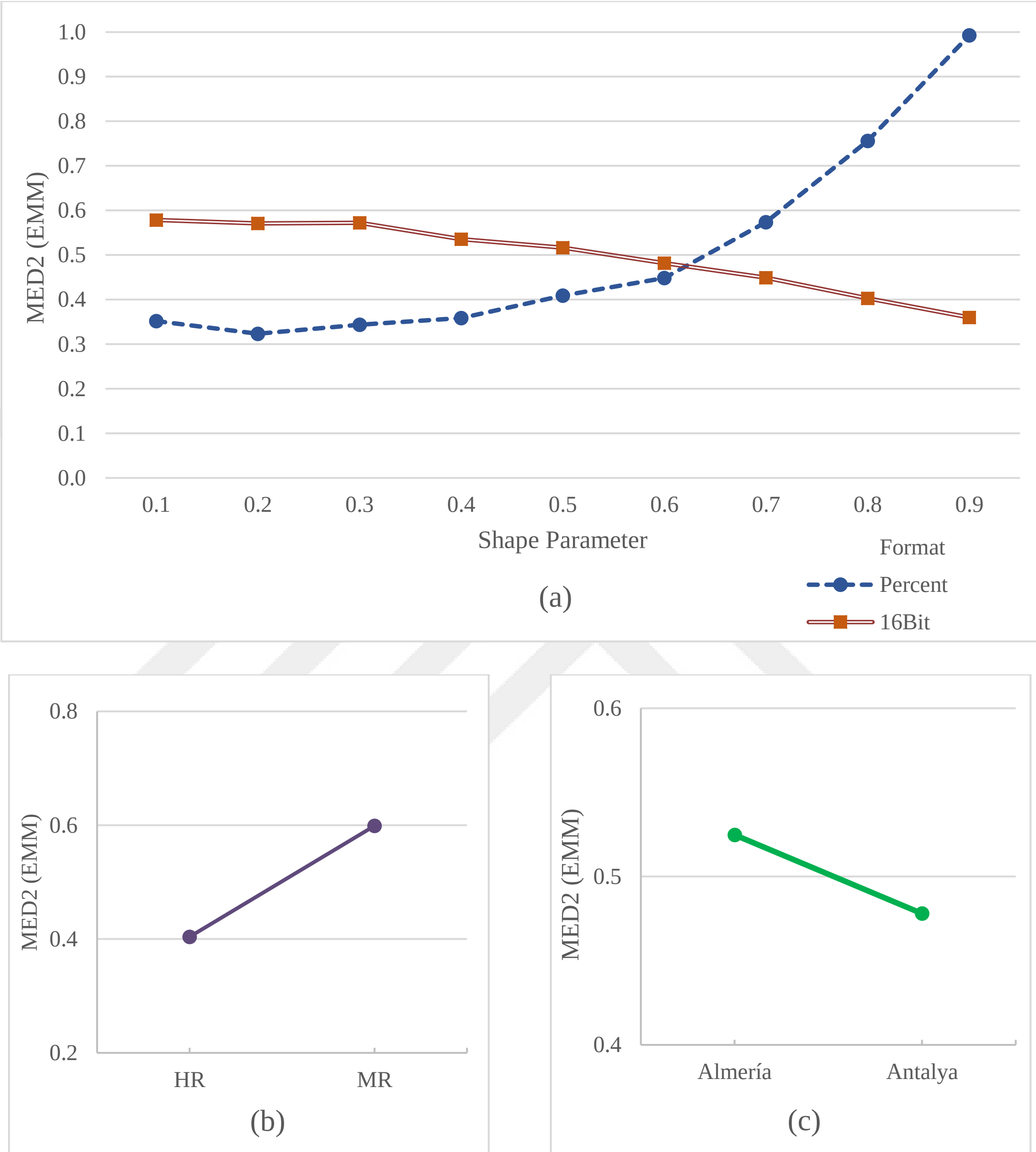

Figure 4.4 : Estimated marginal means (EMM) of optimal MED2 as a function of (a) reflectance storage scale (Percent or 16Bit formats) and shape parameter, (b) spatial resolution (high spatial resolution, HR and medium spatial resolution, MR), and (c) study site (Almería and Antalya).

As confirmed in Figure 4.4 (b), HR images obtained higher segmentation accuracy (with a mean MED2 value of 0.404) than MR images (with a mean MED2 value of 0.599). Moreover, Figure 4.4 (c) revealed that the segmentation accuracy achieved in

Almería (with a mean MED2 value of 0.525)was slightly lower than in Antalya (with a mean MED2 value of 0.478).

Figure 4.4 (b) verified the opposite pattern between Percent and 16Bit RSS formats with varying shape parameters, which lie behind the highest shape parameters appearing as outliers for the Percent format in the scatterplot given in Figure 4.3. These results highlight the critical importance of selecting an acceptable MRS shape parameter based on the RSS format for getting the best segmentation accuracy.

4.2 Feature Extraction and Feature Space Evaluation

After the image segmentation step, segmentation outputs were obtained for Sentinel-2 images based on the results of the first step. The MRS segmentation algorithm was computed by keeping the compactness constant at 0.5, using the B, G, and NIR bands. The parameters and RSS type showing the segmentation step are given in Table 4.7.

Table 4.7 : Segmentation parameters, MED2 values and the total number of objects for the Sentinel-2 images.

	RSS type	Shape	Scale parameter	MED2	Total object number
Almería	Percent	0.2	6	0.405	1756
Antalya	Percent	0.2	4	0.362	3513

Following these steps, the features given in Table 3.1 were extracted for the Almería December Sentinel-2 and Antalya February Sentinel-2 images. 128 features were extracted, including spectral, textural, geometric, and spectral indices. It should be noted that the spectral features (minimum, maximum, mean, median, and standard deviation) of the spectral indices were also extracted. Then, PCG and non-PCG samples were associated with image segments using the spatial join. After forming the explanatory variables with the ground truth data for each image segment, feature space evaluation methods were applied, and then PCG classification accuracy was assessed by training the RF classifier and computing the F1-score. However, before testing the algorithm, it should be noted that hyperparameter tuning was achieved by using GridSearchCV function in Python 3.7 environment. The model evaluation was accomplished using the repeated stratified k-fold with 10 splits and 3 repetitions. The optimal hyperparameters for the RF algorithm selected within the GridSerachCV are given in Table 4.8. The application of Chi^2, RF, RFE with RF estimator (RFE-RF), and SVM estimator with the linear kernel (RFE-SVML) were conducted within the Python 3.7 environment. Table 4.9 shows the top 10 features selected with the evaluated methods.

Table 4.8 : The optimal parameters for the RF algorithm selected within the Gridsearch.

Algorithm	Parameter	Optimal value
RF	max_depth	10
	min_samples_split	2
	num_leaves	10

Table 4.9 : Top 10 ranked features for Sentinel-2 images.

	Almería December				Antalya February			
Feature rank	Chi^2	RF	RFE RF	RFE SVM	Chi^2	RF	RFE RF	RFE SVM
1	GLCM Contrast	PGHI Min	PGHI Min	NDVI Max	GLCM Contrast	PGHI Mean	PGHI Median	CSBI Mean
2	RPGI Min	NDVI Max	NDVI Max	GDI Std	Blue Max	PGHI Median	PGHI Mean	NDVI Mean
3	RPGI Median	GDI Max	GDI Max	PGI Min	Blue Median	PGHI Max	GDI Mean	Max diff.
4	Blue Min	NDBI Max	NDBI Max	Vi Max	Blue Min	GDI Mean	Blue Mean	Vi Mean
5	RPGI Mean	NDVI Std	APGI Min	PGHI Min	Blue Mean	Blue Median	SWIR2 Min	PGHI Mean
6	NIR Min	PGI Min	NDVI Std	NDVI Mean	Green Max	GDI Min	PGHI Max	NDBI Med
7	Green Min	GDI Std	PGI Min	NDVI Min	Green Med	Blue Mean	GLCM Ent	GLCM Entr
8	Blue Median	Vi Max	CSBI Max	APGI Min	Green Min	MDI Mean	SWIR2 Mean	Shape index
9	Blue Mean	APGI Min	Vi Max	PGI Std	Red Max	GDI Med	SWIR2 Med	NDVI Std
10	NIR Median	PGHI Mean	GDI Max	NDVI Std	Red Median	PGHI Min	GDI Med	GDI Mean

Table 4.9 showed that GLCM (contrast) ranked first in Chi^2 method in both study areas. In addition, it is observed that the order of the first four features is the same in RF and RFE methods in Almería. These features are PGHI (min), NDVI (max), GDI (max), and NDBI (max). In addition, in the RFE-SVM method, NDVI (max), GDI (standard deviation), and PGI (min) features are in the top three, while all other features for this method consist of spectral indices. In addition, in the Antalya study area, it has been observed that the first three features for RF and the first two features for RFE-RF consist of the spectral values of the PGHI index. In this study area, CSBI

(mean) for RFE-SVM ranked first, followed by NDVI (mean) and maximum difference.

Figure 4.5 depicts the accuracy change (mean value of F1 scores based on the 10 folds in 3 repetation) with a varying total number of features (from 5 to 70) to train the RF classifier. Accordingly, in the Almería study site, the highest accuracy was achieved with the RFE-SVML method with 20 features (F1 score of 93.19%), while the lowest accuracy was achieved with the Chi^2 method with 5 features.

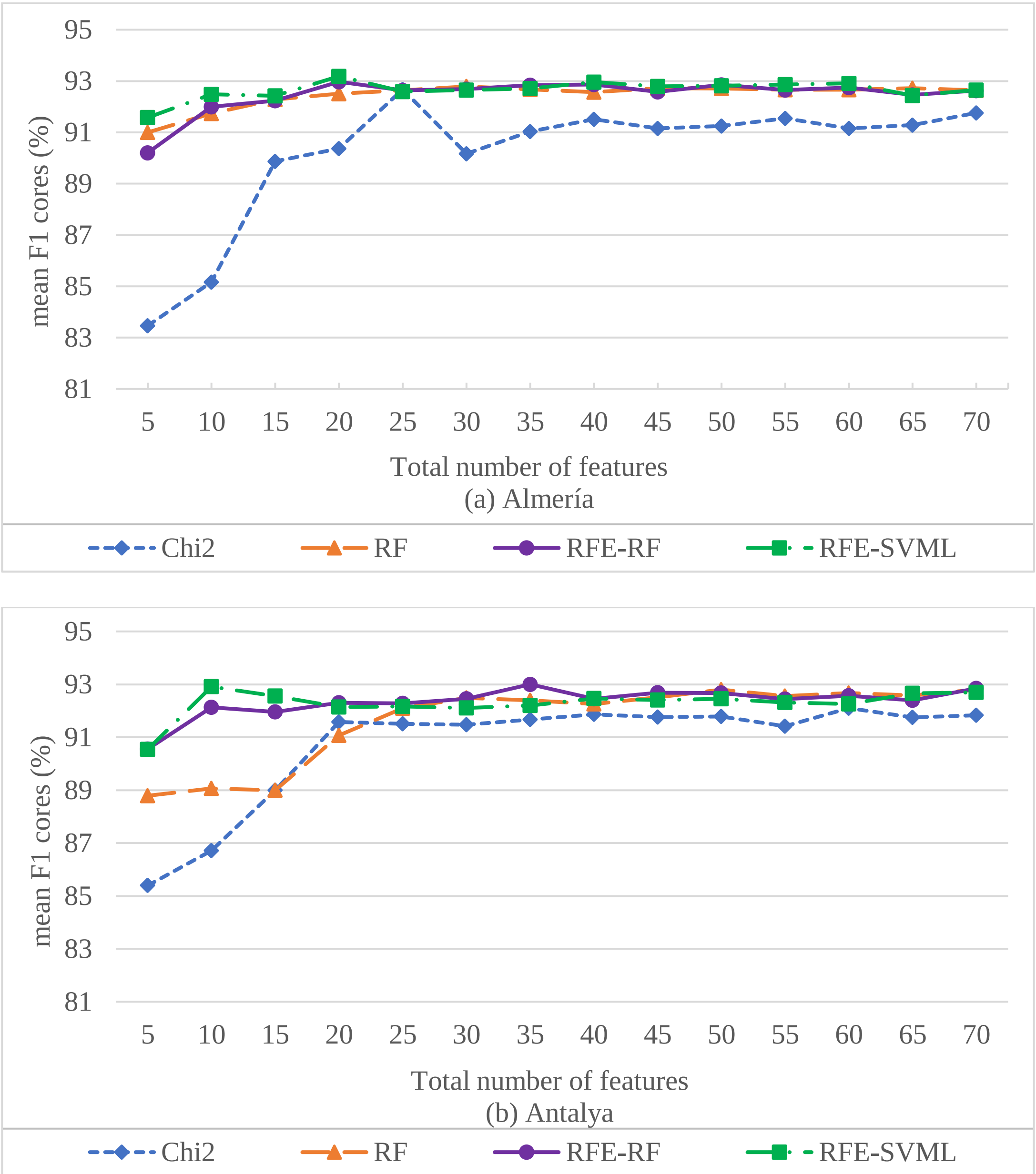

Figure 4.5 : Mean F1 scores of the feature evaluation methods with respect to the changing total number of features for (a) the Almería study site and (b) the Antalya study site.

It has been observed that the Chi^2 method is more sensitive to the changing total number of features, with a standard deviation of F1 score of 2.5 for Almería and 2.04 for Antalya. In the Almería study site, this is followed by RFE-RF (standard deviation = 0.67), RF (standard deviation = 0.48), and RFE-SVM (standard deviation = 0.36), while in the Antalya study site, it is followed by RF (standard deviation = 1.47), RFE-RF (standard deviation = 0.56), and RFE-SVM (standard deviation = 0.53).

The striking pattern in Figure 4.5 is that after the total number of features 35, all the methods tend to achieve stable accuracy. In the Almería study site, the highest accuracy was achieved for Chi^2 with first-ranked 25 features (F1 score of 92.67%), for RF with first-ranked 30 features (F1 score of 92.79%), and for RFE-RF (F1 score of 92.97%) and RFE-SVML (F1 score of 93.19%) with first ranked 20 features. Besides the accuracy, the average time to compile the feature evaluation methods was 1.05 seconds for Chi^2, 1.08 for RF, 37.49 seconds for RFE-RF and 222.76 seconds for RFE-SVML.

In the Antalya study site, the highest accuracy was achieved with the RFE-RF method with a total number of 35 features. This method was followed by RFE-SVML (F1 score of 92.91% with 10 features), RF (F1 score of 92.80% with 50 features), and Chi^2 (F1 score of 92.10% with 60 features), respectively. Additionally, the average time required to run the methods is s 1.55 seconds for Chi^2, 1.78 for RF, 59.75 seconds for RFE-RF and 626.37 seconds for RFE-SVML for Antalya.

4.3 Image Classification

The third and last step of the thesis, image classification and accuracy evaluation was conducted for Sentinel-2 images according to results obtained from the previous sections. The image segments obtained from Section 4.1 and features extracted based on these objects explained in Section 4.2 were used to train the models (KNN, RF, SVM, GB, XGB, LightGBM, AdaBoost, and CatBoost). It should be noted that to train the algorithms, hyperparameters selected through the GridSearchCV were used, which are given in Table 4.10. In addition, for the RF algorithm, the hyperparameters given in Table 4.8 were used. After the training process, image objects were classified, and the accuracy of the models was evaluated by considering the stratified k-fold with 10 splits and 3 repetitions, and F1 scores were calculated for each fold. All the experiments were conducted in a computer with the Intel(R) Core(TM) i7-10750H processor, 16 GB RAM, 2.60 GHz Processor Base Frequency, and Windows 10 Pro (64-Bit) Operating System. The analysis was conducted within Python 3.7 environment.

Table 4.10 : Optimal hyperparameters for the algorithm selected within the Gridsearch.

Algorithm	Parameter	Optimal value
SVM	C	10
	Kernel	Linear
KNN	n_neighbors	5
Adaboost	learning_rate	0.0001
	n_estimators	1
GB	learning_rate	1
	n_estimators	500
XGBoost	colsample_bytree	0.6,
	gamma	1
	subsample	0.6
	max_depth	4
	min_child_weight	5
LightGBM	learning_rate	0.01
	max_depth	3
	min_data_in_leaf	40
	num_leaves	10
Catboost	learning_rate	0.1
	l2_leaf_reg	1
	depth	6

The accuracy results were given in Table 4.10 for both study sites, while the boxplot showing the statistical distribution of the computed F1 scores was given in Figure 4.6. As given in Table 4.11, all the algorithms, except KNN and AdaBoost, achieved over a mean F1 score of 90% considering both study sites. In the Almería study site, the CatBoost algorithm achieved the highest mean F1 score with 92.44%, followed by RF (92.29%), GB (92.08%), XGBoost (92.03%), LightGBM (91.83%), SVM (91.22%), AdaBoost (89.93) and lastly KNN (82.09%). Besides, considering the time required to run the algorithm, the SVM took the longest time, followed by CatBoost and then GB. However, the most crucial issue is that the time required to run the SVM algorithm, which achieves high accuracy, is almost 525 times longer than the time required to run the LightGBM algorithm, which is closest in terms of accuracy. Although the KNN (4.08 second) algorithm is faster than other algorithms, it achieved worse results than all other algorithms in terms of accuracy.

Table 4.11 : Mean F1 score and the total processing time (in second) to compile for each classifier using all 128 features.

	Almería		Antalya	
	Mean F1 score (%)	Time (s)	Mean F1 score (%)	Time (s)
KNN	82.09	4.08	83.29	3.90
RF	92.29	3.36	92.36	5.18
SVM	91.22	2632.09	91.16	4239.05
GB	92.08	76.75	93.19	131.15
XGBoost	92.03	5.01	92.74	7.20
LightGBM	91.83	2.86	91.61	3.44
AdaBoost	89.93	0.28	85.38	0.31
CatBoost	92.44	176.11	92.96	173.84

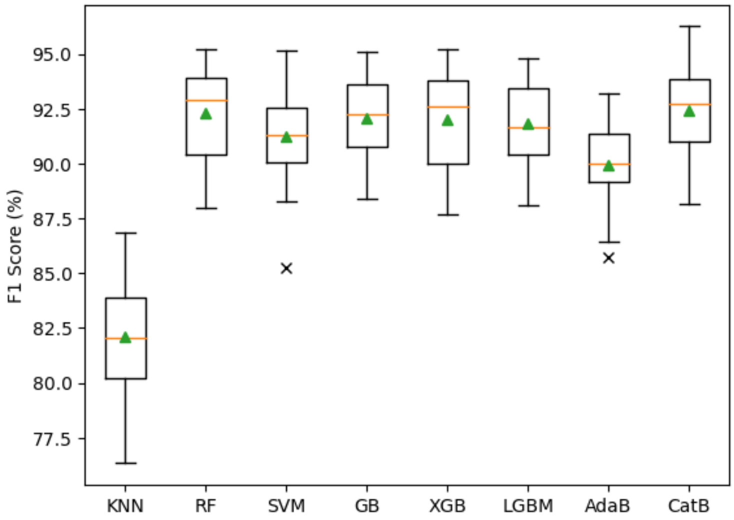

(a) Almería

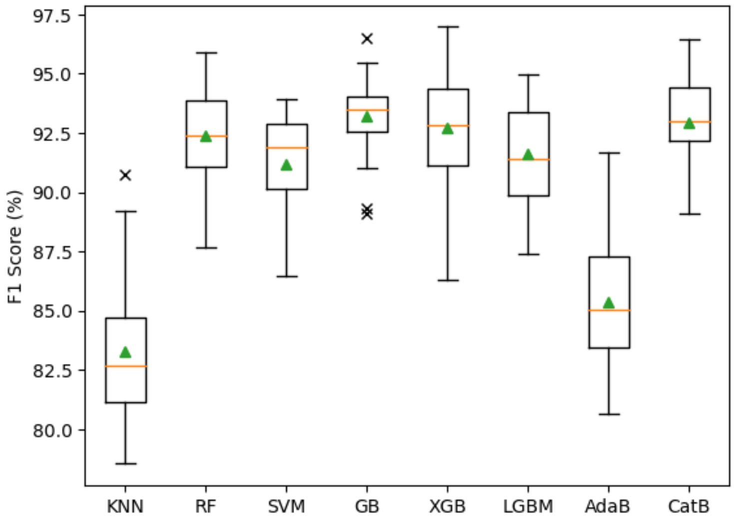

(b) Antalya

Figure 4.6 : The distribution of the F1 scores computed using all 128 features for the investigated classifiers in (a) Almería and (b) Antalya study sites. Note that x specifies the outliers, the orange horizontal line shows the mean and the green triangle shows the median.

One important algorithm that stands out in the Almería study site is the LightGBM algorithm, which reaches 91.83% accuracy in 5.01 seconds. Besides, in the accuracy evaluation performed with 10 folds and 3 repetitions, the KNN algorithm reached the highest standard deviation value (2.76) in F1 score values, as seen in Figure 4.6. XGB followed this algorithm with a standard deviation of 2.19 and SVM with a standard deviation of 2.16. On the other hand, the AdaBoost algorithm reached the lowest standard deviation value, followed by LightGBM and GB.

In the Antalya study site, the highest accuracy was achieved with the GB algorithm (93.19%), followed by CatBoost (92.96%), XGBoost (92.74%), RF (92.36%), LightGBM (91.61%), SVM (91.16%), AdaBoost (85.38%), and KNN (83.29%). Similar to the Almería study area, the SVM was the most time-consuming algorithm which took 4239.05 seconds to run the algorithm, which is also followed by CatBoost (173.84 seconds). In addition, the KNN algorithm reached the highest standard deviation value (3.04), again similar to the Almería study area. This was followed by AdaBoost and XGB. The lowest standard deviation value was 1.59 with GB, followed by SVM with 1.92 and CatBoost with 1.93. In general, in case of accuracy, CatBoost, GB and RF algorithms achieved good PCG classification accuracies. Moreover, Adaboost, LightGBM and RF are the fastest algorithms for PCG classification in the study sites investigated.

The algorithms were also evaluated by considering the 25 features obtained with the RF and RFE-RF algorithms for a detailed analysis of the impacts of feature space evaluation methods on image segmentation algorithms. These feature space evaluation algorithms are applied because they are the fastest algorithm among the investigated methods. The mean F1 score and the time to run the algorithms considering the 25 features were given in Table 4.12 and Table 4.13.

Considering Table 4.12 and Table 4.13, the most important outcome is that the to run the algorithms drastically decreased except for most of the algorithms compared with Table 4.11, which presents the results for all of the features. For example, running the SVM algorithm using all the features took 2632.09 seconds and 4239.05 seconds for Almeria and Antalya study sites, respectively. On the other hand, using only 25 features obtained with RF took 2.32 seconds and 15.95 seconds for Almeria and Antalya study sites, respectively (see Table 4.12).

Table 4.12 : Mean F1 score and the total processing time (in seconds) to compile for each classifier using all 25 features obtained with RF.

	Almería		Antalya	
	Mean F1 score (%)	Time (s)	Mean F1 score (%)	Time (s)
KNN	85.78	0.12	90.08	0.36
RF	92.64	1.64	92.12	3.91
SVM	92.85	2.32	92.07	15.95
GB	91.58	12.68	91.27	26.38
XGBoost	91.64	1.44	91.58	2.36
LightGBM	91.58	0.58	90.55	2.11
AdaBoost	89.93	0.11	85.38	0.13
CatBoost	92.25	34.47	92.09	45.25

Table 4.13 : Mean F1 score and the total processing time (in seconds) to compile for each classifier using all 25 features obtained with RFE-RF.

	Almería		Antalya	
	Mean F1 score (%)	Time (s)	Mean F1 score (%)	Time (s)
KNN	87.04	0.11	90.08	0.22
RF	92.71	1.67	92.25	2.49
SVM	92.69	4.26	92.07	16.41
GB	91.89	13.64	91.22	26.56
XGBoost	92.24	1.60	91.58	2.25
LightGBM	91.88	0.73	90.55	0.78
AdaBoost	89.93	0.11	85.38	0.13
CatBoost	92.57	36.92	92.09	45.45

In case of the Catboost algorithm, the computational cost decreased almost four to five times when using only 25 features. Besides the computational time, for example, for the Almeria study area, decreasing the number of feature space decreased the F1 score with CatBoost, AdaBoost, LightGBM, XGBoost, GB and RF, while the F1 score value increased for the KNN, SVM, and RF algorithms. Regarding accuracy, KNN and AdaBoost algorithms again presented lower accuracies, while other algorithms achieved F1 scores over 90%.

5. DISCUSSION

5.1 Image Segmentation

5.1.1 Image segmentation quality metrics

Employing metrics in selecting optimal MRS parameters for PCG segmentation is important for generalizing segmentation, but which metric to use for this selection is an important question. The answer to this research question was sought in the first stage of the thesis by a comprehensive experimental design with different kinds of image sources. The results given in Section 4.1.1 showed that the MED2 metric was the best metric, while some shortcomings have been identified with other metrics for assessing PCG segmentation quality.

In the almost sixteen datasets examined, the worst segmentation accuracy achieved with the F metric was the highest scale parameter, which means that it depicts the maximum under-segmentation outputs. Conversely, the Fitness metric achieved the best segmentation result with the highest segmentation parameter for all the datasets. In some cases, the worst scale parameter could be determined with the Fitness metric; however, it failed to select the best one, which Jozdani and Chen (2020) also report.

Jozdani and Chen (2020) claimed that the SP selected with the MED2 metric and F measure has resulted in over-segmented objects for building segmentation. Nevertheless, the findings of this research demonstrated that the MED2 metric attained the optimal SP for PCG segmentation. The results yielded that the D index and ED3 were the best metrics to evaluate the PCG segmentation after MED2. The important problem to keep in mind for the metrics D index and ED3 is that the variance of the values pertaining to the SP analyzed is too small. Hence, selecting the best SP with these metrics could be challenging.

5.1.2 Factors Affecting the PCG Segmentation

Within the scope of the thesis, the impacts of different factors on PCG segmentation were evaluated statistically. As a result of this evaluation, the RSS factor emerged as a critical factor.

ANOVA of visual interpretations showed that there is more agreement between interpreters when evaluating Percent orthoimages than 16Bit ones. This is basically related to the fact that the segmentation outputs of these two RSS types are different as already reported by Aguilar et al. (2018), since the ventilation roof windows of PCG were mostly omitted with the Percent RSS type, especially with the WV3 images. These ventilation roofs are unlikely to be seen in the Sentinel-2 orthoimages due to their lower spatial resolution, though over-segmentation can be observed in the optimal SP for Sentinel-2 16Bit image given in Figure 4.1.

Moreover, considering the MED2 metric, the image segmentation quality enhanced with the Percent orthoimages compared to the 16Bit RSS type. The reason behind this can be explained by the main purpose of the segmentation algorithm since the primary purpose is to minimize the heterogeneity between the two objects to be merged. Therefore, as long as there is only a slight increase in heterogeneity, this will result in it merging with another adjacent object.

Considering the MRS algorithm, the spectral heterogeneity (Δh_{color}) given in equation 3.2 is calculated by considering the standard deviation of the two objects. Therefore, downgrading the RSS type from 16Bit format (1-10000) to Percentage format (1-100) will cause a significant decrease in the standard deviation of the objects to be merged, hence the spectral heterogeneity value. The lower standard deviation causes the assembled object to rely on a narrower range of variation. This could explain the lower SP value in Percent images, assuming that objects stop merging when they exceed the threshold f (equation 3.1) value set by SP.

In addition to the RSS factor, it has been seen that choosing the correct value for the shape parameter directly affects the quality of the produced segments. Moreover, its opposite effect on obtaining high-quality segmentation accuracy for images with two types of RSS is demonstrated. In some works (Yao & Wang, 2019, 2022), PCG segmentation quality was investigated in the context of image heterogeneity by using fixed shape and compactness parameters. However, this study revealed the necessity of testing different shape parameters to achieve the best segmentation.

The ANOVA results given in Table 4.6 showed that the spatial resolution of the image is an important factor for PCG segmentation, and moreover, the segmentation results obtained from HR images have higher segmentation accuracy than MR images. In fact, it has been claimed by Mesner and Oštir (2014) that the quality of the image segmentation was reduced with the down-sampling of image spatial resolution. Moreover, Novelli et al. (2016) also reported lower segmentation quality (i.e., higher MED2 values) for the Landsat 8 (30 m GSD) (MED2=0.424) than Sentinel-2 (10 m GSD) (MED2=0.319).

Besides these factors, the optimal MED2 estimated marginal averages for the study area showed that the segmentation accuracy in the Antalya study site was better than the Almería. This may be because PCGs are far from each other and less dense in Antalya, while denser and closer to each other in Almería. Because of this distribution, there are almost no boundaries between PCGs in Almería, so as a result of segmentation, two or more greenhouses appear as the same object, reducing the segmentation accuracy.

5.2 Feature Space Evaluation

5.2.1 Assessment of the feature space evaluation algorithms

The features extracted from each segment play a critical role in the training phase of the classification algorithm as explanatory variables. Within the context of the thesis, four different feature space evaluation algorithms, namely Chi^2, RF, RFE-RF, and RFE-SVML, were assessed both in case of accuracy and time.

In the Almería study area, the algorithm with the highest accuracy was RFE-SVML, while in the Antalya study area, it was RFE-RF. However, the most important difference is that the computational cost of RFE-SVML is almost 6 times higher than RFE-RF in the Almería study area and almost 10 times higher in the Antalya study area.

In fact, Ma et al. (2017) reported that SVM-RFE and Chi^2 are both suitable methods for agriculture mapping with an RF classifier, although the researchers did not evaluate the required time to run the algorithm.

In this thesis, RFE-SVML is also found as suitable in case of accuracy, tough the computational cost for this algorithm is too high. RFE-RF achieved the highest accuracy in the Antalya study area. Moreover, the sensitivity of this method to the variation of feature space number was lower than other algorithms in this study area (with a standard deviation of 0.56). In the Almería study site, both RFE-RF and RF algorithms achieved high PCG mapping accuracy, and they are less sensitive to the change of feature space number than Chi^2. Consequently, RFE-RF and RF algorithms were optimal for the PCG mapping considering both accuracy and computational cost.

5.2.2 The most effective features for the PCG mapping

To evaluate the effects of different features, including spectral, textural, geometric features and spectral indices, a total of 128 features were extracted and assessed through the feature space evaluation methods. The results given in Table 4.9 yielded that among the ten most relevant features, PGHI (min) and NDVI (max) in the Almería study site and PGHI (mean) and PGHI (mean) in Antalya study sites demonstrate good importance for RF and RFE-RF methods.

In the research conducted by Aguilar et al. (2022), the most relevant features for PCG mapping were PGHI (mean), NDVI (difference), and NDVI (std) for the Almería study site and PGHI (max) for the Antalya study site with decision tree classifier. The authors also stated that PGHI (mean) demonstrated good relative importance with the other study sites investigated in the research. Chaofan et al. (2016) investigated the important features for PCG mapping in another research. The authors reported that NDVI is the most relevant feature. Considering the outcomes of the RF, RFE-RF, and RFE-SVM algorithms evaluated, the relevant features achieved in this thesis were in line with the other research. Mainly, statistics derived from PGHI presented great relevance with PCG mapping.

5.3 Image Classification Algorithms

Overall results yielded that all algorithms, except KNN and AdaBoost, reached an F1 score of over 90%. In addition, Catboost, RF, and SVM algorithms performed well in both Almería and Antalya study sites, although the computational time for CatBoost and SVM were higher than other algorithms.

Ding et al. (2021) found that RF classifier performed best for the object-based terrace mapping with the highest F1 score (85.83%) than XGBoost (F1 score of 81.72%) and KNN (F1 score of 77.19%) algorithms. Sahin (2020) evaluated the landslide susceptibility modeling ability of the ensemble learning algorithms and found that CatBoost reached the highest prediction capability, followed by XGBoost, LightGBM and GB. In fact CatBoost algorithm performed well in the case of PCG mapping also, although the computational cost of this algorithm is higher than most of the algorithms. In another research, Bektas Balcik et al. (2020) reported that KNN achieved better overall accuracy than RF and SVM for object-based greenhouse mapping. However, according to the results given within this thesis, KNN algorithm underperformed than all of the other algorithms almost in all of the cases.

It has been observed that after the total number of feature 25 the feature space evaluation algorithms achieved close F1 score values. Ma et al. (2017) reported that 15–25 features produced the best classification with the RF classifier. According to the results achieved within the context of this thesis, 20-30 features achieved the best results for Almería, while in Antalya, the total number of features that achieves the best accuracy varies a lot. In this case, the critical issue is, according to Table 4.11 and Table 4.12, reducing the feature space will significantly reduce the computational cost of the algorithm. Nevertheless, considering the time required for the algorithms to run, RF and LightGBM algorithms provide a significant advantage by working fast with high accuracy, especially in terms of generalizing and evaluating these results on a large-scale PCG mapping.

6. CONCLUSIONS

The area covered by greenhouses is increasing day by day around the world with the increasing population. Since the main covering material for greenhouses is plastic, ecological problems will arise in near future due to the fact that excessive usage of plastic. Together with this fact, greenhouses also contribute to the increase in the use of fertilizers and pesticides. On the other hand, since the economy of many rural regions is supported by greenhouse cultivation, greenhouse activities have an essential role in terms of agricultural production, especially in Mediterranean countries. Additionally, in some areas like Antalya, many greenhouses have been affected by the flashfloods lately. Therefore, determining the spatial distribution of these structures, which have high economic returns but cannot keep up with the adverse conditions brought by climate change, will contribute to developing effective policies and taking necessary precautions in case of disasters. Within the scope of this thesis, answers to different questions were sought by using the OBIA approach, which is stated to give better results in the literature, in order to determine greenhouses.

In the image segmentation step, which is the first step of the OBIA approach, two important questions were sought for PCG segmentation. The first of these questions is which of the supervised metrics is better for evaluating PCG segmentation. Experimental designs yielded that the MED2 was the best metric for evaluating the PCG segmentation quality because this metric agreed mainly with the optimal segmentation outputs evaluated by six interpreters. Additionally, the AssesSeg command-line tool used to calculate this metric is freely available, making it easy to easily access and evaluate segmentation accuracy. On the other hand, Fitness and F metrics failed to identify the best segmentation output compared to other metrics investigated. The effects of different factors on the visual interpretation results of interpreters were also examined. It has been revealed that RSS is an important factor in visual interpretation. In detail, when evaluating the segmentation outputs produced from Percent RSS values, it was seen that the interpreters were more in agreement, and therefore they interpreted this data type more efficiently.

The second question to be answered in the segmentation phase is how factors or interactions affect PCG segmentation. The statistical analysis showed that the optimal SP of the segmentation outputs calculated from the sixteen different data sets were clustered by taking values close to each other in Percent RSS type, while they took values in a broader range in 16Bit RSS type. This shows that it will be easier to determine the optimal SP in the Percent RSS type. In addition, statistical tests showed that the optimal SP obtained from the RSS types was directly dependent on the shape parameter. While segmentation accuracy increases with decreasing shape parameters in Percent RSS type, this is the opposite in 16Bit format. This situation revealed that the selection of shape parameters is significant depending on the RSS type. The main conclusion regarding the image segmentation step is that Percent RSS type is the appropriate data format for PCG segmentation using MRS, and in addition, low shape parameters in Percent format should be preferred.

In the second stage of the thesis, it was hypothesized that different feature space methods and feature space dimensions affect the classification in terms of accuracy and time. Based on this hypothesis, a total of 128 features were obtained from the Sentinel-2 images of the Almeria and Antalya study areas, and the classification performance was evaluated with the RF algorithm by applying different feature space evaluation methods. As a result of this evaluation, it was seen that the reduction of the feature space influenced the accuracy. Nevertheless, it has been found that reducing the feature space significantly reduces the time required to run the classification algorithm. Therefore, the feature space evaluation algorithms examined concluded that RF and RFE-RF algorithms are more suitable for classification accuracy and the time required to run the method. Moreover, it has been found that these algorithms are less dependent on feature space variation in terms of classification accuracy, but reducing the feature space significantly reduces the computation time.

In addition, among the features which are total of 128 features were obtained from segments and including spectral, textural, geometric features and spectral indices PGHI Min, and NDVI (max) in the Almería study site and PGHI (mean), and PGHI (mean) in Antalya study sites found as the most relevant features according to RF and RFE-RF methods. It should be noted that the size and the content of the feature space directly affects the mapping accuracy. As a result, in PCG mapping studies, the application of one of the feature space evaluation methods, such as RF and RFE-RF and including indices such as PGHI and NDVI, is suggested to reduce the computation time and increase the mapping accuracy.

In the third and final stage of the thesis, an answer was sought to the question of which of the ensemble learning algorithms is the best method for PCG classification. Experimental results showed that Catboost, RF and SVM algorithms performed well in both study areas, but the computation time required for CatBoost and SVM was higher than all other algorithms studied. On the other hand, KNN and AdaBoost algorithms reached lower F1 score values in both study areas. In addition to these algorithms, the LightGBM algorithm reached an F1 score of over 90% in both study areas in a very short time. In summary, considering the computation time and classification accuracy, RF and LightGBM are the two prominent algorithms in this study. However, it should be noted that the choice of the classification algorithm depends on the purpose of the application.

In general, within the scope of this thesis, answers were sought for the problems that may occur in three different steps of the OBIA approach to reach the best PCG classification. In terms of PCG determination from satellite images, the analysis was carried out in two essential study areas in the Mediterranean Basin, where greenhouse activities are extensively carried out. The outputs obtained from the classification algorithms also revealed that integrating open access algorithms into the OBIA methodology is suitable. Although these outputs belong to selected test sites, they provide essential outputs for generalizing the findings on a large scale.

REFERENCES

Abdi, A. M. (2019). Land cover and land use classification performance of machine learning algorithms in a boreal landscape using Sentinel-2 data. *GIScience & Remote Sensing*, 57(1), 1-20. doi:10.1080/ 15481603.2019 .1650447

Agüera, F., Aguilar, M. A., & Aguilar, F. J. (2006). Detecting greenhouse changes from QuickBird imagery on the Mediterranean coast. *International Journal of Remote Sensing*, 27(21), 4751-4767. doi:10.1080/01431160600702681

Agüera, F., Aguilar, F. J., & Aguilar, M. A. (2008). Using texture analysis to improve per-pixel classification of very high resolution images for mapping plastic greenhouses. *ISPRS Journal of Photogrammetry and Remote Sensing*, 63(6), 635-646. doi:10.1016/j.isprsjprs.2008.03.003

Aguilar, M. A., Aguilar, F. J., García Lorca, A., Guirado, E., Betlej, M., Cichon, P., Nemmaoui, A., Vallario, A., & Parente, C. (2016b). Assessment of Multiresolution Segmentation for Extracting Greenhouses from Worldview-2 Imagery. *ISPRS - International Archives of the Photogrammetry, Remote Sensing and Spatial Information Sciences*, XLI-B7, 145-152. doi:10.5194/isprsarchives-XLI-B7-145-2016

Aguilar, M. A., Jiménez-Lao, R., & Aguilar, F. J. (2021). Evaluation of Object-Based Greenhouse Mapping Using WorldView-3 VNIR and SWIR Data: A Case Study from Almería (Spain). *Remote Sensing*, 13(11). doi:10.3390/rs13112133

Aguilar, M. A., Jiménez-Lao, R., Ladisa, C., Aguilar, F. J., & Tarantino, E. (2022). Comparison of spectral indices extracted from Sentinel-2 images to map plastic covered greenhouses through an object-based approach. *GIScience & Remote Sensing*, 59(1), 822-842. doi:10.1080/15481603.2022.2071057

Aguilar, M. Á., Jiménez-Lao, R., Nemmaoui, A., Aguilar, F. J., Koc-San, D., Tarantino, E., & Chourak, M. (2020). Evaluation of the Consistency of Simultaneously Acquired Sentinel-2 and Landsat 8 Imagery on Plastic Covered Greenhouses. *Remote Sensing*, 12(12). doi:10.3390/rs12122015

Aguilar, M. A., Novelli, A., Nemamoui, A., Aguilar, F. J., García Lorca, A., & González-Yebra, Ó. (2018). Optimizing Multiresolution Segmentation for Extracting Plastic Greenhouses from WorldView-3 Imagery. Paper presented at the *Intelligent Interactive Multimedia Systems and Services*, Vilamoura, Portugal, 21–23 June 2017; Springer: Berlin/Heidelberg, Germany, 2018; pp. 31–40.

Aguilar, M., Bianconi, F., Aguilar, F., & Fernández, I. (2014). Object-Based Greenhouse Classification from GeoEye-1 and WorldView-2 Stereo Imagery. *Remote Sensing*, 6(5), 3554-3582. doi:10.3390/rs6053554

Aguilar, M., Nemmaoui, A., Novelli, A., Aguilar, F., & García Lorca, A. (2016a). Object-Based Greenhouse Mapping Using Very High Resolution Satellite Data and Landsat 8 Time Series. *Remote Sensing*, 8(6). doi:10.3390/rs8060513

Aguilar, M., Vallario, A., Aguilar, F., Lorca, A., & Parente, C. (2015). Object-Based Greenhouse Horticultural Crop Identification from Multi-Temporal Satellite Imagery: A Case Study in Almeria, Spain. *Remote Sensing*, 7(6), 7378-7401. doi:10.3390/rs70607378

Arcidiacono, C., & Porto, S. M. C. (2010). A model to manage crop-shelter spatial development by multi-temporal coverage analysis and spatial indicators. *Biosystems Engineering*, 107(2), 107-122. doi:10.1016/j.biosystemseng.2010.07.007

Arcidiacono, C., & Porto, S. M. C. (2011). Improving per-pixel classification of crop-shelter coverage by texture analyses of high-resolution satellite panchromatic images. *Journal of Agricultural Engineering*, 4, 9-16.

Aznar-Sanchez, J. A., Velasco-Munoz, J. F., Lopez-Felices, B., & Roman-Sanchez, I. M. (2020). An Analysis of Global Research Trends on Greenhouse Technology: Towards a Sustainable Agriculture. *International Journal of Environmental Research Public Health*, 17(2). doi:10.3390/ijerph17020664

Baatz, M., & Schäpe, A. (2000). Multiresolution Segmentation: an optimization approach for high quality multi-scale image segmentation. *Angewandte Geographische Informationsverarbeitung XII: Beiträge zum AGIT-Symposium*, Salzburg.

Bektas Balcik, F., Senel, G., & Goksel, C. (2020). Object-Based Classification of Greenhouses Using Sentinel-2 MSI and SPOT-7 Images: A Case Study from Anamur (Mersin), Turkey. *IEEE Journal of Selected Topics in Applied Earth Observations and Remote Sensing*, 13, 2769-2777. doi:10.1109/jstars.2020.2996315

Belgiu, M., & Drăguţ, L. (2014). Comparing supervised and unsupervised multiresolution segmentation approaches for extracting buildings from very high resolution imagery. *ISPRS Journal of Photogrammetry and Remote Sensing*, 96, 67-75. doi:10.1016/j.isprsjprs.2014.07.002

Belgiu, M., & Drăguţ, L. (2016). Random forest in remote sensing: A review of applications and future directions. *ISPRS Journal of Photogrammetry and Remote Sensing*, 114, 24-31. doi:10.1016/j.isprsjprs.2016.01.011

Benz, U. C., Hofmann, P., Willhauck, G., Lingenfelder, I., & Heynen, M. (2004). Multi-resolution, object-oriented fuzzy analysis of remote sensing data for GIS-ready information. *ISPRS Journal of Photogrammetry and Remote Sensing*, 58(3-4), 239-258. doi:10.1016/j.isprsjprs.2003.10.002

Berk, A., Bernstein, L. S., Anderson, G. P., Acharya, P. K., Robertson, D. C., Chetwynd, J. H., & Adler-Golden, S. M. (1998). MODTRAN Cloud and Multiple Scattering Upgrades with Application to AVIRIS. *Remote Sensing of Environment*, 65(3), 367-375. doi:10.1016/S0034-4257(98)00045-5

Blaschke, T. (2010). Object based image analysis for remote sensing. *ISPRS Journal of Photogrammetry and Remote Sensing*, 65(1), 2-16. doi:10.1016/j.isprsjprs.2009.06.004

Breiman, L. (2001). Random Forests. *Machine Learning*, 45, 5-32. doi:10.1023/A:1010933404324

Brundtland Commission. (1987). *Report of the World Commission on Environment and Development: Our Common Future*. Retrieved from https://sustainabledevelopment.un.org/content/documents/5987our-common-future.pdf

Campbell, J. B., & Wynne, R. H. (2011). *Introduction to Remote Sensing* (Fifth Edition ed.). New York: The Guillford Press.

Chaofan, W., Jinsong, D., Ke, W., Ligang, M., & Tahmassebi, A. R. S. (2016). Object-based classification approach for greenhouse mapping using Landsat-8 imagery. International *Journal of Agriculture & Biological Engineering*, 9(1), 79-88. doi:10.3965/j.ijabe.20160901.1414

Chen, G., Weng, Q., Hay, G. J., & He, Y. (2018a). Geographic object-based image analysis (GEOBIA): emerging trends and future opportunities. *GIScience & Remote Sensing*, 55(2), 159-182. doi:10.1080/15481603.2018.1426092

Chen, T., & Guestrin, C. (2016). XGBoost: A Scalable Tree Boosting System *Proceedings of the 22nd ACM SIGKDD International Conference on Knowledge Discovery and Data Mining*, San Francisco, California, USA, August 13-17, 785-794.

Chen, W., Xu, Y., Zhang, Z., Yang, L., Pan, X., & Jia, Z. (2021). Mapping agricultural plastic greenhouses using Google Earth images and deep learning. *Computers and Electronics in Agriculture*, 191. doi:10.1016/j.compag.2021.106552

Chen, Y., Ming, D., Zhao, L., Lv, B., Zhou, K., & Qing, Y. (2018b). Review on High Spatial Resolution Remote Sensing Image Segmentation Evaluation. *Photogrammetric Engineering & Remote Sensing*, 84(10), 629-646. doi:10.14358/pers.84.10.629

Chen, Z., Wu, Z., Gao, J., Cai, M., Yang, X., Chen, P., & Li, Q. (2022). A Convolutional Neural Network for Large-Scale Greenhouse Extraction from Satellite Images Considering Spatial Features. *Remote Sensing*, 14(19). doi:10.3390/rs14194908

Clinton, N., Holt, A., Scarborough, J., Yan, L., & Gong, P. (2010). Accuracy assessment measures for object-based image segmentation goodness. *Photogrammetric Engineering and Remote Sensing*, 76(3), 289-299.

Congalton, R. G. (1991). A Review of Assessing the Accuracy of Classifications of Remotely Sensed Data. *Remote Sensing of Environment*, 37(1), 35-46. doi:10.1016/0034-4257(91)90048-B

Costa, G. A. O. P., Feitosa, R. Q., Cazes, T. B., & Feijó, B. (2008). Genetic adaptation of segmentation parameters. In T. Blaschke, S. Lang, & G. J. Hay (Eds.), *Object-Based Image Analysis: Spatial Concepts for Knowledge-Driven Remote Sensing Applications* (pp. 679-695). Berlin, Heidelberg: Springer Berlin Heidelberg.

Costa, H., Foody, G. M., & Boyd, D. S. (2018). Supervised methods of image segmentation accuracy assessment in land cover mapping. *Remote Sensing of Environment*, 205, 338-351. doi:10.1016/j.rse.2017.11.024

Digital Globe. (2014). *Worldview-3 Data Sheet*. Retrieved from http://satimagingcorp .s3.amazonaws.com/site/pdf/WorldView3-DS-WV3-Web.pdf

Ding, H., Na, J., Jiang, S., Zhu, J., Liu, K., Fu, Y., & Li, F. (2021). Evaluation of Three Different Machine Learning Methods for Object-Based Artificial Terrace Mapping—A Case Study of the Loess Plateau, China. *Remote Sensing*, 13(5). doi:10.3390/rs13051021

eCognition Developer 9.0 Reference Book. (2014). Munich, Germany: Trimble Germany GmbH.

Feng, J., Wang, D., Yang, F., Huang, J., Wang, M., Tao, M., & Chen, W. (2022). PODD: A Dual-Task Detection for Greenhouse Extraction Based on Deep Learning. *Remote Sensing*, 14(19). doi:10.3390/rs14195064

Feng, Q., Niu, B., Chen, B., Ren, Y., Zhu, D., Yang, J., Liu, J., Ou, C., & Li, B. (2021). Mapping of plastic greenhouses and mulching films from very high resolution remote sensing imagery based on a dilated and non-local convolutional neural network. *International Journal of Applied Earth Observation and Geoinformation*, 102. doi:10.1016/j.jag.2021.102441

Food and Agriculture Organization of the United Nations. (2008). *Investing in sustainable agricultural intensification: The role of conservation agriculture, A framework for action*. Rome, Italy. Retrieved from https://www.fao.org/sustainable-food-value-chains/library/ details/en/ c/266308/

Freund, Y., & Schapire, R. E. (1997). A Decision-Theoretic Generalization of On-Line Learning and an Application to Boosting. *Journal of Computer and System Science*, 55, 119-139.

Friedman, J. H. (2001). Greedy Function Approximation: A Gradient Boosting Machine, *The Annals of Statistics*, 29(5), 1189–1232.

González-Yebra, Ó., Aguilar, M. A., Nemmaoui, A., & Aguilar, F. J. (2018). Methodological proposal to assess plastic greenhouses land cover change from the combination of archival aerial orthoimages and Landsat data. *Biosystems Engineering*, 175, 36-51. doi:10.1016/j.biosystemseng.2018.08.009

Hamedianfar, A., Gibril, M. B. A., Hosseinpoor, M., & Pellikka, P. K. E. (2020). Synergistic use of particle swarm optimization, artificial neural network, and extreme gradient boosting algorithms for urban LULC mapping from WorldView-3 images. *Geocarto International*, 1-19. doi:10.1080/10106049.2020.1737974

Hao, P., Chen, Z., Tang, H., Li, D., & Li, H. (2019). New Workflow of Plastic-Mulched Farmland Mapping using Multi-Temporal Sentinel-2 data. *Remote Sensing*, 11(11). doi:10.3390/rs11111353

Hasan, M. K., Desiere, S., D'Haese, M., & Kumar, L. (2018). Impact of climate-smart agriculture adoption on the food security of coastal farmers in Bangladesh. *Food Security,* 10(4), 1073-1088. doi:10.1007/s12571-018-0824-1

Hasituya, Chen, Z., Li, F., & Hongmei. (2017). Mapping Plastic-Mulched Farmland with C-Band Full Polarization SAR Remote Sensing Data. *Remote Sensing*, 9(12). doi:10.3390/rs9121264

Hasituya, Chen, Z., Wang, L., Wu, W., Jiang, Z., & Li, H. (2016). Monitoring Plastic-Mulched Farmland by Landsat-8 OLI Imagery Using Spectral and Textural Features. *Remote Sensing*, 8(4). doi:10.3390/rs8040353

Hasituya, Zhongxin, C., Fei, L., & Yuncai, H. (2020). Mapping plastic-mulched farmland by coupling optical and synthetic aperture radar remote sensing. *International Journal of Remote Sensing*, 41(20), 7757-7778. doi:10.1080/01431161.2020.1763510

Hay, G. J., Blaschke, T., Marceau, D. J., & Bouchard, A. (2003). A comparison of three image-object methods for the multiscale analysis of landscape structure. *ISPRS Journal of Photogrammetry and Remote Sensing*, 57(5-6), 327-345. doi:10.1016/s0924-2716(02)00162-4

Hossain, M. D., & Chen, D. (2019). Segmentation for Object-Based Image Analysis (OBIA): A review of algorithms and challenges from remote sensing perspective. *ISPRS Journal of Photogrammetry and Remote Sensing*, 150, 115-134. doi:10.1016/j.isprsjprs.2019.02.009

Janssen, L. L. F., & Molenaar, M. (1995). Terrain objects, their dynamics and their monitoring by the integration of GIS and remote sensing. *IEEE Transactions on Geoscience and Remote Sensing*, 33(3), 749-758. doi:10.1109/36.387590

Ji, L., Zhang, L., Shen, Y., Li, X., Liu, W., Chai, Q., Zhang, R., & Chen, D. (2019). Object-Based Mapping of Plastic Greenhouses with Scattered Distribution in Complex Land Cover Using Landsat 8 OLI Images: A Case Study in Xuzhou, China. *Journal of the Indian Society of Remote Sensing*, 48(2), 287-303. doi:10.1007/s12524-019-01081-8

Jiménez-Lao, R., Aguilar, F. J., Nemmaoui, A., & Aguilar, M. A. (2020). Remote Sensing of Agricultural Greenhouses and Plastic-Mulched Farmland: An Analysis of Worldwide Research. *Remote Sensing*, 12(16). doi:10.3390/rs12162649

Jobin, B., Labrecque, S., Grenier, M., & Falardeau, G. (2008). Object-based classification as an alternative approach to the traditional pixel-based classification to identify potential habitat of the grasshopper sparrow. *Environmental Management*, 41(1), 20-31. doi:10.1007/s00267-007-9031-0

Jozdani, S., & Chen, D. (2020). On the versatility of popular and recently proposed supervised evaluation metrics for segmentation quality of remotely sensed images: An experimental case study of building extraction. *ISPRS Journal of Photogrammetry and Remote Sensing*, 160, 275-290. doi:10.1016/j.isprsjprs.2020.01.002

Kavzoglu, T., & Colkesen, I. (2009). A kernel functions analysis for support vector machines for land cover classification. *International Journal of Applied Earth Observation and Geoinformation*, 11(5), 352-359. doi:10.1016/j.jag.2009.06.002

Ke, G., Meng, Q., Finley, T., Wang, T., Chen, W., Ma, W., Ye, Q., & Liu, T.-Y. (2017). LightGBM: A Highly Efficient Gradient Boosting Decision Tree. *31st Conference on Neural Information Processing Systems* (NIPS 2017), Long Beach, CA, USA.

Koc-San, D. (2013). Evaluation of different classification techniques for the detection of glass and plastic greenhouses from WorldView-2 satellite imagery. *Journal of Applied Remote Sensing*, 7(1). doi:10.1117/1.Jrs.7.073553

Kucharczyk, M., Hay, G. J., Ghaffarian, S., & Hugenholtz, C. H. (2020). Geographic Object-Based Image Analysis: A Primer and Future Directions. *Remote Sensing*, 12(12). doi:10.3390/rs12122012

Lagrari, F.-E., Ziyati, H., & Kettani, Y. E. (2019). An Efficient Model of Text Categorization Based on Feature Selection and Random Forests: Case for Business Documents. *Advanced Intelligent Systems for Sustainable Development (AI2SD'2018),* Cham.

Levin, N., Lugassi, R., Ramon, U., Braun, O., & Ben-Dor, E. (2007). Remote sensing as a tool for monitoring plasticulture in agricultural landscapes. *International Journal of Remote Sensing*, 28(1), 183-202. doi:10.1080/01431160600658156

Levine, M. D., & Nazif, A. (1982). An experimental rule-based system for testing low level segmentation strategies. *Multicomputers and Image Processing: Algorithms and Programs*, 149-160.

Li, H., Gan, Y., Wu, Y., & Guo, L. (2022). EAGNet: A method for automatic extraction of agricultural greenhouses from high spatial resolution remote sensing images based on hybrid multi-attention. *Computers and Electronics in Agriculture*, 202. doi:10.1016/j.compag.2022.107431

Li, M., Zhang, Z., Lei, L., Wang, X., & Guo, X. (2020). Agricultural Greenhouses Detection in High-Resolution Satellite Images Based on Convolutional Neural Networks: Comparison of Faster R-CNN, YOLO v3 and SSD. *Sensors (Basel)*, 20(17). doi:10.3390/s20174938

Lin, J., Jin, X., Ren, J., Liu, J., Liang, X., & Zhou, Y. (2021). Rapid Mapping of Large-Scale Greenhouse Based on Integrated Learning Algorithm and Google Earth Engine. *Remote Sensing*, 13(7). doi:10.3390/rs13071245

Liu, C.-A., Chen, Z., Wang, D., & Li, D. (2019). Assessment of the X- and C-Band Polarimetric SAR Data for Plastic-Mulched Farmland Classification. *Remote Sensing*, 11(6). doi:10.3390/rs11060660

Liu, J., Feng, Q., Wang, Y., Batsaikhan, B., Gong, J., Li, Y., Liu, C., & Ma, Y. (2020). Urban Green Plastic Cover Mapping Based on VHR Remote Sensing Images and a Deep Semi-Supervised Learning Framework. *ISPRS International Journal of Geo-Information*, 9(9). doi:10.3390/ijgi9090527

Liu, Y., Bian, L., Meng, Y., Wang, H., Zhang, S., Yang, Y., Shao, X., & Wang, B. (2012). Discrepancy measures for selecting optimal combination of parameter values in object-based image analysis. *ISPRS Journal of Photogrammetry and Remote Sensing*, 68, 144-156. doi:10.1016/j.isprsjprs.2012.01.007

Lu, L., Di, L., & Ye, Y. (2014). A Decision-Tree Classifier for Extracting Transparent Plastic-Mulched Landcover from Landsat-5 TM Images. *IEEE Journal of Selected Topics in Applied Earth Observations and Remote Sensing*, 7(11), 4548-4558. doi:10.1109/jstars.2014.2327226

Lu, L., Hang, D., & Di, L. (2015). Threshold model for detecting transparent plastic-mulched landcover using moderate-resolution imaging spectroradiometer time series data: a case study in southern Xinjiang, China. *Journal of Applied Remote Sensing*, 9(1). doi:10.1117/1.Jrs.9.097094

Lu, L., Tao, Y., & Di, L. (2018). Object-Based Plastic-Mulched Landcover Extraction Using Integrated Sentinel-1 and Sentinel-2 Data. *Remote Sensing*, 10(11). doi:10.3390/rs10111820

Lucieer, A., & Stein, A. (2002). Existential uncertainty of spatial objects segmented from satellite sensor imagery. *IEEE Transactions on Geoscience and Remote Sensing*, 40(11), 2518-2521. doi:10.1109/tgrs.2002.805072

Ma, A., Chen, D., Zhong, Y., Zheng, Z., & Zhang, L. (2021a). National-scale greenhouse mapping for high spatial resolution remote sensing imagery using a dense object dual-task deep learning framework: A case study of China. *ISPRS Journal of Photogrammetry and Remote Sensing*, 181, 279-294. doi:10.1016/j.isprsjprs.2021.08.024

Ma, H., Feng, T., Shen, X., Luo, Z., Chen, P., & Guan, B. (2021b). Greenhouse extraction with high-resolution remote sensing imagery using fused fully convolutional network and object-oriented image analysis. *Journal of Applied Remote Sensing*, 15(04). doi:10.1117/1.Jrs.15.046502

Ma, L., Fu, T., Blaschke, T., Li, M., Tiede, D., Zhou, Z., Ma, X., & Chen, D. (2017a). Evaluation of Feature Selection Methods for Object-Based Land Cover Mapping of Unmanned Aerial Vehicle Imagery Using Random Forest and Support Vector Machine Classifiers. *ISPRS International Journal of Geo-Information*, 6(2). doi:10.3390/ijgi6020051

Ma, L., Li, M., Ma, X., Cheng, L., Du, P., & Liu, Y. (2017b). A review of supervised object-based land-cover image classification. *ISPRS Journal of Photogrammetry and Remote Sensing*, 130, 277-293. doi:10.1016/j.isprsjprs.2017.06.001

Mesner, N., & Oštir, K. (2014). Investigating the impact of spatial and spectral resolution of satellite images on segmentation quality. *Journal of Applied Remote Sensing*, 8(1). doi:10.1117/1.Jrs.8.083696

Microsoft Corporation. (2021). LightGBM Release 3.2.1. Retrieved from https://lightgbm.readthedocs.io/_/downloads/en/latest/pdf/

Muthoka, J. M., Salakpi, E. E., Ouko, E., Yi, Z.-F., Antonarakis, A. S., & Rowhani, P. (2021). Mapping Opuntia stricta in the Arid and Semi-Arid Environment of Kenya Using Sentinel-2 Imagery and Ensemble Machine Learning Classifiers. *Remote Sensing*, 13(8). doi:10.3390/rs13081494

Nemmaoui, A., Aguilar, M. A., Aguilar, F. J., Novelli, A., & García Lorca, A. (2018). Greenhouse Crop Identification from Multi-Temporal Multi-Sensor Satellite Imagery Using Object-Based Approach: A Case Study from Almería (Spain). *Remote Sensing*, 10(11). doi:10.3390/rs10111751

Neubert, M., Herold, H., & Meinel, G. (2008). Assessing image segmentation quality – concepts, methods and application. In T. Blaschke, S. Lang, & G. J. Hay (Eds.*), Object-Based Image Analysis: Spatial Concepts for Knowledge-Driven Remote Sensing Applications* (pp. 769-784). Berlin, Heidelberg: Springer Berlin Heidelberg.

Novelli, A., & Tarantino, E. (2015). Combining ad hoc spectral indices based on LANDSAT-8 OLI/TIRS sensor data for the detection of plastic cover vineyard. *Remote Sensing Letters*, 6(12), 933-941. doi:10.1080/2150704x.2015.1093186

Novelli, A., Aguilar, M. A., Nemmaoui, A., Aguilar, F. J., & Tarantino, E. (2016). Performance evaluation of object based greenhouse detection from Sentinel-2 MSI and Landsat 8 OLI data: A case study from Almería (Spain). *International Journal of Applied Earth Observation and Geoinformation*, 52, 403-411. doi:10.1016/j.jag.2016.07.011

Novelli, A., Aguilar, M., Aguilar, F., Nemmaoui, A., & Tarantino, E. (2017). AssesSeg—A Command Line Tool to Quantify Image Segmentation Quality: A Test Carried Out in Southern Spain from Satellite Imagery. *Remote Sensing*, 9(1). doi:10.3390/rs9010040

Ou, C., Yang, J., Du, Z., Liu, Y., Feng, Q., & Zhu, D. (2019). Long-Term Mapping of a Greenhouse in a Typical Protected Agricultural Region Using Landsat Imagery and the Google Earth Engine. *Remote Sensing*, 12(1). doi:10.3390/rs12010055

Ou, C., Yang, J., Du, Z., Zhang, T., Niu, B., Feng, Q., Liu, Y., & Zhu, D. (2021). Landsat-Derived Annual Maps of Agricultural Greenhouse in Shandong Province, China from 1989 to 2018. *Remote Sensing*, 13(23). doi:10.3390/rs13234830

Pala, E., Taşdemir, K., & Koc-San, D. (2015). Unsupervised extraction of greenhouses using approximate spectral clustering ensemble. *2015 IEEE International Geoscience and Remote Sensing Symposium (IGARSS)*, July 26-31, Milan, Italy. 10.1109/IGARSS.2015.7326870

Perilla, G. A., & Mas, J.-F. (2019). High-resolution mapping of protected agriculture in Mexico, through remote sensing data cloud geoprocessing. *European Journal of Remote Sensing*, 52(1), 532-541. doi:10.1080/22797254.2019.1686430

Prokhorenkova, L., Gusev, G., Vorobev, A., Dorogush, A. V., & Gulin, A. (2017). CatBoost: unbiased boosting with categorical features. *arXiv preprint*.

Rouse, J. W., Haas, R. H., Schell, J. A., & Deering, D. W. (1973). Monitoring vegetation systems in the great plains with ERTS. *NASA Goddard Space Flight Center 3d ERTS-1 Symposium*, 1.

Sahin, E. K. (2020). Comparative analysis of gradient boosting algorithms for landslide susceptibility mapping. *Geocarto International*, 1-25. doi:10.1080/10106049.2020.1831623

Salas, E. A. L., & Henebry, G. M. (2012). Separability of maize and soybean in the spectral regions of chlorophyll and carotenoids using the Moment Distance Index. *Israel Journal of Plant Sciences*, 60(1), 65-76. doi:10.1560/ijps.60.1-2.65

Scheffler, D., Hollstein, A., Diedrich, H., Segl, K., & Hostert, P. (2017). AROSICS: An Automated and Robust Open-Source Image Co-Registration Software for Multi-Sensor Satellite Data. *Remote Sensing*, 9(7). doi:10.3390/rs9070676

Senel, G., Aguilar, M. A., Aguilar, F. J., Nemmaoui, A., & Goksel, C. (2023). Unraveling Segmentation Quality of Remotely Sensed Images on Plastic-Covered Greenhouses: A Rigorous Experimental Analysis from Supervised Evaluation Metrics. *Remote Sensing*, 15(2). doi:10.3390/rs15020494

Sentinel-2 Products Specification Document. (2021). Retrieved from https://sentinel.esa.int/documents/247904/685211/Sentinel-2-Products-Specification-Document

Sheykhmousa, M., Mahdianpari, M., Ghanbari, H., Mohammadimanesh, F., Ghamisi, P., & Homayouni, S. (2020). Support Vector Machine Versus Random Forest for Remote Sensing Image Classification: A Meta-Analysis and Systematic Review. *IEEE Journal of Selected Topics in Applied Earth Observations and Remote Sensing*, 13, 6308-6325. doi:10.1109/jstars.2020.3026724

Shi, L., Huang, X., Zhong, T., & Taubenbock, H. (2020). Mapping Plastic Greenhouses Using Spectral Metrics Derived From GaoFen-2 Satellite Data. *IEEE Journal of Selected Topics in Applied Earth Observations and Remote Sensing*, 13, 49-59. doi:10.1109/jstars.2019.2950466

Sönmez, N. K., & Sarı, M. (2006). Use of Remote Sensing and Geographic Information System Technologies for Developing Greenhouse Database. *Turkish Journal of Agriculture and Forestry*, 30.

Sun, H., Wang, L., Lin, R., Zhang, Z., & Zhang, B. (2021). Mapping Plastic Greenhouses with Two-Temporal Sentinel-2 Images and 1D-CNN Deep Learning. *Remote Sensing*, 13(14). doi:10.3390/rs13142820

T.C. Aksu District Governorship. (2023). Retrieved from http://www. antalyaaksu.gov.tr/tarim

Tarantino, E., & Figorito, B. (2012). Mapping Rural Areas with Widespread Plastic Covered Vineyards Using True Color Aerial Data. *Remote Sensing*, 4(7), 1913-1928. doi:10.3390/rs4071913

Taşdemir, K., & Koc-San, D. (2014). Unsupervised extraction of greenhouses using Worldview-2 images. *2014 IEEE Geoscience and Remote Sensing Symposium*, Quebec City, QC, Canada, July 13-18.

Tian, J., & Chen, D. M. (2007). Optimization in multi-scale segmentation of high-resolution satellite images for artificial feature recognition. *International Journal of Remote Sensing*, 28(20), 4625-4644. doi:10.1080/01431160701241746

Tilman, D., Balzer, C., Hill, J., & Befort, B. L. (2011). Global food demand and the sustainable intensification of agriculture. *Proceedings of the National Academy of Sciences*, 108(50), 20260-20264. doi:10.1073/pnas. 1116437108

Tiwari, A., Silver, M., & Karnieli, A. (2020). Developing object-based image procedures for classifying and characterising different protected agriculture structures using LiDAR and orthophoto. *Biosystems Engineering*, 198, 91-104. doi:10.1016/j.biosystemseng.2020.07.017

Tong, H., Maxwell, T., Zhang, Y., & Dey, V. (2012). A Supervised and Fuzzy-based Approach to Determine Optimal Multi-resolution Image Segmentation Parameters. *Photogrammetric Engineering & Remote Sensing*, 78(10), 1029-1044. doi:https://doi.org/10.14358/PERS.78.10.1029

TÜİK. (2020). Bitkisel Üretim İstatistikleri. Retrieved from https://biruni.tuik.gov.tr /medas /?kn=92&locale=tr

Tuya, H., Zhongxin, C., Zhenwang, L., & Fei, L. (2021). Potential of Pléiades and Radarsat-2 Data for Mapping Plastic-Mulched Farmland Using Object-Based Image Analysis. *Canadian Journal of Remote Sensing*, 47(4), 607-620. doi:10.1080/07038992.2021.1946384

Ustuner, M., & Balik Sanli, F. (2019). Polarimetric Target Decompositions and Light Gradient Boosting Machine for Crop Classification: A Comparative Evaluation. *ISPRS International Journal of Geo-Information*, 8(2). doi:10.3390/ijgi8020097

Üstüner, M., Abdikan, S., Bilgin, G., & Balık Şanlı, F. (2020). Hafif Gradyan Artırma Makineleri ile Tarımsal Ürünlerin Sınıflandırılması. *Turkish Journal of Remote Sensing and GIS (Türk Uzaktan Algılama ve CBS Dergisi)*, 1(2), 97-105.

Vapnik, V. (2006). *Estimation of dependences based on empirical data*. Springer Science & Business Media.

Wang, B., Zhang, Z., Wang, X., Zhao, X., Yi, L., & Hu, S. (2020). Object-Based Mapping of Gullies Using Optical Images: A Case Study in the Black Soil Region, Northeast of China. *Remote Sensing*, 12(3). doi:10.3390/rs12030487

Weidner, U. (2008). Contribution To The Assessment Of Segmentation Quality For Remote Sensing Applications. *The International Archives of the Photogrammetry, Remote Sensing and Spatial Information Sciences*, Beijing.

Western Mediterranean Development Agency. (2019). Bati Akdeniz Bölgesi Ekonomik Göstergeler. Retrieved from https://www.baka.gov.tr/assets /upload/dosyalar/1561647860BATiAKDENiZBoLGESiEKONOMiK GoSTERGELERHAZiRAN2019.pdf

Xiong, Y., Zhang, Q., Chen, X., Bao, A., Zhang, J., & Wang, Y. (2019). Large Scale Agricultural Plastic Mulch Detecting and Monitoring with Multi-Source Remote Sensing Data: A Case Study in Xinjiang, China. *Remote Sensing*, 11(18). doi:10.3390/rs11182088

Yang, D., Chen, J., Zhou, Y., Chen, X., Chen, X., & Cao, X. (2017). Mapping plastic greenhouse with medium spatial resolution satellite data: Development of a new spectral index. *ISPRS Journal of Photogrammetry and Remote Sensing*, 128, 47-60. doi:10.1016/j.isprsjprs.2017.03.002

Yang, J., Li, P., & He, Y. (2014). A multi-band approach to unsupervised scale parameter selection for multi-scale image segmentation. *ISPRS Journal of Photogrammetry and Remote Sensing*, 94, 13-24. doi:10.1016/j.isprsjprs.2014.04.008

Yao, Y., & Wang, S. (2019). Evaluating the Effects of Image Texture Analysis on Plastic Greenhouse Segments via Recognition of the OSI-USI-ETA-CEI Pattern. *Remote Sensing*, 11(3). doi:10.3390/rs11030231

Yao, Y., & Wang, S. (2022). Effects of Atmospheric Correction and Image Enhancement on Effective Plastic Greenhouse Segments Based on a Semi-Automatic Extraction Method. *ISPRS International Journal of Geo-Information*, 11(12). doi:10.3390/ijgi11120585

Zha, Y., Gao, J., & Ni, S. (2003). Use of normalized difference built-up index in automatically mapping urban areas from TM imagery. *International Journal of Remote Sensing*, 24(3), 583-594. doi:10.1080/01431160304987

Zhang, H., Fritts, J. E., & Goldman, S. A. (2008). Image segmentation evaluation: A survey of unsupervised methods. *Computer Vision and Image Understanding*, 110(2), 260-280. doi:10.1016/j.cviu.2007.08.003

Zhang, P., Du, P., Guo, S., Zhang, W., Tang, P., Chen, J., & Zheng, H. (2022). A novel index for robust and large-scale mapping of plastic greenhouse from Sentinel-2 images. *Remote Sensing of Environment*, 276. doi:10.1016/j.rse.2022.113042

Zhang, X., Cheng, B., Chen, J., & Liang, C. (2021). High-Resolution Boundary Refined Convolutional Neural Network for Automatic Agricultural Greenhouses Extraction from GaoFen-2 Satellite Imageries. *Remote Sensing*, 13(21). doi:10.3390/rs13214237

Zhang, X., Feng, X., Xiao, P., He, G., & Zhu, L. (2015). Segmentation quality evaluation using region-based precision and recall measures for remote sensing images. *ISPRS Journal of Photogrammetry and Remote Sensing*, 102, 73-84. doi:10.1016/j.isprsjprs.2015.01.009

Zhang, Y. J. (1996). A survey on evaluation methods for image segmentation. *Pattern Recognition*, 29, 1335–1346. doi:10.1016/0031-3203(95)00169-7

Zhao, G., J. Li, T. Li, and T. Warner. (2004). Utilizing Landsat TM Imagery to Map Greenhouses in Qingzhou, Shandong Province, China. *Pedosphere*, 14 (3): 363–369.

Url-1 <https://CRAN.R-project.org/package=segmetric>, accessed on 20.01.2023.

Url-2 <https://scikit-learn.org/stable/modules/generated/sklearn.feature_selection.chi2.html#sklearn.feature_selection.chi2>, accessed on 20.01.2023.

Url-3 <https://scikit-learn.org/stable/modules/generated/sklearn.feature_selection.RFE.html>, accessed on 20.01.2023.

Url-4 <https://scikit-learn.org/stable/modules/neighbors.html#classification>, accessed on 20.01.2023.

APPENDICES

APPENDIX A: Tables regarding the experimental design for image segmentation stage.

APPENDIX A: Tables regarding the experimental design for image segmentation stage.

Table A.1 : Optimal segmentations determined through visual inspections for Almería study site, winter season, and WorldView-3 (WV3) orthoimages (Percent and 16Bits). SP: MRS segmentation scale. I: Interpreter.

	SP	I-1	I-2	I-3	I-4	I-5	I-6	Median
Almeria December WV3 Percent	35	5	3	5	10	4	8	5.0
	40	4	2	6	7	3	10	5.0
	45	2	1	4	3	5	3	3.0
	50	1	4	1	1	6	1	1.0
	55	3	5	2	4	1	5	3.5
	60	6	6	3	5	2	2	4.0
	65	7	7	7	2	8	4	7.0
	70	8	8	8	6	7	7	7.5
	75	9	9	9	8	9	6	9.0
	80	10	10	10	9	10	9	10.0
Almeria December WV3 16Bits	180	10	9	9	10	10	10	10.0
	220	9	10	10	9	9	9	9.0
	260	8	7	8	8	8	7	8.0
	300	7	6	7	7	6	6	6.5
	340	6	4	6	6	5	4	5.5
	380	4	1	5	5	4	5	4.5
	420	1	2	3	2	1	3	2.0
	460	2	3	4	1	2	1	2.0
	500	3	5	1	3	3	2	3.0
	540	5	8	2	4	7	8	6.0

Table A.2 : Optimal segmentations determined through visual inspections for Almería study site, winter season, and Sentinel-2 orthoimages (Percent and 16Bits). SP: MRS segmentation scale. I: Interpreter.

	SP	I-1	I-2	I-3	I-4	I-5	I-6	Median
Almeria December Sentinel-2 Percent	2	8	9	10	10	10	10	10.0
	3	5	8	9	9	7	9	8.5
	4	3	4	8	5	4	8	4.5
	5	1	2	4	2	3	7	2.5
	6	2	1	1	1	2	2	1.5
	7	4	3	2	4	1	1	2.5
	8	6	5	7	3	8	3	5.5
	9	7	7	5	6	5	5	5.5
	10	9	6	6	7	9	4	6.5
	11	10	10	3	8	6	6	7.0
Almeria December Sentinel-2 16Bits	15	10	7	10	10	10	10	10
	20	9	9	9	9	8	9	9
	25	6	6	8	8	7	6	6.5
	30	4	4	7	4	5	8	4.5
	35	3	2	6	2	2	4	2.5
	40	1	1	3	1	3	3	2
	45	2	3	1	3	1	2	2
	50	5	10	2	5	4	1	4.5
	55	7	5	5	6	9	5	5.5
	60	8	8	4	7	6	7	7

Table A.3 : Optimal segmentations determined through visual inspections for Almería study site, summer season, and WorldView-3 (WV3) orthoimages (Percent and 16Bits). SP: MRS segmentation scale. I: Interpreter.

	SP	I-1	I-2	I-3	I-4	I-5	I-6	Median
Almeria June WV3 Percent	20	9	10	10	10	10	10	10.0
	30	5	9	9	9	9	9	9.0
	40	3	8	3	4	6	3	3.5
	50	1	3	1	1	4	2	1.5
	60	2	2	4	2	1	1	2.0
	70	4	5	2	3	5	4	4.0
	80	6	4	7	6	7	8	6.5
	90	7	1	5	5	2	7	5.0
	100	8	6	6	7	3	6	6.0
	110	10	7	8	8	8	5	8.0
Almeria June WV3 16Bits	190	9	10	10	10	10	10	10.0
	245	7	9	9	9	9	9	9.0
	300	4	8	8	8	8	8	8.0
	355	3	7	7	7	5	2	6.0
	410	2	6	6	3	7	7	6.0
	465	1	5	5	1	6	6	5.0
	520	5	4	1	2	3	1	2.5
	575	6	3	2	4	4	5	4.0
	630	8	2	3	5	2	4	3.5
	685	10	1	4	6	1	3	3.5

Table A.4 : Optimal segmentations determined through visual inspections for Almería study site, summer season, and Sentinel-2 orthoimages (Percent and 16Bits). SP: MRS segmentation scale. I: Interpreter.

	SP	I-1	I-2	I-3	I-4	I-5	I-6	Median
Almeria June Sentinel-2 Percent	2	10	10	10	6	10	10	10.0
	3	7	9	9	2	9	9	9.0
	4	6	8	8	10	8	8	8.0
	5	4	7	3	3	3	2	3.0
	6	2	6	1	4	7	1	3.0
	7	1	1	4	7	6	3	3.5
	8	3	5	2	1	2	5	2.5
	9	5	3	5	8	1	4	4.5
	10	8	4	6	9	5	7	6.5
	11	9	2	7	5	4	6	5.5
Almeria June Sentinel-2 16Bits	15	10	10	10	8	10	10	10.0
	20	9	9	9	3	9	9	9.0
	25	8	8	8	6	8	8	8.0
	30	7	7	7	1	6	6	6.5
	35	6	6	6	10	7	5	6.0
	40	4	5	5	5	4	7	5.0
	45	3	4	3	4	5	3	3.5
	50	1	3	2	9	3	4	3.0
	55	2	2	1	2	2	1	2.0
	60	5	1	4	7	1	2	3.0

Table A.5 : Optimal segmentations determined through visual inspections for Antalya study site, winter season, and SPOT-7 orthoimages (Percent and 16Bits). SP: MRS segmentation scale. I: Interpreter.

	SP	I-1	I-2	I-3	I-4	I-5	I-6	Median
Antalya February SPOT-7 Percent	15	6	3	5	5	8	9	5.5
	20	4	2	4	3	3	6	3.5
	25	1	1	3	1	5	1	1.0
	30	2	4	1	2	4	2	2.0
	35	3	5	2	4	1	3	3.0
	40	5	6	6	7	2	4	5.5
	45	7	7	7	6	6	5	6.5
	50	8	8	8	8	7	7	8.0
	55	9	9	9	9	9	8	9.0
	60	10	10	10	10	10	10	10.0
Antalya February SPOT-7 16Bits	150	10	10	9	10	10	10	10.0
	170	9	9	10	4	9	9	9.0
	190	8	8	7	3	8	8	8.0
	210	7	7	8	1	7	1	7.0
	230	5	6	5	2	1	2	3.5
	250	2	5	3	5	6	4	4.5
	270	1	4	1	6	2	3	2.5
	290	3	2	2	7	4	5	3.5
	310	4	3	6	8	3	6	5.0
	330	6	1	4	9	5	7	5.5

Table A.6 : Optimal segmentations determined through visual inspections for Antalya study site, winter season, and Sentinel-2 orthoimages (Percent and 16Bits). I: Interpreter. SP: MRS segmentation scale. I: Interpreter.

	SP	I-1	I-2	I-3	I-4	I-5	I-6	Median
Antalya February Sentinel-2 Percent	2	7	10	10	8	10	7	9.0
	3	4	2	9	1	9	6	5.0
	4	2	1	4	2	4	1	2.0
	5	1	3	3	3	2	2	2.5
	6	3	4	2	4	1	3	3.0
	7	5	5	1	5	3	4	4.5
	8	6	6	5	6	5	5	5.5
	9	8	7	7	7	6	8	7.0
	10	9	8	6	9	7	9	8.5
	11	10	9	8	10	8	10	9.5
Antalya February Sentinel-2 16Bits	15	10	10	10	9	10	10	10.0
	20	7	9	9	10	8	9	9.0
	25	4	3	1	3	1	7	3.0
	30	3	4	2	1	2	2	2.0
	35	2	1	4	2	3	1	2.0
	40	1	5	3	4	4	3	3.5
	45	5	2	5	5	5	4	5.0
	50	6	6	8	6	7	5	6.0
	55	8	7	7	7	6	6	7.0
	60	9	8	6	8	9	8	8.0

Table A.7 : Optimal segmentations determined through visual inspections for Antalya study site, summer season, and SPOT-7 orthoimages (Percent and 16Bits). SP: MRS segmentation scale. I: Interpreter.

	SP	I-1	I-2	I-3	I-4	I-5	I-6	Median
Antalya July SPOT-7 Percent	15	6	7	10	6	10	9	8.0
	20	3	4	9	4	5	6	4.5
	25	1	1	2	1	2	1	1.0
	30	2	2	1	2	1	2	2.0
	35	4	3	3	3	3	3	3.0
	40	5	5	4	5	4	4	4.5
	45	7	6	5	7	6	5	6.0
	50	8	8	6	8	7	7	7.5
	55	9	9	7	9	8	8	8.5
	60	10	10	5	10	9	10	10.0
Antalya July SPOT-7 16Bits	140	10	10	10	8	10	10	10.0
	170	8	9	9	9	9	9	9.0
	200	5	8	7	6	5	8	6.5
	230	3	7	6	3	6	2	4.5
	260	1	6	5	1	4	1	2.5
	290	2	5	4	2	1	3	2.5
	320	4	2	1	4	2	4	3.0
	350	6	1	2	5	3	5	4.0
	380	7	3	3	7	7	6	6.5
	410	9	4	8	10	8	7	8.0

Table A.8 : Optimal segmentations determined through visual inspections for Antalya study site, summer season, and Sentinel-2 orthoimages (Percent and 16Bits). SP: MRS segmentation scale. I: Interpreter.

	SP	I-1	I-2	I-3	I-4	I-5	I-6	Median
Antalya July Sentinel-2 Percent	3	4	6	10	10	10	8	9.0
	4	2	5	9	1	7	7	6.0
	5	1	2	8	2	2	1	2.0
	6	3	1	2	3	1	2	2.0
	7	5	3	1	4	4	3	3.5
	8	6	7	5	5	3	4	5.0
	9	7	8	3	6	6	5	6.0
	10	8	4	4	7	5	6	5.5
	11	9	10	6	8	8	9	8.5
	12	10	9	7	9	9	10	9.0
Antalya July Sentinel-2 16Bits	25	9	10	10	10	10	10	10.0
	30	5	9	9	8	9	9	9.0
	35	4	8	8	5	8	8	8.0
	40	2	7	7	3	7	2	5.0
	45	1	4	6	1	4	1	2.5
	50	3	2	3	2	1	3	2.5
	55	6	3	5	4	3	4	4.0
	60	7	5	4	6	2	5	5.0
	65	8	6	2	7	5	6	6.0
	70	10	1	1	9	6	7	6.5

Table A.9 : Segmentation metrics for Almería study site, winter season, and WorldView-3.

	SP	Object	ED2	AFI	D index	ED3	F measure	Fitness	M	QR	Median
Percent	35	3229	0.813	0.084	0.436	0.263	0.508	7.315	0.821	0.582	5.0
	40	2590	0.463	-0.035	0.385	0.210	0.495	5.932	0.840	0.506	5.0
	45	2118	0.344	-0.147	0.355	0.184	0.478	4.902	0.844	0.464	3.0
	50	1774	0.341	-0.327	0.332	0.168	0.459	4.231	0.838	0.432	1.0
	55	1534	0.373	-0.434	0.319	0.158	0.443	3.624	0.826	0.415	3.5
	60	1341	0.493	-0.616	0.300	0.165	0.429	3.126	0.804	0.401	4.0
	65	1189	0.655	-0.856	0.308	0.177	0.407	2.684	0.781	0.415	7.0
	70	1089	0.771	-1.022	0.318	0.187	0.398	2.513	0.764	0.430	7.5
	75	991	0.899	-1.212	0.335	0.204	0.386	2.326	0.740	0.456	9.0
	80	885	1.115	-1.520	0.364	0.225	0.373	2.042	0.708	0.495	10.0
16Bits	180	7206	3.430	0.413	0.604	0.402	0.500	17.547	0.696	0.818	10.0
	220	5074	2.221	0.291	0.571	0.368	0.510	13.070	0.751	0.762	9.0
	260	3762	1.374	0.146	0.517	0.326	0.511	10.158	0.793	0.688	8.0
	300	2967	0.925	0.041	0.474	0.290	0.498	8.519	0.807	0.627	6.5
	340	2358	0.668	-0.106	0.437	0.262	0.479	6.801	0.804	0.578	5.5
	380	1908	0.498	-0.312	0.414	0.234	0.462	5.237	0.795	0.539	4.5
	420	1594	0.447	-0.413	0.388	0.214	0.446	3.637	0.788	0.506	2.0
	460	1384	0.496	-0.583	0.362	0.196	0.436	2.628	0.777	0.472	2.0
	500	1231	0.618	-0.756	0.360	0.191	0.422	2.163	0.763	0.467	3.0
	540	1094	0.808	-1.022	0.364	0.203	0.408	1.680	0.740	0.479	6.0

Table A.10 : Segmentation metrics for Almería study site, winter season, and Sentinel-2.

	SP	Object	ED2	AFI	D index	ED3	F measure	Fitness	M	QR	Median
Percent	2	12345	7.601	0.701	0.661	0.463	0.335	19.375	0.496	0.908	10.0
	3	5441	2.695	0.448	0.592	0.407	0.400	8.367	0.604	0.807	8.5
	4	3226	1.225	0.224	0.515	0.341	0.407	4.931	0.663	0.699	4.5
	5	2188	0.741	-0.031	0.453	0.297	0.393	3.453	0.677	0.622	2.5
	6	1603	0.638	-0.309	0.416	0.272	0.376	2.690	0.674	0.577	1.5
	7	1283	0.749	-0.550	0.392	0.258	0.361	2.249	0.661	0.549	2.5
	8	1010	0.998	-0.916	0.408	0.268	0.344	1.831	0.633	0.568	5.5
	9	828	1.318	-1.411	0.423	0.283	0.326	1.596	0.606	0.591	5.5
	10	692	1.834	-2.028	0.444	0.302	0.317	1.441	0.577	0.621	6.5
	11	579	2.279	-2.740	0.469	0.325	0.307	1.332	0.543	0.657	7.0
16Bits	15	11317	6.166	0.616	0.653	0.455	0.384	26.975	0.562	0.893	10
	20	6435	3.062	0.469	0.610	0.416	0.407	15.124	0.621	0.826	9
	25	4134	1.638	0.325	0.560	0.370	0.411	9.315	0.658	0.752	6.5
	30	3018	1.106	0.123	0.521	0.336	0.407	6.418	0.678	0.698	4.5
	35	2304	0.790	-0.071	0.488	0.306	0.390	4.895	0.682	0.654	2.5
	40	1855	0.698	-0.323	0.461	0.286	0.375	3.921	0.685	0.620	2
	45	1526	0.774	-0.657	0.448	0.279	0.359	3.146	0.666	0.604	2
	50	1291	0.940	-0.923	0.446	0.280	0.346	2.614	0.647	0.601	4.5
	55	1114	1.099	-1.228	0.451	0.283	0.335	2.266	0.633	0.608	5.5
	60	966	1.258	-1.429	0.459	0.289	0.326	2.051	0.619	0.619	7

Table A.11 : Segmentation metrics for Almería study site, summer season and WorldView-3.

	SP	Object	ED2	AFI	D index	ED3	F measure	Fitness	M	QR	Median
Percent	20	10429	5.720	0.558	0.625	0.434	0.446	19.049	0.620	0.868	10
	30	4598	1.481	0.235	0.488	0.321	0.523	9.956	0.811	0.667	9
	40	2713	0.522	0.035	0.379	0.214	0.497	6.264	0.861	0.505	3.5
	50	1991	0.308	-0.113	0.320	0.169	0.469	4.304	0.866	0.424	1.5
	60	1572	0.368	-0.348	0.297	0.150	0.446	3.359	0.842	0.393	2
	70	1318	0.462	-0.562	0.295	0.153	0.432	2.711	0.818	0.392	4
	80	1149	0.548	-0.669	0.311	0.166	0.418	2.373	0.800	0.412	6.5
	90	1024	0.648	-0.823	0.306	0.178	0.408	1.994	0.779	0.415	5
	100	911	0.864	-1.203	0.320	0.198	0.395	1.796	0.745	0.441	6
	110	817	1.106	-1.504	0.347	0.219	0.379	1.695	0.712	0.479	8
16Bits	190	6957	3.670	0.447	0.609	0.408	0.477	15.904	0.683	0.827	10
	245	4515	1.931	0.299	0.549	0.354	0.493	10.027	0.755	0.737	9
	300	3174	1.075	0.155	0.485	0.298	0.489	7.122	0.802	0.646	8
	355	2379	0.664	-0.046	0.445	0.255	0.468	5.196	0.812	0.585	6
	410	1890	0.426	-0.168	0.393	0.212	0.457	3.587	0.820	0.514	6
	465	1564	0.360	-0.357	0.356	0.182	0.441	2.895	0.823	0.463	5
	520	1340	0.387	-0.450	0.342	0.170	0.427	2.335	0.818	0.443	2.5
	575	1162	0.545	-0.671	0.325	0.177	0.415	2.067	0.795	0.430	4
	630	1042	0.641	-0.824	0.3175	0.175	0.406	1.646	0.786	0.424	3.5
	685	952	0.734	-0.921	0.3179	0.179	0.398	1.521	0.776	0.426	3.5

Table A.12 : Segmentation metrics for Almería study site, summer season and Sentinel-2.

	SP	Object	ED2	AFI	D index	ED3	F measure	Fitness	M	QR	Median
Percent	2	16880	11.310	0.747	0.677	0.475	0.316	31.423	0.478	0.931	10
	3	7348	4.256	0.537	0.626	0.434	0.398	14.049	0.603	0.853	9
	4	4256	2.035	0.321	0.560	0.381	0.417	8.013	0.672	0.761	8
	5	2867	1.019	0.142	0.485	0.321	0.411	5.220	0.722	0.663	3
	6	2113	0.689	-0.080	0.440	0.284	0.394	3.841	0.726	0.603	3
	7	1665	0.508	-0.286	0.400	0.254	0.380	2.986	0.725	0.551	3.5
	8	1372	0.551	-0.445	0.392	0.247	0.367	2.461	0.712	0.540	2.5
	9	1139	0.641	-0.661	0.385	0.246	0.357	2.086	0.696	0.534	4.5
	10	973	0.832	-0.954	0.381	0.247	0.348	1.801	0.672	0.535	6.5
	11	874	1.019	-1.204	0.384	0.253	0.340	1.648	0.658	0.542	5.5
16Bits	15	18136	11.630	0.634	0.680	0.477	0.391	45.722	0.552	0.933	10
	20	10537	6.216	0.531	0.650	0.455	0.409	29.876	0.605	0.890	9
	25	6611	3.520	0.408	0.612	0.423	0.411	17.840	0.645	0.833	8
	30	4633	2.197	0.280	0.579	0.393	0.413	12.531	0.680	0.782	6.5
	35	3469	1.400	0.162	0.543	0.361	0.403	8.985	0.693	0.729	6
	40	2742	1.056	-0.004	0.512	0.335	0.393	6.813	0.696	0.687	5
	45	2274	0.818	-0.129	0.494	0.317	0.380	5.791	0.693	0.660	3.5
	50	1933	0.714	-0.261	0.476	0.304	0.369	4.729	0.686	0.637	3
	55	1632	0.698	-0.491	0.467	0.294	0.361	3.829	0.674	0.624	2
	60	1412	0.716	-0.654	0.455	0.289	0.352	3.424	0.665	0.613	3

Table A.13 : Segmentation metrics for Antalya study site, winter season, and SPOT-7.

	SP	Object	ED2	AFI	D index	ED3	F measure	Fitness	M	QR	Median
Percent	15	9409	1.097	0.163	0.433	0.287	0.516	8.624	0.829	0.598	5.5
	20	5758	0.425	-0.021	0.328	0.193	0.490	5.064	0.866	0.444	3.5
	25	3861	0.252	-0.316	0.274	0.148	0.446	3.592	0.852	0.369	1
	30	2813	0.338	-0.523	0.272	0.146	0.404	2.862	0.831	0.366	2
	35	2165	0.561	-0.875	0.297	0.175	0.364	2.186	0.783	0.404	3
	40	1705	0.848	-1.297	0.333	0.204	0.329	1.889	0.736	0.453	5.5
	45	1341	1.307	-2.149	0.360	0.237	0.292	1.552	0.680	0.500	6.5
	50	1108	1.689	-2.936	0.389	0.262	0.270	1.417	0.640	0.543	8
	55	943	2.415	-4.295	0.422	0.293	0.248	1.336	0.589	0.596	9
	60	811	2.802	-4.827	0.448	0.312	0.233	1.248	0.559	0.633	10
16Bits	150	5005	1.103	0.018	0.508	0.304	0.463	6.846	0.819	0.665	10
	170	4002	0.737	-0.126	0.461	0.268	0.437	5.187	0.821	0.603	9
	190	3319	0.576	-0.288	0.433	0.244	0.422	4.540	0.819	0.563	8
	210	2829	0.512	-0.494	0.414	0.229	0.404	4.129	0.814	0.537	7
	230	2411	0.505	-0.689	0.388	0.203	0.388	3.067	0.800	0.498	3.5
	250	2103	0.586	-0.819	0.376	0.194	0.367	2.334	0.782	0.483	4.5
	270	1849	0.798	-1.097	0.364	0.197	0.343	1.864	0.759	0.474	2.5
	290	1652	0.936	-1.286	0.372	0.206	0.323	1.711	0.739	0.487	3.5
	310	1498	1.005	-1.364	0.372	0.209	0.312	1.503	0.732	0.488	5
	330	1340	1.161	-1.625	0.369	0.209	0.302	1.335	0.721	0.487	5.5

Table A.14 : Segmentation metrics for Antalya study site, winter season, and Sentinel-2.

	SP	Object	ED2	AFI	D index	ED3	F measure	Fitness	M	QR	Median
Percent	2	11651	2.981	0.469	0.603	0.414	0.436	10.525	0.650	0.821	9
	3	5279	0.817	0.029	0.489	0.314	0.427	4.717	0.711	0.663	5
	4	3211	0.496	-0.459	0.413	0.265	0.389	2.923	0.707	0.570	2
	5	2172	0.644	-0.947	0.384	0.243	0.349	2.177	0.686	0.534	2.5
	6	1599	0.979	-1.569	0.388	0.258	0.311	1.673	0.647	0.547	3
	7	1229	1.504	-2.387	0.411	0.288	0.281	1.405	0.596	0.587	4.5
	8	982	2.000	-3.133	0.440	0.308	0.259	1.252	0.561	0.628	5.5
	9	798	2.744	-4.204	0.482	0.340	0.235	1.172	0.510	0.686	7
	10	676	3.322	-5.032	0.510	0.360	0.218	1.136	0.477	0.723	8.5
	11	580	4.447	-6.454	0.539	0.381	0.195	1.096	0.438	0.763	9.5
16Bits	15	10816	3.061	0.438	0.609	0.418	0.449	12.922	0.650	0.826	10
	20	6287	1.454	0.263	0.554	0.367	0.436	7.210	0.690	0.742	9
	25	4131	0.716	0.035	0.496	0.313	0.410	4.630	0.708	0.660	3
	30	3005	0.471	-0.274	0.467	0.278	0.378	3.213	0.699	0.617	2
	35	2323	0.520	-0.659	0.460	0.269	0.345	2.502	0.680	0.606	2
	40	1859	0.689	-1.110	0.457	0.265	0.325	2.015	0.671	0.602	3.5
	45	1498	1.077	-1.731	0.459	0.274	0.301	1.741	0.634	0.609	5
	50	1278	1.499	-2.393	0.469	0.286	0.285	1.470	0.606	0.625	6
	55	1108	1.981	-3.052	0.478	0.302	0.260	1.315	0.576	0.643	7
	60	940	2.486	-4.128	0.477	0.306	0.243	1.193	0.560	0.648	8

Table A.15 : Segmentation metrics for Antalya study site, summer season, and SPOT-7.

	SP	Object	ED2	AFI	D index	ED3	F measure	Fitness	M	QR	Median
Percent	15	9425	1.616	0.230	0.498	0.335	0.517	10.349	0.806	0.689	8
	20	5657	0.481	0.070	0.349	0.211	0.490	5.740	0.856	0.482	4.5
	25	4017	0.215	-0.076	0.272	0.142	0.462	4.038	0.869	0.371	1
	30	2986	0.264	-0.302	0.261	0.133	0.420	2.968	0.847	0.357	2
	35	2351	0.404	-0.612	0.298	0.150	0.388	2.369	0.812	0.398	3
	40	1878	0.503	-0.847	0.306	0.165	0.350	2.001	0.789	0.412	4.5
	45	1610	0.680	-1.200	0.316	0.187	0.334	1.752	0.755	0.433	6
	50	1351	1.043	-1.929	0.350	0.211	0.303	1.548	0.712	0.479	7.5
	55	1136	1.432	-2.656	0.386	0.240	0.275	1.445	0.668	0.529	8.5
	60	974	1.633	-2.977	0.413	0.257	0.257	1.309	0.642	0.562	10
16Bits	140	5644	1.617	0.193	0.545	0.343	0.457	9.088	0.794	0.725	10
	170	4148	0.938	0.065	0.483	0.289	0.435	6.220	0.826	0.639	9
	200	3226	0.634	-0.051	0.434	0.253	0.401	4.326	0.831	0.575	6.5
	230	2606	0.403	-0.183	0.388	0.213	0.373	3.274	0.831	0.512	4.5
	260	2178	0.346	-0.285	0.355	0.192	0.348	2.476	0.826	0.470	2.5
	290	1882	0.396	-0.493	0.360	0.189	0.331	2.311	0.813	0.473	2.5
	320	1595	0.463	-0.680	0.332	0.160	0.315	1.729	0.813	0.431	3
	350	1420	0.512	-0.739	0.330	0.158	0.299	1.470	0.807	0.427	4
	380	1229	0.664	-1.014	0.301	0.155	0.282	1.040	0.798	0.398	6.5
	410	1108	1.221	-2.305	0.309	0.172	0.269	0.980	0.765	0.415	8

Table A.16 : Segmentation metrics for Antalya study site, summer season and Sentinel-2.

	SP	Object	ED2	AFI	D index	ED3	F measure	Fitness	M	QR	Median
Percent	3	6918	1.970	0.216	0.576	0.388	0.445	9.104	0.693	0.780	9
	4	4116	0.882	-0.137	0.505	0.331	0.420	5.017	0.715	0.685	6
	5	2817	0.533	-0.618	0.458	0.286	0.393	3.502	0.713	0.621	2
	6	2100	0.586	-0.889	0.430	0.273	0.355	2.639	0.699	0.587	2
	7	1639	0.782	-1.253	0.431	0.272	0.324	2.068	0.667	0.588	3.5
	8	1323	1.184	-1.964	0.445	0.290	0.295	1.704	0.618	0.612	5
	9	1126	1.481	-2.517	0.454	0.302	0.276	1.572	0.592	0.628	6
	10	930	1.815	-3.085	0.467	0.315	0.258	1.394	0.561	0.650	5.5
	11	809	2.195	-3.586	0.483	0.330	0.238	1.244	0.534	0.674	8.5
	12	689	2.655	-4.332	0.496	0.341	0.218	1.148	0.513	0.694	9
16Bits	25	6044	2.216	0.248	0.589	0.399	0.407	10.773	0.658	0.794	10
	30	4435	1.530	0.136	0.554	0.367	0.388	6.924	0.667	0.743	9
	35	3359	0.973	-0.053	0.522	0.340	0.364	5.256	0.670	0.699	8
	40	2657	0.801	-0.359	0.513	0.327	0.343	4.234	0.664	0.683	5
	45	2180	0.682	-0.634	0.501	0.319	0.330	3.438	0.647	0.669	2.5
	50	1824	0.795	-1.156	0.496	0.313	0.312	2.836	0.632	0.662	2.5
	55	1568	0.956	-1.565	0.493	0.310	0.287	2.533	0.620	0.657	4
	60	1378	1.211	-1.937	0.490	0.309	0.270	2.129	0.602	0.656	5
	65	1217	1.452	-2.304	0.487	0.309	0.257	1.777	0.587	0.655	6
	70	1071	1.570	-2.517	0.475	0.304	0.245	1.599	0.587	0.644	6.5

CURRICULUM VITAE

Name Surname **: Gizem ŞENEL**

EDUCATION **:**

- **B.Sc.** **:** 2017, Istanbul Technical University, Civil Engineering Faculty, Department of Geomatics Engineering
- **M.Sc.** **:** 2019, Istanbul Technical University, Institute of Science, and Technology, Department of Geomatics Engineering

SCHOLARSHIPS:

- 2019: Doctorate Scholarship Holder of The Scientific and Technological Research Council of Turkey (In Turkish, Türkiye Bilimsel Ve Teknolojik Araştırma Kurumu, TÜBİTAK), 2211-A National PhD Scholarship Program
- 2019: Doctorate Scholarship Holder of the Council of Higher Education, Turkey (CoHE, in Turkish Yükseköğretim Kurulu, YÖK) in the priority field of Remote Sensing and GIS within the scope of 100/2000 Program
- 2021: 2214-A Doctoral Research Grant awarded by The Scientific and Technological Research Council of Turkey (TÜBİTAK)

PUBLICATIONS ON THE THESIS:

- **Senel, G.,** Aguilar, M. A., Aguilar, F. J., Nemmaoui, A., and Goksel, C. 2023. Unraveling Segmentation Quality of Remotely Sensed Images on Plastic-Covered Greenhouses: A Rigorous Experimental Analysis from Supervised Evaluation Metrics, *Remote Sensing*, 15(2). doi:10.3390/rs15020494

OTHER PUBLICATIONS:

Research Articles (SCI)

- Isiacik Colak, T**., Senel, G.,** Goksel, C. (2021). GIS-Based Maritime Spatial Planning for Site Selection of Offshore Wind Farms with Exergy Efficiency Analysis: A Case Study, *International Journal of Exergy*, 34(2), pp. 255-268 doi:10.1504/IJEX.2021.10035340.
- Sözen, S., Yüzer, E., Duba, S., Gökçekuş, H., Dogru A. O., **Senel, G.** Goksel, C. Orhon, D. (2021). Water management for Istanbul: collapse or survival, *Environmental Earth Sciences*, 80, 280-289 doi:10.1007/s12665-021-09563-0.

- **Senel, G.,** Dogru, A.O., Goksel, C. (2020). Exploring the Potential of Landsat-8 OLI and Sentinel-2 MSI Data for Mapping and Monitoring Enez Dalyan Lagoon, *Desalination and Water Treatment*, 177, pp. 330– 337; doi: 10.5004/dwt.2020.24802.
- Goksel, C., **Senel, G.,** Dogru, A.O. (2020). Determination of Shoreline Change in the Black Sea Cost of Istanbul Using Remote Sensing and GIS Technology, *Desalination and Water Treatment*, 177, pp. 242–247; doi: 10.5004/dwt.2020.24975.
- Bektas Balcik, F., **Senel, G.,** Goksel, C. (2020). Object-Based Classification of Greenhouses Using Sentinel-2 MSI and SPOT-7 Images: A Case Study from Anamur (Mersin), Turkey, *IEEE Journal of Selected Topics in Applied Earth Observations and Remote Sensing*, 13, pp. 2769-2777; doi: 10.1109/JSTARS.2020.2996315.
- Arekhi, M., Goksel, C., Balik Sanli, F., and **Senel, G.** (2019). Comparative Evaluation of the Spectral and Spatial Consistency of Sentinel-2 and Landsat-8 OLI Data for Igneada Longos Forest. *ISPRS-International Journal of Geo-Information*, 8 (2), 56; doi: 10.3390/ijgi80200564**.**

Conference Proceedings

- **Senel, G.,** Goksel, C. (2021). Investigation of the Thresholding Methods and Water Indices for Water Surface Mapping Using Landsat-8 OLI Data, *International Symposium on Applied Geoinformatics (ISAG2021),* December 2-3 2021, Riga, Latvia, doi:10.15659/isag2021.12508.
- İşiaçık Çolak, T., Soltani, H. R., **Senel, G.,** Göksel, Ç. (2021). GIS-Based Offshore Wind Farm Site Selection Using Fuzzy Multi-Criteria Decision-Making Methods With Exergy Efficiency Analysis, *9th Global Conference on Global Warming (GCGW-2021),* pp. 127-130, August 1-4, 2021, Crotia, ISBN:978-605-648061-4.
- **Senel, G.,** Eroglu, M., Bektas Balcik, F., Goksel, C. (2020). Analysing Flood Affected Region in Meriç River Basin Using Sentinel-1 and Sentinel-2 Data, *8th International Conference on Cartography and GIS,* Volume: 1, pp. 710-716, Nessebar, Bulgaria, ISSN: 1314-0604.
- **Senel, G.,** Eroglu, M., Bektas Balcik, F., Goksel, C. (2020). Flood Extent Determination in Agricultural Fields Using Sentinel-2 Data and Random Forest Classification, *8th International Conference on Cartography and GIS,* Volume: 1, pp. 702-709, Nessebar, Bulgaria, ISSN: 1314-0604.
- Bektas Balcik, F., **Senel, G.,** Goksel, C. (2019). Greenhouse Mapping using Object Based Classification and Sentinel-2 Satellite Imagery, *IEEE, 2019 8th International Conference on Agro-Geoinformatics (Agro-Geoinformatics),* July 16-19, Istanbul, Turkey, doi: 10.1109/Agro-Geoinformatics.2019.8820252.
- **Senel, G.,** Bektas Balcik, F., Goksel, C. (2019). Qualitative and Quantitative Performance Evaluation of the Different Pansharpening Algorithms Applied to Landsat-8 Imagery, *International Symposium on Applied Geoinformatics ISAG-2019*, Volume: 1, No: 1, 7-9 November 2019, Istanbul, Turkey, ISBN: 978-975-461-564-7/2019.

- Göksel, Ç., Arekhi, M., Balık Şanlı, F., **Şenel, G.** (2019). Landsat-8 ve Sentinel-2 Uydu Görüntülerinin Spektral Tutarlılığının Karşılaştırmalı Değerlendirmesi; İğneada Longoz Ormanları Örneği (Comparative Evaluation of the Spectral Consistency of Sentinel-2 and Landsat-8 OLI Data for Igneada Longos Forest). *17. Türkiye Harita Bilimsel ve Teknik Kurultayı (17th Turkish Scientific and Technical Mapping Symposium)* 25-27 April, Ankara, Turkey.
- Isiacik Colak. T., **Senel , G.,** Goksel , C. (2018). Coastline Zone Extraction Using Landsat-8 OLI Imagery, Case Study: Bodrum Peninsula, Turkey. The International Archives of the Photogrammetry, Remote Sensing and Spatial Information Sciences, Volume XLII-4/W12,pp: 101-104, 2019. *5th International Conference on Geoinformation Science – GeoAdvances 2018*, October 10–11, Casablanca, Morocco. doi: 10.5194/isprs-archives-XLII-4-W12-101-2019.